National Technical University of Ukraine
"Igor Sikorsky Kyiv Polytechnic Institute"
Ministry of Education and Science of Ukraine

National Technical University of Ukraine
"Igor Sikorsky Kyiv Polytechnic Institute"
Ministry of Education and Science of Ukraine

Qualifying scientific
work as a manuscript

ZHOU ZHENTAO

UDC 546.05+546.8+ 66.067

THESIS

Research on Modified MOF Materials for Water Pesticide Pollutant Purification

161 Chemical Technologies and Engineering
16 Chemical and Bioengineering

Submitted for the attainment of the Doctor of Philosophy degree

The dissertation contains the results of personal research. The use of ideas, results, and texts from other authors are accompanied by references to the respective sources.

Чжоу Чжентао Zhou Zhentao

Scientific Supervisor: Tetiana Dontsova, Dr. Tech. Sc., Professor.

Kyiv – 2025

ABSTRACT

Zhou Zhentao. Research on modified MOF materials for water pesticide pollutant purification. – Qualified scientific work on the rights of the manuscript.

Dissertation for the degree of Doctor of Philosophy in the specialty 161 – Chemical Technologies and Engineering – National Technical University of Ukraine "Igor Sikorsky Kyiv Polytechnic Institute", Kyiv, 2025.

This dissertation is divided into two main parts: the first is the study of a Ti-MOF-based NH_2-MIL-125/TiO_2 composite photocatalytic system; the second is the study of an M88A@TA-X photo-Fenton catalytic system based on Fe-MOF modified with tannic acid and calcined. In the first part, the physicochemical structure of the NH_2-MIL-125/TiO_2 composites and their photocatalytic degradation performance of the insecticide imidacloprid in water are studied in detail. In the second part, the physicochemical structure of the M88A@TA-X series of materials, their photo-Fenton degradation performance of the herbicide atrazine, and their potential applications are studied in detail.

This work investigates the photocatalytic activity of NH_2-MIL-125/TiO_2 composites synthesized at different dosage ratios of TiO_2 and TPOT (the precursor of NH_2-MIL-125). The results show that all NH_2-MIL-125/TiO_2 composites exhibit superior catalytic performance compared to pure NH_2-MIL-125. Furthermore, we found that the material synthesized with a TiO_2/TPOT ratio of 1:1 (NH_2-MIL-125/TiO_2-100%) exhibited optimal catalytic activity (removing 100% of imidacloprid in 90 minutes). Increasing the TiO_2/TPOT ratio from 0.35:1 to 1:1 showed an

improvement in catalytic activity. However, further increasing the TiO_2/TPOT ratio (from 1:1 to 2:1) did not lead to a further increase in catalytic activity. Therefore, this study used NH_2-MIL-125/TiO_2-100% as a representative material for characterization.

X-ray diffraction spectroscopy (XRD), Infrared absorption spectrum (FTIR), and Thermogravimetric analysis (TGA) characterization demonstrated that TiO_2 successfully incorporated into the NH_2-MIL-125/TiO_2 composite during its preparation, and that its incorporation did not disrupt the basic lattice and chemical structure of NH_2-MIL-125. Scanning electron microscopy (SEM) results demonstrated that the TiO_2 in the NH_2-MIL-125/TiO_2 composite was uniformly dispersed on the surface, facilitating contact between the catalyst and the pollutant during the reaction. Furthermore, Ultraviolet-Visible Diffuse Reflectance Spectroscopy (UV-Vis DRS) results indicate that the band gap energy of NH_2-MIL-125/TiO_2 is 2.58 eV, lower than that of NH_2-MIL-125 (2.68 eV) and TiO_2 (3.36 eV). This suggests that NH_2-MIL-125/TiO_2 has a wider spectral response range, thus favoring photocatalytic reactions.

For a photo-Fenton catalyst (M88A@TA-X) prepared by modifying Fe-MOF (MIL-88A, denoted as M88A), this paper discusses the effects of different modification methods (including calcination temperature and whether tannic acid modification was used before calcination) on the photo-Fenton catalytic performance of the catalyst. Results showed that M88A@TA-2, modified with tannic acid and calcined at 200 °C, exhibited the best photo-Fenton activity, achieving 100% atrazine degradation within 30 minutes. Its reaction rate constant was 0.164 min^{-1}, 32.8 and 5.5 times that of M88A (0.005 min^{-1}) and M88A@TA (0.030 min^{-1}), respectively. M88A@TA-3 and M88A@TA-4, synthesized at higher temperatures, exhibited significantly reduced or completely inactivated activities. Furthermore, the catalytic activity of M88A-2

(synthesized by calcining MIL-88A at 200 °C without TA modification) showed almost no increase compared with that of pure MIL-88A. These findings confirm that tannic acid modification and calcination at 200°C are crucial for enhancing the catalytic activity of MIL-88A. In addition to evaluating the photo-Fenton degradation rates of various materials, we also assessed their H_2O_2 consumption rates during the photo-Fenton reaction. Results show that M88A@TA-2 exhibits approximately fourfold higher H_2O_2 utilization efficiency than M88A, which holds great promise for its future practical applications.

To investigate the mechanism underlying the excellent photo-Fenton activity of M88A@TA-2, the morphology and phase structure of the prepared material were characterized using SEM, Transmission electron microscopy (TEM), and Brunauer-Emmett-Teller surface area analysis (BET) methods. Results indicate that M88A@TA-2 exhibits a loose and porous structure compared to unmodified M88A. Furthermore, its surface area, at 44 m^2/g, is significantly higher than that of M88A (13 m^2/g). Furthermore, XRD, XPS, TGA, and FTIR characterizations demonstrate that M88A@TA-2 possesses a rich defect structure. The band structure of the prepared material was investigated using UV-Vis DRS and X-ray photoelectron spectroscopy (XPS) valence band spectroscopy. Results show that, thanks to defects regulating the band structure, the band gap energy of M88A@TA-2 (2.70 eV) is higher than that of M88A (2.94 eV), resulting in superior light absorption.

This paper also discusses the mechanism by which M88A@TA-2 degrades atrazine in water via a photo-Fenton catalytic reaction. First, reactive oxygen species (ROS) scavenging experiments and electron paramagnetic resonance spectroscopy characterization confirmed that the primary reactive oxygen species in the photo-

Fenton catalytic reaction are ·OH and $^1O_2$. Ultra-high performance liquid chromatography-quadrupole time-of-flight mass spectrometry (UPLC-QTOF-MS) was used to analyze samples from the photo-Fenton degradation of atrazine using M88A@TA-2, revealing the degradation products. Furthermore, the photo-Fenton degradation products of atrazine by M88A@TA-2 after the addition of different ROS scavengers were analyzed to infer the effects of different ROS on the degradation products. The results further confirm that ·OH and $^1O_2$ are the dominant ROS in the M88A@TA-2 photo-Fenton system.

The scientific novelty of the dissertation lies in the following provisions. A new composite photocatalyst, NH_2-MIL-125/TiO_2, based on metal-organic framework (MOF) semiconductors, has been synthesised. This combines the high light absorption capacity of NH_2-MIL-125 with the high oxidation capacity of TiO_2, allowing for greater photocatalytic activity. A new, simple synthesis method has been proposed which includes stages of modification with tannic acid and calcination. This method allows the synthesis of M88A@TA-2 material containing a large number of defects, demonstrating high photo-Fenton catalytic activity and extremely high H_2O_2 utilisation efficiency at low concentrations. This significantly reduces the energy consumption of the photo-Fenton process. Furthermore, a mechanism for the photo-Fenton decomposition of atrazine using the M88A@TA-2 catalyst has been proposed, providing valuable information for future research in the field of photo-Fenton catalysis.

The practical significance of this work lies in establishing the optimal conditions for the synthesis of the NH_2-MIL-125/TiO_2 composite, which provides the basis for its future large-scale production. In addition, a simple method for the synthesis of the

highly efficient photo-Fenton catalyst M88A@TA-2 was developed as part of this study. It has been shown that the use of M88A@TA-2 increases the activity of the traditional photo-Fenton catalyst M88A by 32.8 times and increases the efficiency of the photocatalytic process when activated by hydrogen peroxide by 4 times, which indicates that M88A@ TA-2 effectively decomposes pollutants at extremely low H_2O_2 concentrations (1.76 mM). In addition, M88A@TA-2 demonstrated strong pH adaptability, which will reduce energy consumption, capital costs and reagent costs when treating complex real-world water environments, demonstrating its significant potential for applications in photo-Fenton processes.

Keywords: *pesticide pollution, metal-organic frameworks, modification, titanium(IV) dioxide, photocatalysis, photo-Fenton, visible light, reactive oxygen species, hydrogen peroxide*

The list of applicants publication as follows:

Scientific papers:

1. **Zhou Zhentao**, Tetiana Dontsova. Modification methods to enhance the performance of TiO_2 in photocatalysis. *Water and Water Purification Technologies. Scientific and Technical News*, 2023, 36(2): 40-57. https://doi.org/10.20535/2218-930022023299542. *Contributions of the author: literature analysis, experiments performing, paper drafting, submission.*

2. **Zhou Zhentao**, Anastasiia Sukhoivanenko, Tetiana Dontsova. Prospects of using MOF/TiO_2 nanocomposites for photocatalytic degradation of pesticides. *Functional Materials*, 2024, 31 (4): 630-637. https://doi.org/10.15407/fm31.04.630.

Contributions of the author: literature analysis, experiments performing, paper drafting.

3. Wang, W., Shi, H., Shi, H., Zhou, Z., Mao, L., Zhang, L., & Liu, X. Application of modified biochar in integrated pollution management for pesticides and antibiotics in water: Recent advances and future prospects. Environmental Research, 2025, 285: 122499. https://doi.org/10.1016/j.envres.2025.122499. *Contributions of the author: analysis of literature, experiments performing, data processing, paper drafting.*

Abstracts of conference presentations:

1. Zhou Zhentao, Dontsova T.A. (2023). Degradation performance and mechanism of MOF/TiO_2 nanocomposites for pesticide pollutants in aqueous phase. *Book of abstracts of Міжнародну конференцію з хімії, хімічної технології та екології, що присвячена 125-річчю КПІ ім. Ігоря Сікорського.* Kyiv, p. 263. *The applicant's personal contribution is conducting experimental research, processing the results obtained, writing and submitting abstract.*

2. Zhou Zhentao, Dontsova T.A. (2023). Prospects for the use of TiO_2/MOF structures in photocatalysis. *Book of abstracts of the International research and practice conference «Nanotechnology and nanomaterials» (NANO-2023).* Lviv, p. 206. *The applicant's personal contribution is conducting experimental research, processing the results obtained, writing and submitting abstract.*

АНОТАЦІЯ

Чжоу Чженьтао. Дослідження модифікованих MOF-матеріалів для очищення води від забруднення пестицидами. – Кваліфікаційна наукова праця на правах рукопису.

Дисертація на здобуття наукового ступеня доктора філософії за спеціальністю 161 – Хімічні технології та інженерія – Національний технічний університет України «Київський політехнічний інститут імені Ігоря Сікорського», Київ, 2025.

Дана дисертація складається з двох напрямів досліджень: перший присвячений дослідженню фотокаталітичної системи на основі композиту NH_2-MIL-125/TiO_2 з Ti-MOF; другий – дослідженню фотокаталітичної системи M88A@TA-X на основі Fe-MOF, яку або модифікували дубильною кислотою, або прожарювали. В роботі детально досліджується фізико-хімічна структура композитів NH_2-MIL-125/TiO_2 та їх фотокаталітична активність у розкладанні інсектициду імідаклоприду у воді. Також детально досліджується фізико-хімічна структура матеріалів серії M88A@TA-X, їх фото-Фентон здатність по відношенню до розкладання гербіциду атразину та їх потенційні застосування.

Досліджено фотокаталітична активність композитів NH_2-MIL-125/TiO_2, синтезованих при різних співвідношеннях дозувань TiO_2 і ТРОТ (попередника NH_2-MIL-125). Результати показують, що всі композити NH_2-MIL-125/TiO_2 демонструють кращі каталітичні властивості порівняно з чистим NH_2-MIL-125. Крім того виявлено, що матеріал, синтезований із співвідношенням TiO_2/ТРОТ

як 1:1 (NH_2-MIL-125/TiO_2-100%), продемонстрував найбільшу каталітичну активність (видалення 100% імідаклоприду за 90 хвилин). При збільшенні співвідношення TiO_2/ТРОТ з 0.35:1 до 1:1 каталітична активність зростає. Однак подальше збільшення співвідношення TiO_2/ТРОТ (зі 1:1 до 2:1) не призводить до подальшого збільшення каталітичної активності. Тому як репрезентативний матеріал для характеризації було обрано NH_2-MIL-125/TiO_2-100%.

Результати характеризації методами рентгенівського фазового аналізу (РФА), інфрачервоної спектроскопії (ІЧ) та термогравіметричного аналізу (ТГА) показали, що TiO_2 успішно вбудовується в композит NH_2-MIL-125/TiO_2 під час його синтезу і не порушують будову та хімічну структуру NH_2-MIL-125. Результати скануючої електронної мікроскопії (СЕМ) продемонстрували, що TiO_2 рівномірно розподіляється на поверхні композиту NH_2-MIL-125/TiO_2, що полегшує контакт між каталізатором і забруднювачем під час фотокаталітичного процесу. Крім того, результати ультрафіолет-видимої дифузної відбивної спектроскопії (UV-Vis DRS)показують, що ширина забороненої зони композиту NH_2-MIL-125/TiO_2 становить 2,58 еВ, що нижче, ніж у зразків NH_2-MIL-125 (2,68 еВ) і TiO_2 (3,36 еВ). Це свідчить про те, що NH_2-MIL-125/TiO_2 має ширший спектральний діапазон чутливості, що сприятиме більш ефективного фотокаталітичного розкладання забрудників у водних розчинах.

У дисертації розглядається вплив різних методів модифікування Fe-MOF (MIL-88A, позначений як M88A) включаючи стадії прожарювання та модифікування дубильною кислотою перед прожарюванням на фото-Фентонівські каталітичні властивості каталізатора M88A@TA-X. Результати показали, що M88A@TA-2, модифікований дубильною кислотою і прожарений

при 200 °C, продемонстрував найкращу фото-Фентон активність, досягнувши 100% розкладання атразину протягом 30 хвилин. Константа швидкості реакції становила 0,164 хв$^{-1}$, що в 32,8 і 5,5 разів перевищувало показники для M88A (0,005 хв$^{-1}$) і M88A@TA (0,030 хв$^{-1}$) відповідно. M88A@TA-3 і M88A@TA-4, що синтезовані при вищих температурах, продемонстрували значно знижену або повністю інактивовану активність. Крім того, каталітична активність M88A-2 (синтезованого шляхом прожарювання M88A при 200 °C без модифікації TA) майже не збільшилася порівняно з чистим M88A.. Ці результати підтверджують, що одночасне модифікування дубильною кислотою та прожарювання при температурі 200 °C є вирішальними для підвищення каталітичної активності Fe-MOF (M88A). Окрім оцінки швидкості фото-Фентонового розкладання різних матеріалів також оцінено швидкість розкладання H_2O_2 під час фото-Фентонової реакції. Результати показали, що при розкладанні такої ж кількості атразину M88A@TA-2 потребував на чверть менше H_2O_2, ніж M88A, що вказує на те, що ефективність використання H_2O_2 M88A@TA-2 була в чотири рази вищою, чим M88A.

Для дослідження механізму, що лежить в основі фото-Фентонської активності M88A@TA-2, морфологія та фазова структура синтезованого матеріалу були охарактеризовані за СЕМ, трансмісійної електронної мікроскопії (ТЕМ) та аналізу питомої поверхні Брунауер-Еммет-Теллер (БЕТ). Результати показують, що M88A@TA-2 має більш пористу структуру порівняно з немодифікованим M88A. Крім того, його площа поверхні, що становить 44 м^2/г, значно перевищує площу поверхні M88A (13 м^2/г). Більше того, результати характеризації методами РФА, рентгенівської фотоелектронної спектроскопії

(РФЕС), ТГА та ІЧ демонструють, що M88A@TA-2 має високо дефектну структуру. Структура зон M88A@TA-2 досліджена за допомогою UV-Vis DRS та РФЕС методів. Результати показують, що завдяки дефектам, які впливають на структуру зон, енергія забороненої зони M88A@TA-2 (2,70 еВ) є вищою, ніж у M88A (2,94 еВ), що забезпечує краще поглинання світла.

У дисертації також представлений механізм, який запропоновано для розкладання атразину у воді за допомогою M88A@TA-2 у каталітичній реакції фото-Фентона. Методами вилученням активних форм кисню (ROS) та електронного парамагнітного резонансу показано, що основними активними формами кисню у фотокаталітичній реакції Фентона є ·OH та $^1O_2$. Розчин зразка після фото-Фентоновської деградації атразину за допомогою M88A@TA-2 був проаналізований за допомогою ультрапродуктивної рідинної хроматографії-квадрупольної часопролітної мас-спектрометрії (UPLC-QTOF-MS), що виявило продукти деградації атразину. Крім того, були проаналізовані продукти фото-Фентоновської деградації атразину за допомогою M88A@TA-2 після додавання різних поглиначів активних форм кисню (ROS), щоб визначити вплив різних ROS на продукти деградації. Отримані результати ще раз підтверджують, що ·OH та $^1O_2$ є домінуючими ROS у фото-Фентонівській системі M88A@TA-2.

Науковою новизною дисертації є синтез нового композитного фотокаталізатора NH_2-MIL-125/TiO_2 на основі MOF-напівпровідників, який поєднує високу здатність світлопоглинання NH_2-MIL-125 та високу здатність до окиснення TiO_2, що дозволяє досягати більшої фотокаталітичної активності. Запропоновано новий та простий метод синтезу, який має стадії модифікування дубильною кислотою і прожарювання, що дозволило синтезувати матеріал

M88A@TA-2 з великою кількістю дефектів та продемонструвати високу фото-Фентонову каталітичну активність і надзвичайно високу ефективність використання H_2O_2 за малих концентрацій, що суттєво зменшує енергоспоживання фото-Фентонового процесу. Запропоновано механізм фото-Фентонового розкладання атразину за допомогою каталізатору M88A@TA-2, який пояснює та надає цінну інформацію для майбутніх досліджень у галузі фото-Фентонового каталізу.

Практичне значення цієї роботи полягає у встановленні оптимальних умов синтезу композиту NH_2-MIL-125/TiO_2, що забезпечує основу для його майбутнього масштабного виготовлення. Крім того, в рамках цього дослідження було розроблено простий метод синтезу високоефективного фото-Фентон каталізатора M88A@TA-2. Показано, що використання M88A@TA-2 збільшує активність традиційного фото-Фентона каталізатора M88A в 32,8 рази та підвищує ефективність фотокаталітичного процесу при активації пероксидом водню в 4 рази, що свідчить про те, що M88A@TA-2 ефективно розкладає забруднювачі при надзвичайно низьких концентраціях H_2O_2 (1,76 мМ). Крім того, M88A@TA-2 продемонстрував сильну адаптивність до pH, яка дозволить зменшити споживання енергії, знизити капітальні затрати та витрати на реагенти при очищенні складних реальних водних середовищ, що демонструє свій значний потенціал при застосуваннях у фото-Фентон процесах.

Ключові слова: *забруднення пестицидами, металоорганічні каркаси, модифікація, титану (IV) оксид, фотокаталіз, фото-Фентон, видиме світло, активні форми кисню, пероксид водню*

CONTENTS

LIST OF ABBREVIATIONS

ROS – Reactive Oxygen Species

MBR – Membrane Bioreactor

AOPs – Advanced Oxidation Processes

TOC – Total Organic Carbon

EPR – Electron Paramagnetic Resonance

MOFs – Metal-Organic Frameworks

TPOT – Titanium Isopropoxide

TA – Tannic Acid

SEM – Scanning Electron Microscopy

TEM – Transmission Electron Microscopy

EDS – Energy-Dispersive X-Ray Spectroscopy

BET – Brunauer-Emmett-Teller

XRD – X-ray Diffraction

FTIR – Fourier Transform Infrared Spectroscopy

XPS – X-ray Photoelectron Spectroscopy

TG – Thermogravimetric Analysis

ICP-OES – Inductively Coupled Plasma Optical Emission Spectroscopy ()

UV-Vis DRS – UV-Vis Diffuse Reflectance Spectroscopy

ATZ – Atrazine

IMD – Imidacloprid

RhB – Rhodamine B

INTRODUCTION

Relevance of the topic.

As human demands for agricultural production continue to rise, the resulting problem of pesticide pollution is becoming increasingly serious. These organic pesticides are often persistent, migratory, and toxic organic chemicals, posing a significant threat to the ecological environment and human health. However, due to the low concentrations and high stability of organic pesticide contaminants in water, traditional water treatment methods struggle to effectively remove these pollutants. This can lead to their accumulation in the environment and even entry into drinking water systems, threatening drinking water safety. Therefore, the development of new water treatment technologies is essential to address this problem.

Among the many new water treatment technologies, heterogeneous photocatalysis and heterogeneous photo-Fenton catalysis offer unique advantages such as catalyst reusability, solar energy utilization, and environmental friendliness, making them highly promising water treatment technologies. However, traditional photocatalysts and photo-Fenton catalysts are primarily based on semiconductor materials such as TiO_2 and Fe_3O_4. These traditional semiconductor materials often have low visible light utilization efficiency and are difficult to modify. Metal-organic frameworks (MOFs), as a new type of semiconductor-like material, possess flexible structures and generally possess strong light absorption capabilities, making them highly promising photocatalysts and photo-Fenton catalysts. The Ti-based MOF NH_2-MIL-125 exhibits excellent visible light absorption and stability, making it a suitable photocatalyst for water treatment. However, its photocatalytic oxidation ability is relatively poor due to its bandgap structure. Therefore, the oxidation performance of NH_2-MIL-125 can be

enhanced by combining it with the semiconductor photocatalyst TiO_2, which has strong photocatalytic oxidation performance, to create a composite material. This approach has the potential to simultaneously address the issues of TiO_2 poor light absorption and NH_2-MIL-125 weak oxidation ability. Therefore, developing suitable composite synthesis methods is crucial.

The Fe-based MOF MIL-88A, due to its abundant Fe sites and high visible light absorption, is well-suited as a photo-Fenton catalyst. However, MIL-88A suffers from low specific surface area, low Fe site utilization, and poor Fe site activity. Defect engineering can often improve catalyst mass transfer, enhance active site utilization, and improve the reactivity of active sites. Therefore, it is very important to develop targeted modification methods and use defect engineering to modify MIL-88A to further improve its photo-Fenton efficiency for its practical application.

The connection of the work with scientific programs, plans, and topics.

The dissertation was completed at the Department of Inorganic Substances Technology, Water Treatment and General Chemical Technology of the National Technical University of Ukraine 'Igor Sikorsky Kyiv Polytechnic Institute' as part of the project funded by the National Research Fund of Ukraine 'Synthesis of low-cost ceramic membranes of the controlled design for mobile MF/UF/NF systems', registration card 0123U102670.

Research purposes and tasks.

The research objectives of this work are to develop high-performance MOF-based photocatalytic and photo-Fenton catalysts for the efficient degradation of various

organic pesticide pollutants in water.

To achieve these objectives, this study set the following research tasks:

1. Design and synthesize NH_2-MIL-125/TiO_2 composite photocatalysts and investigate the effects of different synthesis conditions (TiO_2/TPOT addition ratio) on the composite photocatalyst's physicochemical properties (morphology, phase structure, chemical structure, energy band structure, optical properties, etc.) and photocatalytic activity.

2. Design and synthesize defect-rich Fe-MOF photo-Fenton catalysts and investigate the effects of different modification conditions on the photo-Fenton performance of the synthesized MOF materials for pesticide degradation. Experimental and characteristic studies of morphology, specific surface area, phase structure, chemical structure, energy band structure, elemental composition, chemical structure and defect concentration of prepared materials in order to elucidate the mechanism of catalytic activity.

3. Through ROS scavenging experiments, EPR spectroscopy, UPLC-QTOF-MS, and other experimental methods, the main active species in the pesticide degradation process of the prepared photo-Fenton material were investigated and the degradation pathway of the pesticide was inferred. This provided a clearer understanding of the photo-Fenton reaction mechanism.

4. The H_2O_2 utilization efficiency and pH resistance of the prepared photo-Fenton material were tested to evaluate its practical application potential.

Research object:

NH_2-MIL-125/TiO_2 composite photocatalyst, modified Fe-MOF photo-Fenton catalyst, the photocatalytic processes in which they participate.

Research subject:

Synthesis conditions, morphology, structural characteristics, optical properties, and photocatalytic activity of NH_2-MIL-125/TiO_2 photocatalyst. Synthesis conditions, morphology, structural characteristics, optical properties, and photo-Fenton catalytic activity of the modified Fe-MOF material M88A@TA-X.

Research Methodology.

The morphology of the prepared materials was characterized using a Regulus 8100 (Hitachi High-Tech, Japan) field emission scanning electron microscope (SEM). Transmission electron microscopy (TEM) and energy dispersive X-ray spectroscopy (EDS) tests were performed using a FEI Tecnai G2 F30 microscope (Thermo Fisher Scientific, USA) equipped with an Oxford XPLORE spectrometer to analyze the internal structure of the prepared materials. The specific surface area and pore size distribution of the samples were determined using nitrogen adsorption-desorption (77 K) using a fully automated surface and porosity analyzer (Builder 4200, Micromeritics Tristar II 3020 M). Micromeritics ASAP 2460 software was used for Brunauer-Emmett-Teller (BET) model fitting. The crystal structure of the sample was characterized using a Bruker D8 Advance X-ray diffractometer (Bruker, Germany), using Cu Kα radiation (λ = 1.5406 Å) as the X-ray source, with an operating voltage and current set to 40 kV and 40 mA, respectively. The chemical structure and functional group composition of the samples were analyzed using a Fourier transform infrared spectrometer (Nicolet 6700, Thermo Fisher Scientific, USA). The elemental composition and chemical state of the samples were characterized using an X-ray photoelectron spectrometer (ESCALAB 250Xi, Thermo Fisher Scientific, USA). The

simultaneous thermal analysis (TG-DTA) test of the sample was carried out using a NETZSCH STA 449 F3/F5 thermal analyzer (NETZSCH, Germany). The Fe content of the samples was determined using a Thermo ICAP PRO inductively coupled plasma optical emission spectrometer (ICP-OES, Thermo Fisher Scientific, USA). Characterization was performed using an ER200-SRC (Bruker, Germany) electron paramagnetic resonance (EPR) spectrometer. The ultraviolet-visible diffuse reflectance spectroscopy (UV-vis DRS) of the samples was tested using a Lambda 650S UV-visible spectrophotometer (Perkin Elmer, USA). A 50W xenon lamp (Beijing Perfect Light PLS-SXE300E) was used as a simulated solar light source for photocatalysis and photo-Fenton catalysis experiments.

Scientific novelty.

The scientific novelty of the dissertation lies in the following provisions:

1. A new composite photocatalyst NH_2-MIL-125/TiO_2 based on MOF semiconductors has been synthesised, combining the high light absorption capacity of NH_2-MIL-125 and the high oxidation capacity of TiO_2, which allows for greater photocatalytic activity.

2. A new and simple synthesis method has been proposed, which includes stages of modification with tannic acid and calcination, allowing the synthesis of the material M88A@ TA-2 material with a large number of defects and demonstrate high photo-Fenton catalytic activity and extremely high H_2O_2 utilisation efficiency at low concentrations, which significantly reduces the energy consumption of the photo-Fenton process.

3. A mechanism for the photo-Fenton decomposition of atrazine using the

M88A@TA-2 catalyst has been proposed, which explains and provides valuable information for future research in the field of photo-Fenton catalysis.

The Practical Significance of the Obtained Results.

The practical significance of this work lies in establishing the optimal conditions for the synthesis of the NH_2-MIL-125/TiO_2 composite, which provides the basis for its future large-scale production. In addition, a simple method for the synthesis of the highly efficient photo-Fenton catalyst M88A@TA-2 was developed as part of this study. It has been shown that the use of M88A@TA-2 increases the activity of the traditional photo-Fenton catalyst M88A by 32.8 times and increases the efficiency of the photocatalytic process when activated by hydrogen peroxide by 4 times, which indicates that M88A@ TA-2 effectively decomposes pollutants at extremely low H_2O_2 concentrations (1.76 mM). In addition, M88A@TA-2 demonstrated strong pH adaptability, which will reduce energy consumption, capital costs and reagent costs when treating complex real-world water environments, demonstrating its significant potential for applications in photo-Fenton processes.

Contributions of the author.

All scientific results, conclusions, and statements presented for defense were obtained by the applicant personally. In the co-authored scientific works, the applicant participated in task formulation, conducting the experimental research, discussing and summarizing results, and writing and formatting the articles. In the co-authored publications, the author's contribution is primary. The research results have been presented by the applicant personally at scientific conferences. The co-authors of the

scientific works are the scientific supervisor and researchers with whom the joint studies were conducted.

Approbation of the results of the dissertation.

The results of the study were presented and discussed at 2 international conferences: “Nanotechnology and nanomaterials” (NANO-2023) and Міжнародна конференція з хімії, хімічної технології та екології, що присвячена 125-річчю КПІ ім. Ігоря Сікорського (2023).

Publications.

The study results were published in 3 scientific publications, that are 3 scientific papers published in profile journals: 1 in category B of profile journals of Ukraine and 2 – indexed in Scopus international citations database.

Structure and scope of work.

The dissertation consists of an introduction, 4 chapters, a conclusion, a list of 104 references. The total number of pages in the paper is 133, with 117 pages for the main part. It includes 47 figures, 6 equations, and 5 tables.

CHAPTER 1. The Current Situation, Hazards and Control Methods of Pesticide Pollution in Water

Water is a very important natural resource, which is particularly important for maintaining the normal operation of the earth's ecosystem and providing a guarantee for the survival and development of the entire ecosystem. Although the earth has abundant water resources, due to the uneven distribution of water resources in time and space, there are still more than 2 billion people whose living water is limited [1]. In addition, due to huge population growth, modern industrialization, civilization, domestic and agricultural activities and other geological, environmental and global changes, the pollution of natural water bodies has become increasingly serious, resulting in an increasing number of people lacking basic drinking water supplies [2]. These persistent pollutants enter water bodies, which are unable to remove them through self-purification processes, contaminating drinking water sources. The release of these pollutants into the environment causes widespread pollution and severe ecological damage. Water pollution also increases health risks for the public. Water pollution causes a range of illnesses and injuries, including approximately 190 million illnesses and 60,000 deaths annually [3]. Related studies have reported links between water pollution and acute waterborne diseases, including hepatitis, giardiasis, cryptosporidiosis, cholera, dysentery, diarrhoea, and typhoid fever [4], [5], [6]. The increasing negative impact of water pollution puts more and more people at risk of cancer-causing diseases and may even contribute to the development of cancer villages[7].

1.1 Current status of pesticide pollution in water

With the rapid development of agriculture and the rapid growth of food production, global pesticide production has also increased at an annual rate of approximately 11%, from 200,000 tons in the 1950s to over 5 million tons in the 2000s. Although pesticides play an important role in increasing crop yields and producing high-quality food, the increase in pesticide use has also brought some negative impacts on the environment and human health. According to statistics, 3 billion kilograms of pesticides are used annually worldwide, and only 1% of them are actually used.

In recent years, there have been numerous reports of pesticide contamination of surface and groundwater around the world. For example, in 2017, large amounts of herbicides contaminated between 37,000 and 500,000 square meters of wetlands in Saskatchewan, Canada, exceeding national standards [8]. In 2018, the U.S. Geological Survey (USGS) found multiple pesticides in more than 90% of water and fish samples collected from U.S. streams [9]. In the same year, pesticide pollution was also reported in China's Yongding River, and pollution levels were found to vary in different seasons [10]. Pesticide pollution in these aquatic environments not only directly affects local water quality, but is also transferred to other media (such as soil, atmosphere, and food chains) through evaporation, surface runoff, rainfall, etc., thereby causing more extensive indirect impacts on the ecological environment (Figure 1.1).

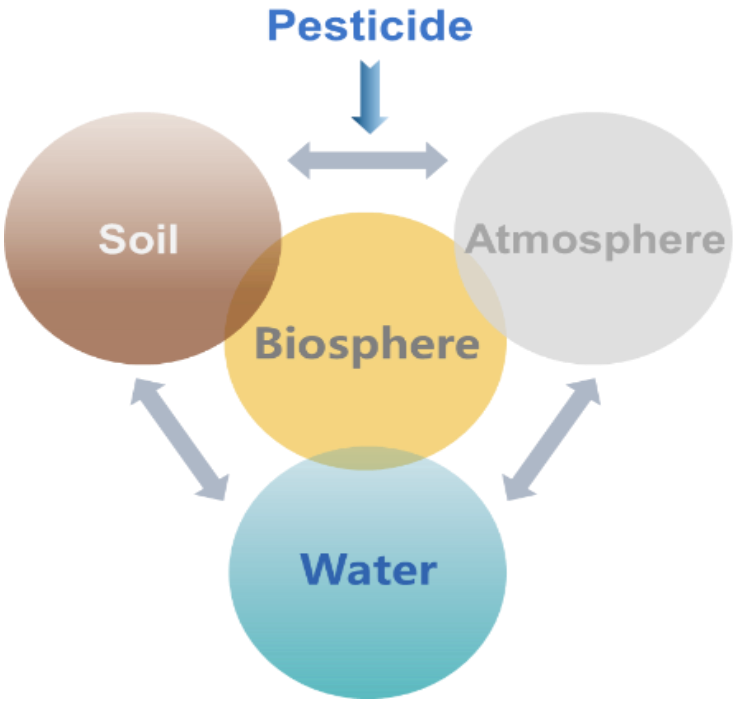

Figure 1.1 Schematic diagram of the migration paths of pesticide pollutants in the environment.

1.2 The hazards of pesticide water pollution

Humans are exposed to pesticides in a variety of ways, with varying degrees of exposure leading to varying effects. Excessive pesticide exposure is thought to cause a number of diseases, including non-Hodgkin's lymphoma [11], Parkinson's disease [12], and endocrine disruption [13]. Pesticides are also thought to cause cancer in humans; for example, glyphosate has been linked to breast cancer [14]. Many pesticides, such as paraquat, rotenone, and maneb, can induce reactive oxygen species (ROS)-mediated stress and neurodegenerative diseases. For example, Alzheimer's disease, one of the most common disabilities in the elderly, is characterized by abnormal deposition of beta-amyloid protein and is closely related to oxidative stress [15]. Long-term low-dose exposure to paraquat, dieldrin, organochlorine, and organophosphate pesticides

can induce ROS-mediated neurotoxicity and is positively correlated with the incidence of Alzheimer's disease [16]. In recent years, the problem of pesticide pollution in water has become increasingly serious. Therefore, how to efficiently remove pesticides and other organic pollutants from water bodies and reduce their impact on humans and ecosystems has become a current research hotspot and difficulty.

1.3 The main treatment methods for organic pollutants in water

Currently, the technologies and methods for treating organic pollutants such as pesticides mainly include three categories: biological treatment, physical treatment and chemical treatment.

1.3.1 Biological method

Biological treatment is an artificially enhanced biological treatment technology based on environmental self-purification. It utilizes the metabolic activity of microorganisms in the environment to oxidize and decompose organic pollutants in water, converting them into stable and harmless inorganic substances [17]. Common biological treatment methods include activated sludge and membrane bioreactors.

Activated sludge process, also known as aerobic biological treatment, mainly removes pollutants from water through biodegradation and sludge adsorption [18]. Biodegradation mainly removes antibiotics through two metabolic processes: microbial co-metabolism and microbial metabolism. In the former, antibiotics can be degraded by the action of corresponding enzymes secreted by microbial communities, while in the latter, microorganisms can use antibiotics as a carbon source and energy substrate for their growth [19]. Therefore, microorganisms can decompose and

transform antibiotics by themselves. It is reported that activated sludge treatment can be used to remove sulfonamide antibiotics, quinolone antibiotics and tetracycline antibiotics [20], [21]. Jilani et al. used the bacterial isolate IES-PS-1 to evaluate the potential of an activated sludge process for the degradation of the pesticide cypermethrin [22]. Experimental results showed that at a dose of 80 $mg \cdot L^{-1}$, the degradation rate reached 88%. Complete removal of 20 $mg \cdot L^{-1}$ of cypermethrin was achieved after 48 hours of treatment. However, in practical applications, the activated sludge process is limited by high costs, long cycle times, and the risk of microbial inactivation due to contaminants.

Membrane bioreactor (MBR) is a treatment process based on the combination of conventional activated sludge and membrane separation, which has three functions: biosorption, biodegradation and membrane separation. Compared with the activated sludge process, MBR has the advantages of long sludge retention time, small sludge volume and high suspended solids concentration [23]. Although some membrane structures cannot effectively remove antibiotics (such as microfiltration membranes and ultrafiltration membranes), they can intercept toxic substances in water, improve the favorable environment for microbial growth, and maintain high biomass concentrations. Therefore, biodegradation in membrane bioreactors is enhanced. Raghavan et al. studied the fate and removal behavior of 12 antibiotics in an osmotic membrane bioreactor (OMBR), and the overall removal rate of all antibiotics was as high as 77.7-99.8% [24]. Xiao et al. used an anaerobic membrane bioreactor to experimentally investigate the removal of five drugs [25]. Biodegradation was the primary removal mechanism for trimethoprim and sulfamethoxazole, with removal efficiencies of 93.3 ± 5.7% and 76.7 ± 14.6%, respectively. Although membrane

bioreactors offer high pollutant removal efficiencies, they also face challenges such as high cost and energy consumption, as well as reduced efficiency due to membrane fouling.

1.3.2 Physical method

Common physical treatment methods include membrane filtration and adsorption. Common membrane treatment processes include microfiltration, ultrafiltration, nanofiltration, and reverse osmosis membranes. Compared to microfiltration and ultrafiltration membranes, nanofiltration and reverse osmosis membranes have smaller pore sizes, with molecular weight cutoffs (MWCO) of 0.001 to 0.008 μm and less than 0.001 μm, respectively. They can more effectively intercept and remove water pollutants. Therefore, most common antibiotic treatments are also based on research on reverse osmosis and nanofiltration membranes [26], [27]. Alonso et al. developed a reverse osmosis membrane element that successfully removed ciprofloxacin from artificial seawater with a removal rate of greater than 90% [28]. Cheng et al. discovered that polyamide nanofiltration membranes can effectively separate tobramycin [29]. This is due to the high permeability of the membrane structure and its rejection of positively charged antibiotics. Under optimal conditions, the antibiotic retention rate reaches 96%. Membrane filtration is a green, harmless, and efficient treatment method, but membranes are expensive, most membranes are only disposable, and most membrane materials are polymers that are soluble in many organic solvents. Therefore, membrane filtration is not well suited for aqueous environments containing organic solvents.

Adsorption method mainly uses porous materials to adsorb pollutants in wastewater to achieve the purpose of water purification. The selection of adsorbent

plays a key role in the efficient adsorption process, because the specific surface area, pore size and functional groups carried on the surface of the adsorbent play a decisive role in adsorption. At present, common adsorption materials include activated carbon, bentonite, synthetic resin, graphene oxide, metal organic framework, etc [30]. Many researchers have studied the effectiveness of these common adsorbents in adsorbing pollutants. Wang et al. modified bentonite with octadecyl dimethyl betaine (BS-18) and studied the adsorption of tetracycline (TC) and norfloxacin (NOR) by the bentonite under different modification ratios, temperatures, pH values, and ionic strengths [31]. The results showed that the adsorption of TC by the amphiphilic BS-18-modified bentonite conformed to the Langmuir model, indicating monolayer adsorption. Lin et al. constructed a magnetically separable ethanolamine (AE)-functionalized graphene adsorbent (MAEGO) using organic covalent bonding, supramolecular self-assembly, and soft chemistry [32]. The synergistic effect between AE and Fe_3O_4 nanoparticles resulted in highly exposed adsorption sites within MAEGO, significantly improving pollutant adsorption and transport efficiency. Within 5 minutes, MAEGO achieved an adsorption capacity of 315.25 $mg \cdot g^{-1}$ for tetracycline (TC), and when TC adsorption reached equilibrium (1440 min), the removal efficiency reached 97.80%. Adsorption methods offer advantages such as ease of operation and low environmental and equipment requirements [33]. However, regeneration of the adsorbent is a difficult problem. Consequently, cost constraints have long hampered the development of adsorption methods.

1.3.3 Chemical method

Chemical treatment primarily involves chemical reactions between chemical oxidants or reactive oxygen species and pollutants, disrupting their molecular structure and further converting them into harmless small molecules or completely mineralizing them into H_2O and CO_2, ultimately achieving the goal of pollutant degradation or harmlessness. Common chemical treatment methods include oxidation with strong oxidants (such as chlorination) and advanced oxidation processes (AOPs). Chlorine is the most widely used disinfectant and oxidant in wastewater treatment. However, the treatment process is prone to the formation of potentially toxic disinfection byproducts (such as chlorates, chlorites, and methyl halides) [34]. In recent years, AOP processes have attracted attention due to their simplicity and environmental friendliness, mainly including photocatalytic oxidation, electrochemical oxidation, ozone oxidation, Fenton reaction and Fenton-like reaction.

1.4 Advanced Oxidation Processes

1.4.1 Electrochemical oxidation and ozone oxidation technologies

The electrochemical oxidation process of pollutants mainly refers to the process of degrading organic pollutants by utilizing hydroxyl radicals (·OH) or other oxidative active substances generated by electrochemical reactions at the anode. It has the advantages of high yield, high product purity, and easy operation. For example, Tang et al. synthesized $MnFe_2O_4$ nanoparticles and added them to an electrochemical oxidation system with persulfate to degrade TC [35]. After 60 minutes of treatment, the TC removal rate reached 86.23%. However, current electrochemical oxidation methods are currently limited in practical application by high power consumption and

low current efficiency, requiring further improvement.

Ozone oxidation is also a common method for treating organic matter. Xu et al. prepared Cu-Al layered double hydroxides (Cu-Al LDHs) by coprecipitation and used them as catalysts for the heterogeneous ozone-catalytic oxidation of ciprofloxacin [36]. Under optimal conditions (pH = 9, LDH dosage 0.79 $g \cdot L^{-1}$, and ozone dosage 61.2 $mg \cdot min^{-1}$), the ozone-catalytic oxidation achieved a total organic carbon (TOC) removal rate of 72% for ciprofloxacin. Furthermore, electron paramagnetic resonance (EPR) measurements confirmed the involvement of hydroxyl radicals, superoxide radicals, and singlet oxygen in the process. Li et al. prepared a Co-Mn/CeO_2 composite material using a sol-gel method and used it as a highly effective catalyst for the ozone oxidation of norfloxacin (NOR) [37]. At Co-Mn/CeO_2 composite concentration of 0.60 $g \cdot L^{-1}$, the ozone oxidation method achieved a NOR removal rate of 87.24%. Although ozone has a strong oxidizing capacity and is not prone to secondary pollution during the reaction, its unstable nature, high cost, and high energy consumption make it difficult to scale up this method for industrial use.

1.4.2 Photocatalytic technology

Photocatalytic oxidation refers to a chemical oxidation reaction that occurs under light irradiation. The reaction involves using solar energy to induce excited electrons and holes in a photocatalyst (usually a semiconductor). These electrons and holes gradually react with oxygen or hydrogen peroxide to form reactive oxygen species (ROS), which then undergo further oxidation [38]. For example, Nguyen et al. prepared Ni-doped TiO_2 (Ni-TiO_2) photocatalysts and studied their performance against antibiotic pollutants such as cephalexin (CF) and tetracycline (TC) [39]. The results showed that Ni doping enhanced the photocatalytic performance of TiO_2. In

photodegradation experiments, Ni-TiO_2 achieved a photocatalytic degradation efficiency of 93.6% for CF and 82.5% for TC. Lin et al. successfully doped the metal-organic framework UiO-66 with Fe using a solvothermal method [40]. Fe-UiO-66 exhibited excellent photocatalytic degradation of sulfonamide antibiotics in water. Under visible light, Fe-UiO-66 achieved a degradation rate of 89.9% within 300 minutes. Photocatalytic oxidation, with its high efficiency and harmless reaction, is a promising technology for water pollution treatment.

1.4.3 Fenton (like) technology

Among various advanced oxidation technologies for wastewater treatment, Fenton oxidation is one of the most commonly used reactions. Its mechanism generally involves the reaction of Fe^{2+} ions with H_2O_2 under acidic conditions to form ·OH radicals with strong oxidizing power (Equation 1-1). These ·OH radicals then oxidize and degrade organic pollutants into harmless substances (Equations 1-3 and 1-4). However, the Fenton reaction requires the addition of large amounts of Fe^{2+} to treat wastewater. Excessive Fe^{2+} additions can easily generate iron sludge, leading to secondary contamination of water resources [41]. Therefore, in order to improve the performance of the Fenton reaction and reduce the use of Fe^{2+} ions, most pollutant treatment research in recent years has been based on Fenton-like oxidation reactions.

$$Fe^{2+} + H_2O_2 \rightarrow Fe^{3+} + \cdot OH + OH^- \quad (1-1)$$

$$Fe^{3+} + H_2O_2 \leftrightarrows Fe^{2+} + H^+ + HO_2 \cdot \quad (1-2)$$

$$RH + \cdot OH \rightarrow H_2O + R \cdot \quad (1-3)$$

$$R + \cdot OH \rightarrow \cdot ROH \quad (1-4)$$

The principles of Fenton-like reactions are basically the same as those of Fenton reactions (see Equation 1-2), including homogeneous Fenton reactions and

heterogeneous Fenton reactions (such as photo-Fenton reactions and electro-Fenton reactions). Liu et al. used FeO_x nanocluster-modified TiO_2 nanofiber (FeO_x-TNFs) heterostructures to efficiently photocatalytically remove the antibiotic norfloxacin (NOR) under white light LED irradiation [42]. In the visible light-driven Fenton-like photocatalytic reaction, the NOR removal rate reached 92% within 5 h. Lv et al. synthesized Fe-0@Fe_3O_4 nanoparticles with superior dispersibility and stability compared to single nanoparticles of zero-valent iron [43]. They combined them with H_2O_2 to form a heterogeneous Fenton-like system, which they applied to the degradation of 2,4-dichlorophenoxyacetic acid (2,4-D). 2,4-D was completely removed within 90 minutes, with nearly 66% of the 2,4-D mineralized. Heterogeneous Fenton-like systems offer advantages such as high degradation efficiency and reduced secondary pollution, effectively addressing the large sludge volumes and narrow pH range of application inherent in traditional Fenton processes. Therefore, heterogeneous Fenton-like reactions can be an effective means of removing pollutants from water.

1.5 Functional materials for water purification

1.5.1 Semiconductor catalyst materials

Selecting viable catalyst materials is key to utilizing advanced oxidation technologies to degrade pollutants. Semiconductor materials such as TiO_2 [44], ZnO [45], Co_3O_4 [46], SnO_2 [47], CdS [48], and g-C_3N_4 [49] offer advantages such as high reactivity, high functionality, and high stability, making them effective catalysts. These semiconductors can be excited by light with energies above their band gaps, generating electron-hole pairs that participate in redox reactions.

Among many semiconductor catalysts, TiO_2 has become a widely studied

photocatalyst material due to its simple and low cost preparation method, strong oxidation ability, stable physical and chemical properties, anti-photocorrosion ability and non-toxicity [50], [51]. However, TiO_2 has several drawbacks that limit its widespread application. For example, due to its band gap of 3.2 eV, TiO_2 absorbs only 3-5% of sunlight, making it excitable only by ultraviolet light. Consequently, researchers have attempted to improve its photocatalytic properties by modifying TiO_2 using various methods, such as dye sensitization, doping, semiconductor composites, and precious metal deposition. For example, Sheng et al. found that Pd-modified TiO_2 showed higher activity for the photocatalytic oxidation of NO [52]. Brundabana Naik et al. synthesized S- and N-doped mesoporous TiO_2 nanocomposites via a template-free homogeneous coprecipitation technique [53]. In the degradation of methyl orange and phenol under sunlight, SNTs exhibited approximately two times higher photocatalytic activity than single-N-doped or S-doped mesoporous TiO_2 and three times higher than commercial P25. This is attributed to the synergistic effect of S and N on the TiO_2 lattice. The light absorption and charge transfer mechanism in the catalyst is shown in Figure 1.2. The sulfate species anchored on the TiO_2 act as a catalyst, increasing surface acidity, participating in the separation and transfer of charge carriers, increasing surface area, and inhibiting phase transitions, thereby enhancing photocatalytic activity.

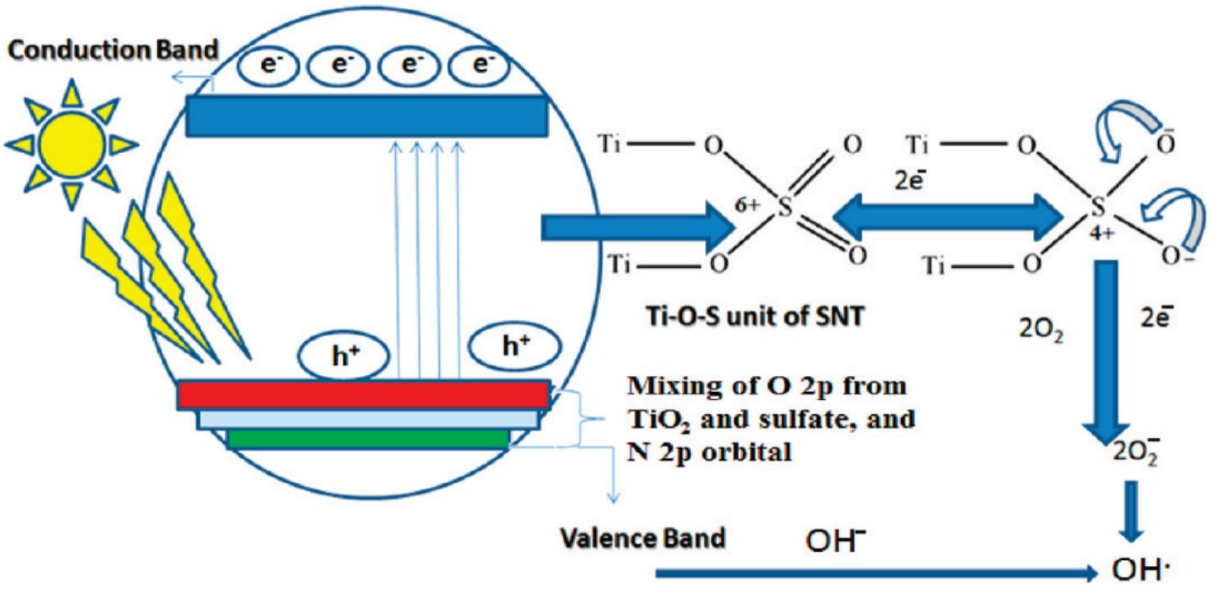

Figure 1.2 Mechanism of Light Absorption and Charge Transfer in the Catalyst [53].

Prabakaran et al. manipulated the formation of oxygen vacancies by adding Y^{3+} and rGO nanosheets to TiO_2 nanostructures, resulting in favorable electronic properties [54]. Y^{3+} infiltrates the TiO_2 lattice and combines with rGO to form defects. The increased Y^{3+} reduces oxygen in the lattice, leading to an increase in electron concentration. The presence of rGO facilitates charge carrier mobility, significantly enhancing the conductivity of the nanocomposite. As shown by EIS results, the addition of rGO increases electron lifetime and reduces charge transfer resistance, ultimately enhancing the optical and electrical properties of TiO_2.

1.5.2 Metal organic frameworks

Many traditional semiconductors have been reported to possess photocatalytic properties. However, due to the limited visible light utilization and inefficient separation of photogenerated electrons and holes faced by these photocatalysts, the development of new materials is urgent. Metal-organic frameworks (MOFs) are

materials with three-dimensional porous structures that use metal ions as templates and organic ligands as linkers, as shown in Figure 1.3 [55].

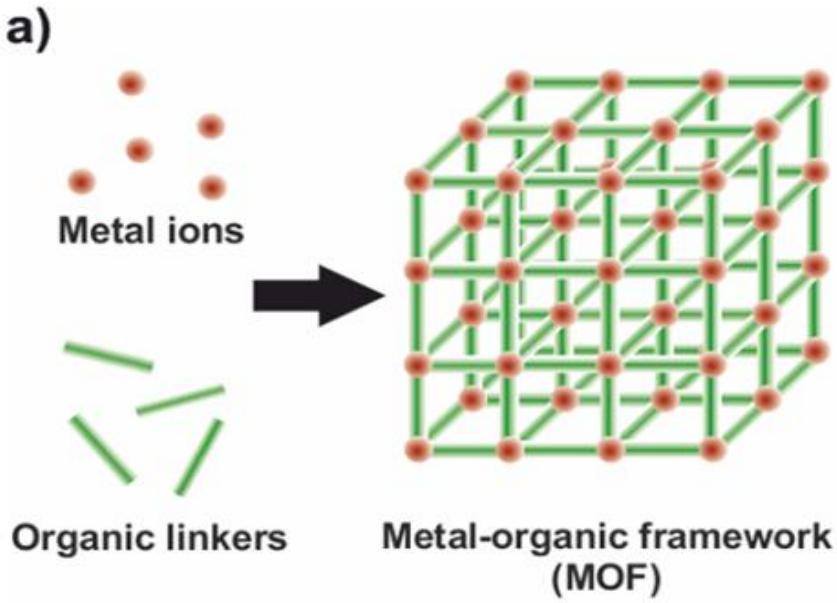

Figure. 1.3 Schematic diagram of MOF structure [55].

Because MOFs have the characteristics of high specific surface area, high porosity, controllability, and exposed active sites [56], they are widely used in the fields of gas storage [57], chemical sensors [58], and drug delivery [59]. Among the numerous MOFs, common metal centers include Cu(II), Zn(II), Fe(III), Al(III), Ti(III), and Zr(IV). Common organic ligands include imidazoles, carboxylates, sulfonates, and phosphates, such as 2-methylimidazole, terephthalic acid, 2-aminoterephthalic acid, and tris-benzoic acid. Based on naming conventions, MOFs can be divided into the following categories: IRMOFs, ZIFs, PCNs, MILs, and the UiO series (Table 1.1).

Table 1.1 Classification of metal ions and organic ligands for different types of MOFs

Types of MOFs	Metal ions	Organic ligands	Representative materials
IR-MOFs	Zn	Terephthalic acid	IRMOF-3, MOF-5
ZIFs	Zn, Co	Imidazole	ZIF-8, ZIF-90, ZIF-71, ZIF-67, ZIF-7
PCNs	Cu, Pt, Zr	Porphyrin	PCN-333, PCN-224, PCN-222, PCN-57
UiOs	Zr, Hf	Terephthalic acid, trimesic acid	UiO-66, UiO-67
MILs	Fe, Cr and other transition metals and lanthanide elements	Fumaric acid, glutaric acid, terephthalic acid, trimesic acid	MIL-101, MIL-100, MIL-53, MIL-88, MIL-125

In 2007, MOF-5 was discovered to possess semiconductor properties, demonstrating similar photocatalytic activity for phenol degradation to P25 [60]. Research has shown that most MOFs, such as MIL-53 and MIL-100, possess semiconductor properties. MOFs can also form heterostructures by combining with other semiconductors, effectively promoting photoinduced electron migration and carrier separation, thereby increasing light utilization. Among them, Ti-based and Fe-based MOFs are the most widely studied, and in recent years they have also attracted much attention in the fields of photocatalysis and photo-Fenton [61].

1.5.2.1 Ti-MOF

MIL-125(Ti) is the first porous crystalline carboxylate-based Ti-MOF. It is a highly crystalline MOF synthesized by Ferey and colleagues in 2009 via a direct solvothermal method [62]. It uses Ti as the metal central ion and 1,4-benzenedicarboxylic acid (H_2BDC) as a ligand. The Ti−O clusters form strong bonds with the BDC ligands to form a stable interconnected octameric ring framework structure, resulting in a high specific surface area and excellent photocatalytic performance. However, pure MIL-125(Ti) photocatalysts are only effective in the ultraviolet region and are unstable during photochemical operations in aqueous solutions. Therefore, MOFs have been used directly as supports, and their catalytic performance has been enhanced through modification methods such as metal loading and doping, organic ligand modification, and multiple catalyst combinations. Rational design of organic ligands can increase carrier lifetime and, to a certain extent, narrow the band gap, thereby enhancing visible light absorption efficiency. Functional groups can be introduced into organic linkers, with $-NH_2$ being the most common functional group, effectively enhancing visible light absorption in MOFs. This introduction yields NH_2-MIL-125(Ti), a crystalline structure identical to MIL-125(Ti) composed of Ti_8O_8 clusters and 2-aminoterephthalic acid linkers, and has been extensively studied. For example, Fu et al. obtained amino-modified NH_2-MIL-125(Ti) by changing the ligand from terephthalic acid to 2-aminoterephthalic acid during the preparation process [63]. It can efficiently convert CO_2 into HCOO- under visible light irradiation, showing the potential of MOF as a photocatalyst for reducing CO_2 (Figure.1.4).

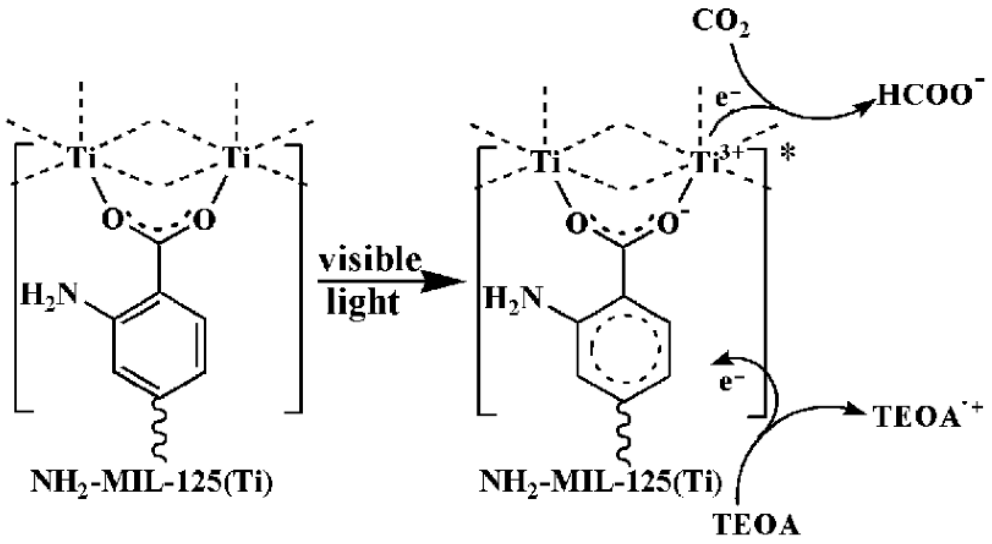

Figure.1.4 Mechanism of photocatalytic reduction of carbon dioxide by NH_2-MIL-125(Ti) under visible light irradiation [63].

Yin et al. self-assembled Bi_2WO_6 nanosheets onto NH_2-MIL-125(Ti) to construct a novel NH_2-MIL-125(Ti)/Bi_2WO_6 composite [64]. They demonstrated that photoexcited charge carriers can effectively separate and transfer between the two components. The composite exhibited enhanced photocatalytic activity for the removal of rhodamine B (RhB) and tetracycline (TC) under visible light irradiation. Figure 1.5 illustrates the degradation mechanism of the composite. The introduction of NH_2-MIL-125(Ti) into Bi_2WO_6 enhances visible light absorption and accelerates charge carrier separation and transfer. Superoxide radicals ($\cdot O_2^-$) and holes (h^+) play a dominant role in the photocatalytic degradation of pollutants.

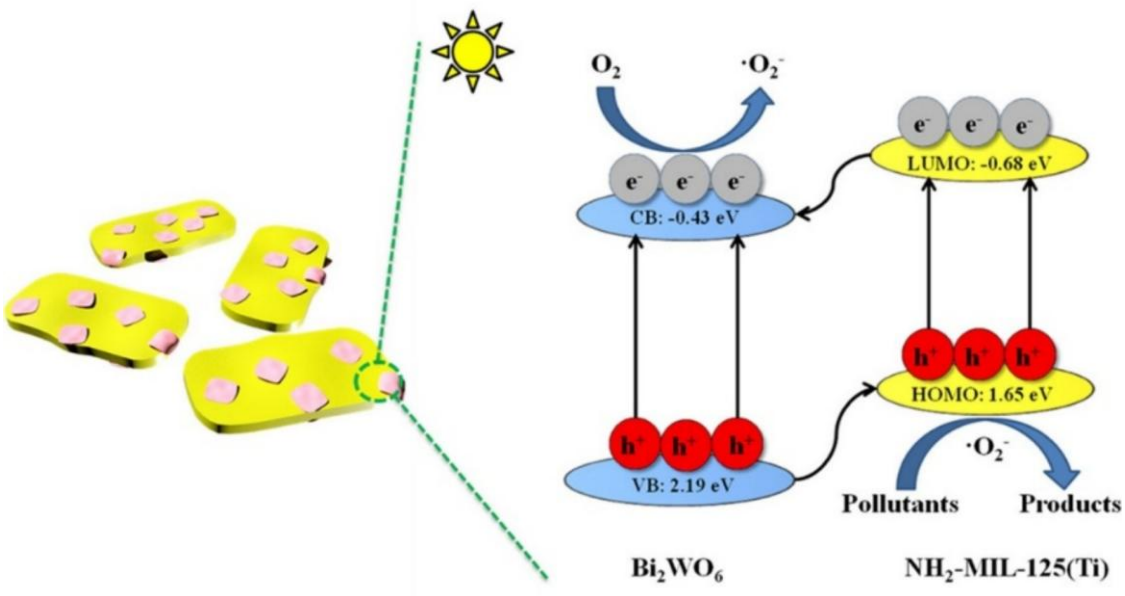

Figure. 1.5 NH_2-MIL-125(Ti)/Bi_2WO_6 photocatalytic mechanism [64].

Therefore, to construct a new type of Ti-MOFs photocatalyst, it should have the advantages of a wider absorption range of visible light, higher electron-hole separation efficiency and excellent photocatalytic efficiency.

1.5.2.2 Fe-MOF

Iron-based metal-organic frameworks (Fe-MOFs) have recently become a hot topic due to their high surface area and porosity, environmental friendliness, low cost, ease of separation, chemical stability, high Earth abundance, and strong absorption in the visible light region due to the presence of Fe−O clusters. Several Fe-based MOFs, such as MIL-100(Fe), MIL-53(Fe), MIL-101(Fe), MIL-88A(Fe), and MIL-88B(Fe), have been shown to be visible-light-driven photocatalysts [61], [65]. In addition, due to the abundant Fe-O clusters and visible light activity of Fe-MOF, Fe-MOF can use light energy to drive the Fe^{2+}/Fe^{3+} cycle and react with H_2O_2, thereby achieving better photo-Fenton oxidation activity.

As an eco-friendly and low-toxic material, MIL-88(Fe) can be used as an efficient

AOPs catalyst for the degradation of organic pollutants and as an efficient adsorbent for the removal of heavy metals and organic pollutants. For example, Katrien et al. successfully evaluated the photocatalytic performance of MIL-88B(Fe) by removing a rhodamine solution and demonstrated the excellent photocatalytic activity of this Fe(III)-based MOF in the visible light region [66]. Yan et al. noted that the implantation of carbon nanotubes significantly contributes to the formation and separation of charge carriers in pure MIL-101(Fe), resulting in high ciprofloxacin removal efficiency [67]. However, these additional materials may clog pores or metal sites in Fe-based MOFs, resulting in insufficient contact with pollutants. Therefore, researchers can modify Fe-based MOFs to enhance light absorption and increase active sites. Li et al. prepared TiO_2 nanoparticles anchored on NH_2-MIL-88B(Fe) using a one-step solvothermal method, enhancing their adsorption and photocatalytic performance [68]. TiO_2@NH_2-MIL-88B(Fe) exhibited excellent adsorption and photodegradation performance for methylene blue (MB) fuel in wastewater under visible light irradiation. Photocurrent analysis and electrochemical impedance spectroscopy confirmed the synergistic effect between TiO_2 and NH_2-MIL-88B(Fe), demonstrating that heterojunctions can enhance photocatalytic performance.

However, Fe-MOFs have disadvantages such as a narrow light absorption range or a high recombination rate of photogenerated carriers, and their light energy utilization and catalytic efficiency need to be improved.

1.6 Modification methods of metal organic frameworks

Despite the numerous advantages of most MOFs, their practical applications remain limited. Due to their wide bandgap, some MOFs can only absorb ultraviolet

light and lack response in the visible region. Furthermore, the high electron-hole recombination rate and poor chemical stability of pure MOFs limit their application. Therefore, they need to be modified to produce materials with higher catalytic activity. Modification and structural engineering of MOFs, such as elemental doping, organic ligand modification, heterojunction formation with other semiconductors, and defect engineering, can yield MOFs with even superior catalytic performance.

1.6.1 Element doping

Rationally tuning the chemical composition of photocatalysts through elemental doping can effectively amplify sunlight absorption, accelerate charge transfer, and promote rapid surface reaction kinetics [69]. Metals (such as Fe, Cu, Co, and Ni), rare earth metals (such as Er, Ce, and La), and non-metallic elements (such as C, N, S, and P) can be incorporated. The addition of these elements can also create lattice defects that favor the formation of active centers.

Han et al. introduced Cu^{2+} into the porphyrin core of PCN 224 via a simple hydrothermal method. MOFs doped with 10% Cu^{2+} exhibited an antibacterial efficacy of 99.71% against Staphylococcus aureus after 20 minutes of light irradiation, effectively killing bacteria and accelerating wound healing [70]. Figure 1.6 shows the preparation process and crystal structure of Cu-doped MOFs, as well as the mechanism by which they achieve synergistic bacterial killing through enhanced photocatalytic performance and photothermal effects. This mechanism is based on the fact that the incorporation of Cu^{2+} into MOFs captures electrons, thereby inhibiting the recombination of photogenerated electron-hole pairs.

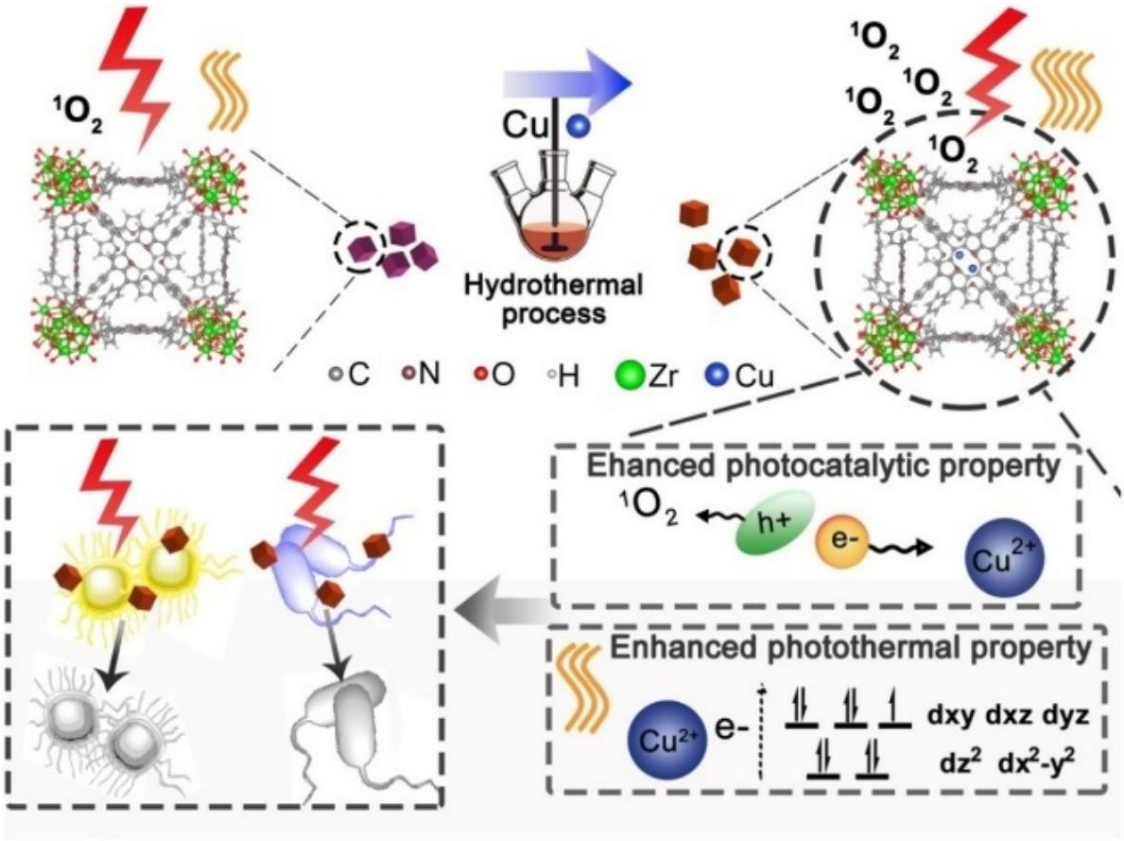

Figure. 1.6 The preparation procedures and the crystal structure of Cu doping MOFs [70].

Li et al. used a sulfur-doped MOF as a precursor and further synthesized a MOF-derived sulfur-doped NiFeP structure [71]. Due to the tunable electronic structure, partial substitution of phosphorus with sulfur improved the performance of the NiFeP catalyst in both the oxygen evolution reaction (OER) and hydrogen evolution reaction (HER). The optimized CCS-NiFeP-10 achieved a current density of 10 mA cm^{-2} in the OER with an overpotential of 201 mV, outperforming most NiFe-based catalysts.

To improve the surface charge separation and cycling stability of MIL-125(Ti), Gao et al. proposed an in situ co-doping strategy with pyrrole N/Zn. They obtained pyrrole N/Zn co-doped MIL-125(Ti) for the degradation of vapor acetaldehyde under high humidity conditions. The results showed that the synergistic effect of N/Zn co-

doping enhanced the activation of $\cdot O_2^-$ and ·OH radicals, resulting in a 10-fold faster reaction kinetics for CH_3CHO degradation in humid air than that of MIL-125(Ti).

1.6.2 Building composite materials

MOFs are often combined with other photocatalytic semiconductor materials to form heterojunctions. The synergistic effect between the two accelerates charge transfer across the interface, shortening the transmission distance and thus improving the separation efficiency of photogenerated electrons and holes. Furthermore, heterojunctions can extend the absorption range into the visible light region, thereby enhancing catalytic performance. For example, Wang et al. combined BUC-21 and N-$K_2Ti_4O_9$ via ball milling to produce a series of BUC-21/$NK_2Ti_4O_9$ composites [72]. They systematically studied the photocatalytic reduction of Cr(VI) using these composites. The introduction of N-$K_2Ti_4O_9$ into BUC-21 broadened its white light absorption region and suppressed the recombination of photogenerated electrons and holes. BUC-21 and N-$K_2Ti_4O_9$ form a traditional heterojunction structure, and a mechanism for the photocatalytic reduction of Cr(VI) under white light was proposed, as shown in Figure 1.7. BUC-21 and N-$K_2Ti_4O_9$ are excited by white light, generating photogenerated electrons and holes. The photogenerated electrons migrate from the conduction band of BUC-21 to that of N-$K_2Ti_4O_9$, where they accumulate electrons in the conduction band of N-$K_2Ti_4O_9$, promoting the reduction of Cr(VI) to Cr(III).

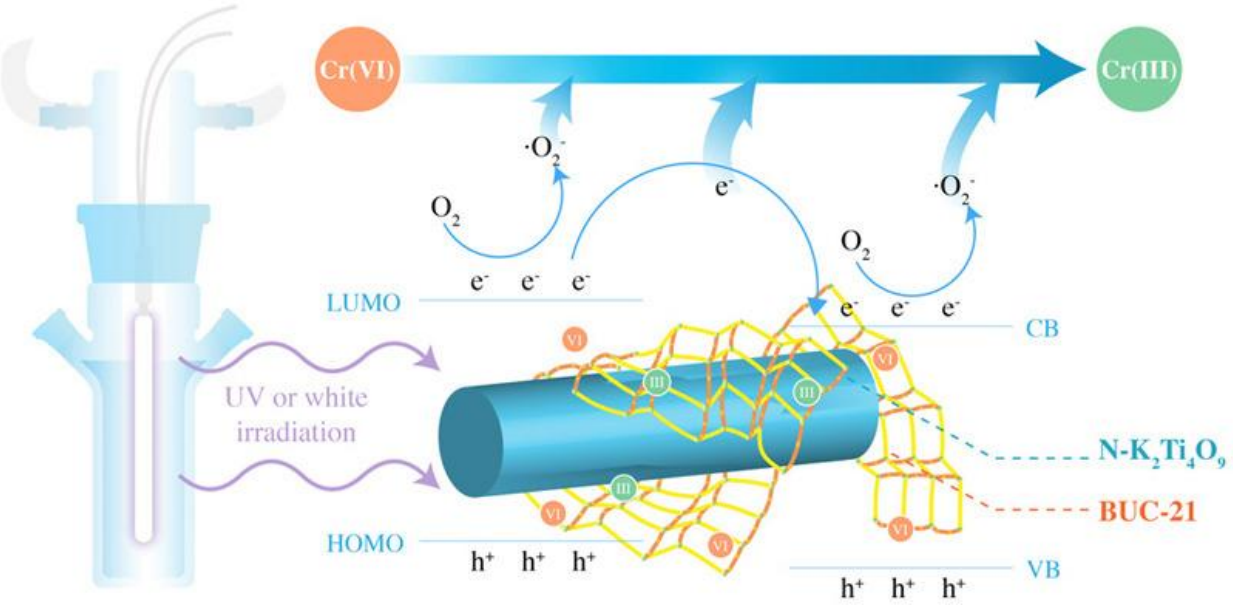

Figure. 1.7 Mechanism of photocatalytic reduction of hexavalent chromium by BUC-21/N-$K_2Ti_4O_9$ under white light [72].

Hu et al. introduced MIL-88B(Fe) into Bi_2WO_6 flower balls via a two-step solvothermal method, constructing an efficient visible-light-active Z-type heterojunction MIL-88B(Fe)/Bi_2WO_6 composite [73]. The optimally proportioned Bi_2WO_6/MIL-88B(Fe) composite achieved a TC removal efficiency of 96.40% within 90 minutes. As shown in Figure 1.8a, under visible-light irradiation, both Bi_2WO_6 and MIL-88B(Fe) were photoexcited and generated electron-hole pairs. The CB potential of Bi_2WO_6 is lower than the redox potential required for the formation of $\cdot O_2^-$, while the VB potential of MIL-88B(Fe) (2.02 eV) is lower than the hydroxyl redox potential. Therefore, this traditional carrier transfer separation mechanism is not conducive to the generation of reactive free radicals. Compared with the traditional heterojunction, Figure 1.8b also shows a more reasonable Z-type conduction mechanism. In this charge migration path, photoexcited electrons are directly transferred from Bi_2WO_6 to MIL-88B(Fe). The recombination rate of holes and photogenerated electrons in MIL-88B is

reduced, which is conducive to improving the separation of electron-hole pairs.

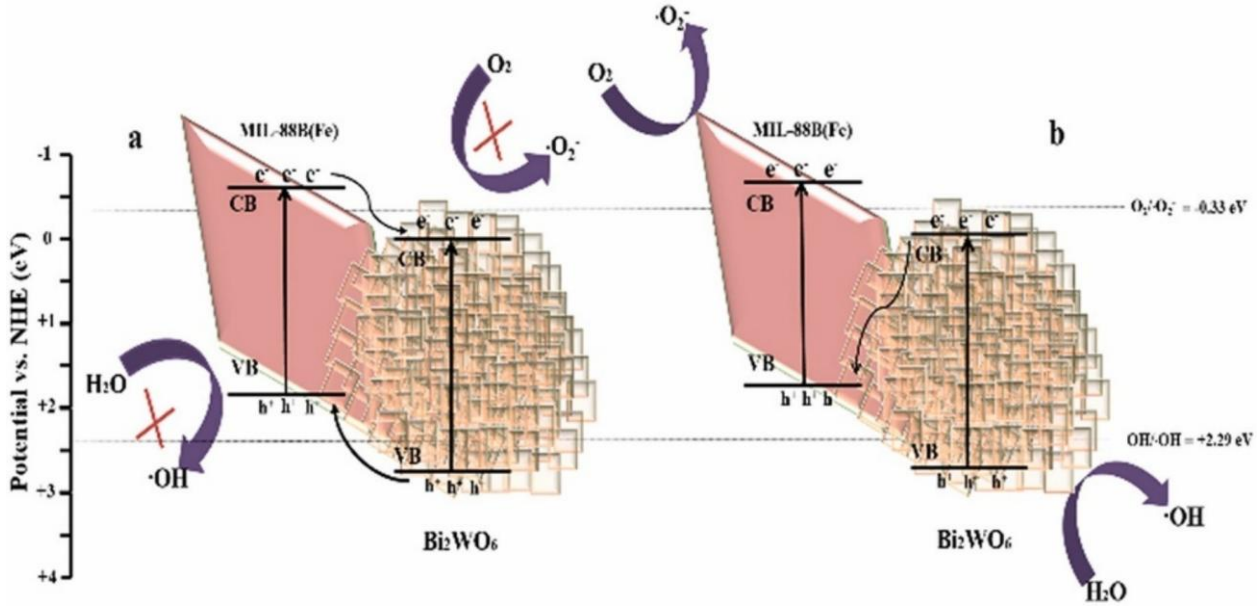

Figure. 1.8 Photocatalytic degradation of MIL-88B(Fe)/Bi_2WO_6 under visible light irradiation [73].

Wei et al. prepared NH_2-UiO-66/PTCDA (NU100PX) composites by simple mechanical ball milling [74]. The NU100P10 photocatalyst exhibited superior Cr(VI) degradation performance under visible light irradiation compared to PTCDA, NH_2-UiO-66, and other NU100PX materials. PL, TRPL, and electrochemical measurements revealed that the enhanced photocatalytic performance was primarily due to the formation of a Z-scheme heterostructure that facilitated the enhanced motion of photoinduced electrons. Both pure PTCDA and NH_2-UiO-66 were excited by visible light, and photogenerated holes were more likely to be retained in the VB of PTCDA. Simultaneously, photoinduced electrons could migrate from the CB of PTCDA to the HOMO of NH_2-UiO-66, improving the separation of photogenerated electrons and holes.

1.6.3 Defective Engineering

Studies have shown that appropriate defect structures not only do not affect MOF stability but can also enhance their catalytic activity. This strategy, often referred to as defect engineering, can be categorized into ligand defects, metal defects, and metal cluster defects. By constructing defect structures, Wang et al. improved the photo-Fenton degradation performance of NH_2-MIL-88B(Fe) by 50% and the TOC removal rate by 41% (Figure 1.9) [75]. The defect structure of NH_2-MIL-88B(Fe) enhances its adsorption capacity for organic matter, light absorption, and photogenerated electron-hole separation efficiency. Furthermore, it enhances the Lewis acidity of the Fe site, promoting the Fe(III)/Fe(II) cycle.

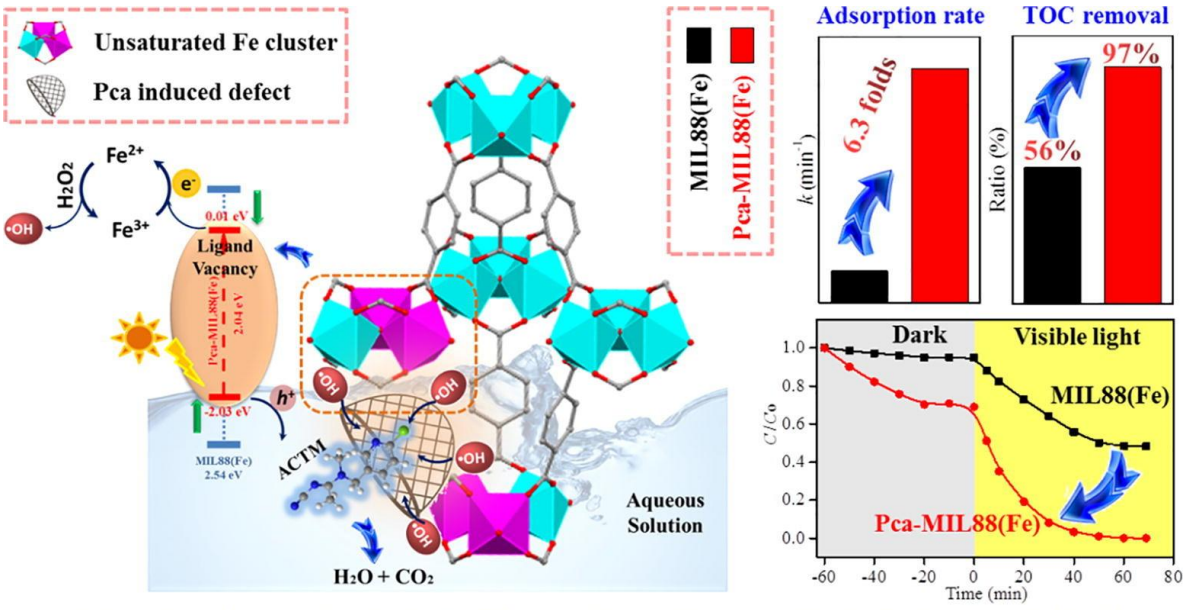

Figure. 1.9 Mechanism diagram of improving the photo-Fenton activity of NH_2-MIL-88B(Fe) by defect engineering [75].

To investigate the influence of defect levels on the Fenton-like properties of MOFs, Duan et al. synthesized MIL-100(Fe) with varying degrees of defect, replacing one -

COOH group of trimesic acid with functional groups such as -N, -NO_2, -Cl, or -OH [76]. Electrochemical reflection (EPR) measurements revealed that the defect levels of MIL-100(Fe) constructed with different ligands varied in order: D_N-MIL-100(Fe) > D_{NO_2}-MIL-100(Fe) > D_{Cl}-MIL-100(Fe) > D_{OH}-MIL-100(Fe) > MIL-100(Fe). Interestingly, the photo-Fenton activity was consistent with this order. Mechanistic studies revealed that the electronegativity of the functional group (the order of electronegativity corresponds to the degree of defect) altered the coordination bond energy between the ligand and the Fe-O cluster, leading to varying degrees of defect. However, increasing the degree of defect did not alter the stability of the MOFs. Increasing the defect density increases the charge density of the Fe sites, improves the Fe(III) reduction efficiency, and ultimately enhances the Fenton-like activity.

Furthermore, studies have shown that creating defects in MOFs can increase the exposure of metal sites, thereby improving the efficiency of MOFs in removing organic pollutants from water through Fenton-like reactions. For example, Cheng et al. promoted the adsorption and activation of PDS by MIL-101(Fe) through defect engineering (Figure 1.10), ultimately increasing the efficiency of photocatalytic PDS degradation of tetracycline [77]. Chen et al. prepared a defective MOF (Fe(II)-MOF-CA) using citric acid as a regulator and found that the presence of defects increased the exposed active sites, ultimately increasing the efficiency of activated persulfate degradation of SMX by 51.5% [78].

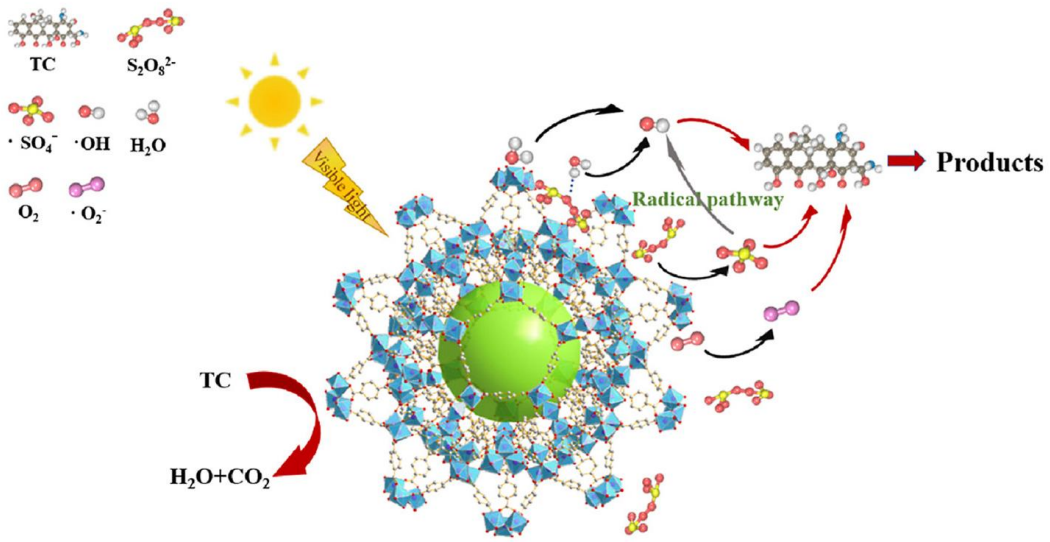

Figure. 1.10 Mechanism diagram of defect engineering promoting exposure of active sites of MIL-101 (Fe) to enhance adsorption and catalytic activity [77].

Conclusion of Chapter 1

According to surveys, organic pollution in water has seriously impacted the stability of the ecological environment. Pesticide-induced water pollution from agricultural production is particularly serious. These pesticide pollutants primarily include herbicides and insecticides, and have been detected in oceans, rivers, lakes, and even drinking water. Even at low concentrations, these pesticides can have significant adverse effects on the health of plants, animals, and even humans in the ecosystem.

However, pollutants such as pesticides, which exist at low concentrations in aquatic environments, are often difficult to remove. Therefore, research into advanced treatment technologies for these pollutants is crucial. This section reviews several common methods for removing organic pollutants from water, primarily biological, physical, and chemical methods. Biological methods include activated sludge and membrane bioreactors, physical methods primarily include membrane filtration and

adsorption, and chemical methods include oxidant oxidation and advanced oxidation processes. Based on a literature review, AOPs are the most advantageous method for removing low-concentration organic pollutants. Among these AOPs, heterogeneous photocatalysis and heterogeneous photo-Fenton processes offer unique advantages, such as their ability to utilize solar radiation, recyclable catalysts, and strong oxidizing properties. Through the above analysis, we identified research topics centered around photocatalysis and photo-Fenton catalysis.

We investigated catalyst materials suitable for photocatalysis and photo-Fenton catalysis. Comparing traditional semiconductor-based photocatalysts with MOF-based photocatalysts, we found that MOFs possess advantages such as light absorption capabilities approaching those of semiconductors, high surface area, and ease of modification. Therefore, we identified MOF-based photocatalysis and photo-Fenton catalysis as our primary research targets.

While MOFs offer numerous advantages, they also suffer from issues such as low photon quantum yield, short carrier lifetime, and low metal active site utilization. Therefore, we conducted a literature review of MOF modification methods. These methods include element doping, composite material construction, and defect engineering. Composite material construction can effectively promote carrier separation, while defect engineering can enhance active site utilization. Therefore, MOF modification through these methods is of great significance for promoting the application of MOF materials in water treatment.

Based on this analysis of the scientific literature, we identified the main research directions and formulated scientific tasks to achieve the established goals.

The results of the analysis of scientific literature conducted during the preparation of this section are presented in the following publications:

Research articles:

1. **Zhou Zhentao**, Tetiana Dontsova. Modification methods to enhance the performance of TiO_2 in photocatalysis. *Water and Water Purification Technologies. Scientific and Technical News*, 2023, 36(2): 40-57. https://doi.org/10.20535/2218-930022023299542.
2. Wang, W., Shi, H., Shi, H., Zhou, Z., Mao, L., Zhang, L., & Liu, X. Application of modified biochar in integrated pollution management for pesticides and antibiotics in water: Recent advances and future prospects. Environmental Research, 2025, 285: 122499. https://doi.org/10.1016/j.envres.2025.122499.

CHAPTER 2. Materials and Methods

2.1 Synthesis methods of titanium-based MOF (NH_2-MIL-125) and its composites (NH_2-MIL-125/TiO_2)

2.1.1 Synthesis of pure titanium-based MOF (NH_2-MIL-125)

A pure titanium-based MOF was synthesized using an improved solvothermal method [79]. As shown in Figure 2.1, amino-terephthalic acid (NH_2-BDC) (0.56 g, 3.1 mmol) was dissolved in a mixed solvent containing 36 mL of N-N-dimethylformamide (DMF) and 4 mL of methanol ($V_{DMF}/V_{Methanol}$ = 9:1), designated as Solution A. Titanium isopropoxide (TPOT) (0.6 mL, 2.0 mmol) was then added to Solution A. The resulting solution was sonicated and stirred for 15 minutes, designated as Solution B. Solution B was then transferred to a 100 mL polytetrafluoroethylene-lined steel autoclave and reacted in a forced-air drying oven at 150°C for 24 hours. After cooling, the yellow solid product was washed three times with DMF and twice with methanol, and then centrifuged. These samples were then activated in boiling DMF for 5 hours to remove any unreacted reactants remaining in the pores. Finally, they were dried in a vacuum oven at 60 °C for 12 hours to obtain the pure titanium-based MOF (NH_2-MIL-125).

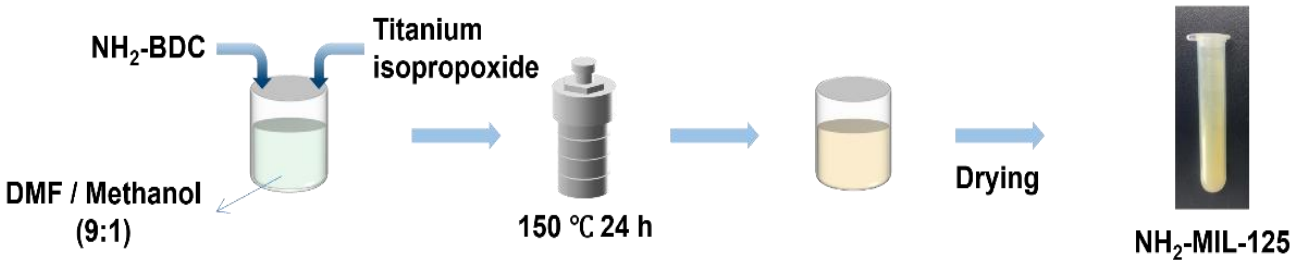

Figure 2.1 Synthesis steps of NH_2-MIL-125.

2.1.2 Synthesis method of NH_2-MIL-125/TiO_2 composite material

NH_2-MIL-125/TiO_2 composites were synthesized by a solvothermal method, as shown in Figure 2.2. Typically, a certain amount of commercial TiO_2 nanoparticles (P25) was dispersed in a mixture containing 36 mL of DMF and 4 mL of methanol. Ultrasonic stirring was performed for 30 min to completely disperse the TiO2 nanoparticles. Then, 0.56 g of NH_2-BDC (3.1 mmol) and 0.6 mL of NH_2-BDC (2 mmol) were added to the solution, and the mixture was stirred until the NH_2-BDC was completely dissolved. The mixture was then transferred to a 100 mL Teflon-lined stainless steel autoclave and reacted at 150°C in a forced-air drying oven for 24 h. After cooling to room temperature, the solid product was isolated by centrifugation, washed several times with DMF and methanol, and dried in a vacuum drying oven at 80°C overnight. The amount of P25 added was calculated based on the molar ratio of P25 to the precursor NH_2-BDC: 0.35:1, 1:1, 1.5:1, and 2:1, respectively.

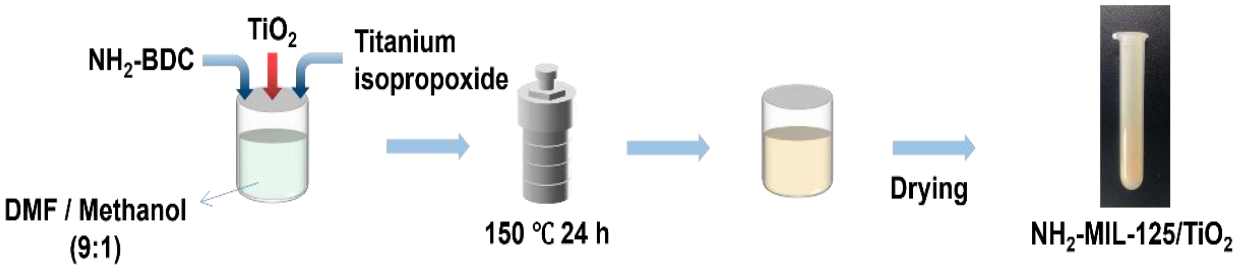

Figure 2.2 Synthesis steps of NH_2-MIL-125/TiO_2.

2.2 Synthesis method of iron-based MOF (MIL-88A) and its modified materials

2.2.1 Synthesis of pure iron-based MOF (MIL-88A)

MIL-88A(Fe) was prepared using a simple, green, low-temperature hydrothermal synthesis method [80], as shown in Figure 2.3. First, fumaric acid (5 mM, 580 mg) and

$FeCl_3 \cdot 6H_2O$ (5 mM, 1.3520 g) were dispersed in 30 mL of deionized water and stirred with a magnetic stirrer for 15 minutes to fully dissolve all the precursors. The resulting suspension was transferred to a 100 mL polytetrafluoroethylene reactor, which was then placed in a forced-air drying oven at 65°C for 12 hours. The resulting precipitate was then washed several times with deionized water and ethanol to remove impurities. Finally, the resulting material was transferred to a vacuum drying oven and dried at 80°C overnight to obtain the pure Fe-based MOF (MIL-88A(Fe).

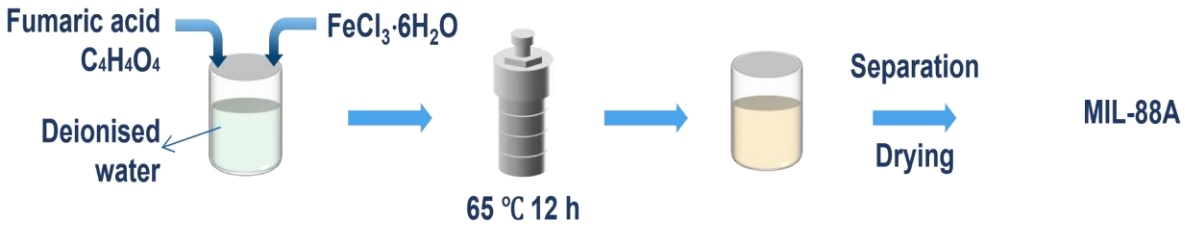

Figure 2.3 Synthesis steps of pure MIL-88A(Fe).

2.2.2 Synthesis of Tannic Acid Modified MIL-88A (MIL-88A@TA)

MIL-88A@TA is prepared by etching MIL-88A in an aqueous phase using tannic acid (TA) as an etchant. The process is shown in Figure 2.4. First, 800 mg of MIL-88A was added to 80 mL of deionized water and sonicated for 30 minutes to completely disperse the MIL-88A. The resulting suspension is designated Solution A. Then, 800 mg of tannic acid (TA) was added to 80 mL of deionized water and stirred using a magnetic stirrer until completely dissolved. The resulting reaction solution is designated Solution B. Subsequently, Solution B was slowly added dropwise to Solution A and stirred at room temperature for 8 hours. After the reaction was complete, the resulting solution was centrifuged (8000 rpm) to separate the solid product. The

solid product was then washed several times with deionized water and ethanol to remove impurities. Finally, the washed material was dried in a vacuum oven at 60°C overnight to obtain the final product (MIL-88A@TA).

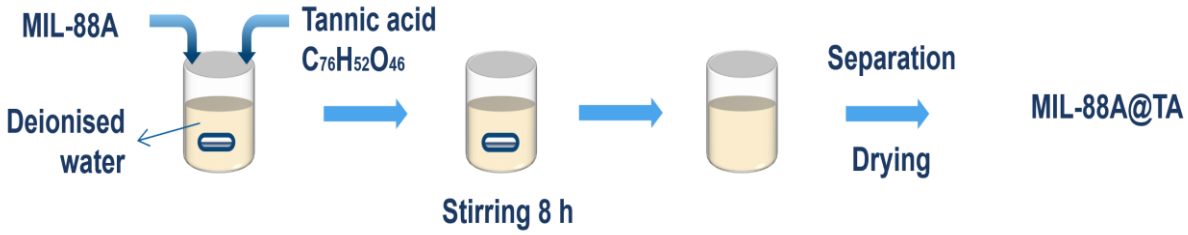

Figure 2.4 Synthesis steps of MIL-88A(Fe)@TA.

2.2.3 Synthesis method of modified MIL-88A with porous structure (MIL-88A@TA-X)

MIL-88A@TA-X was prepared by a calcination method, as shown in Figures 2.5. First, 200 mg of MIL-88A was poured into a covered alumina crucible and transferred to a tube furnace. The crucible was calcined for 240 min at a preset temperature of 200–400°C and a heating rate of 2°C/min. Nitrogen was continuously introduced during the calcination process. After the reaction, the resulting material was washed with deionized water to remove surface impurities. Finally, the washed product was transferred to a vacuum drying oven and dried overnight at 80°C to obtain MIL-88A@TA-X (where X represents the calcination temperature). Furthermore, MIL-88A-X was synthesized using the same conditions using pure MIL-88A, unmodified with tannic acid, as a precursor to compare the effects of tannic acid modification on the material.

Figure 2.5 Synthesis steps of MIL-88A(Fe)@TA-X.

2.3 Characterization of the synthesized materials

2.3.1 Morphology and phase structure characterization

2.3.1.1 Scanning Electron Microscopy (SEM) characterization

We characterized the prepared materials using a Regulus 8100 (Hitachi High-Tech, Japan) field emission scanning electron microscope (SEM). First, the powdered nanomaterials to be tested were dispersed in anhydrous ethanol and sonicated for 5 min to disperse the nanoparticles. Then, a silicon wafer of appropriate size was glued to the SEM sample stage with conductive adhesive, and a small amount of the dispersion was dripped onto the wafer by the drop-coating method and dried naturally. The samples were coated with a thin layer of gold using a sputter coater (Quorum Q150R ES, Quorum Technologies Ltd., East Sussex, UK) under a current of 20 mA for 60 s to improve conductivity and reduce charging during FE-SEM observation. After the sample is gold-sprayed, it is placed in a scanning microscope for testing.

2.3.1.2 High-resolution Transmission Electron Microscopy (HRTEM) characterization

Transmission electron microscopy (TEM) and energy-dispersive X-ray spectroscopy (EDS) were performed using a FEI Tecnai G2 F30 microscope (Thermo Fisher Scientific, USA) equipped with an Oxford XPLORE spectrometer.

Before TEM observation, the powder sample was ultrasonically dispersed in ethanol for 10 minutes to ensure a homogeneous suspension. A drop of the dispersion was placed on a carbon-coated copper TEM grid (300 mesh) and allowed to dry naturally. Morphological and structural analysis was performed using brightfield mode and high-angle annular dark-field scanning transmission mode (HAADF-STEM). Elemental distribution and composition were characterized using EDS elemental mapping and EDS line scans. Combining HAADF-STEM imaging with EDS analysis enables correlation of structural features with the spatial distribution of individual elements.

2.3.1.3 Specific surface area and pore size analysis

The specific surface area and pore size distribution of the samples were determined using nitrogen adsorption-desorption (77 K) using a fully automated surface and porosity analyzer (Builder 4200, Micromeritics Tristar II 3020 M). Micromeritics ASAP 2460 software was used for Brunauer-Emmett-Teller (BET) model fitting. The specific surface area results were retained to three significant figures, and the pore size distribution curve was calculated using the desorption branch data. The specific steps are as follows:

First, sample pretreatment was performed. Approximately 50-100 mg of powdered nanomaterial was placed in a sample tube and vacuum degassed at 120°C for 12 hours to completely remove surface-adsorbed moisture and impurities. Nitrogen adsorption-desorption isotherms were measured in a liquid nitrogen bath (77 K) over a relative pressure (P/P_0) range of 0.05-0.30 for BET surface area calculation (linear correlation coefficient $R^2 > 0.999$). Data from the full pressure range (0.01-0.99 P/P_0) were used for pore size distribution analysis.

2.3.1.4 X-ray Diffraction (XRD) analysis

The crystal structure of the sample was characterized using a Bruker D8 Advance X-ray diffractometer (Bruker, Germany), using Cu Kα radiation (λ = 1.5406 Å) as the X-ray source, with an operating voltage and current set to 40 kV and 40 mA, respectively. Before testing, 200 mg of powder sample was evenly spread in a glass sample holder (20 × 16 × 1 mm^3) and compacted using back pressure to ensure a flat surface. During testing, the sample stage was rotated at 15 rpm to minimize preferred orientation effects. Diffraction data were collected in the 5–80° (2θ) range, with a scan step size of 0.02°.

2.3.2 Chemical composition and structural characterization

2.3.2.1 Fourier Transform Infrared Spectroscopy (FTIR)

The chemical structure and functional group composition of the samples were analyzed using a Fourier transform infrared spectrometer (Nicolet 6700, Thermo Fisher Scientific, USA). Prior to testing, the samples were ground with dry potassium bromide at a mass ratio of approximately 1:100 and pressed into transparent thin sheets. All spectra were acquired at room temperature, with a scan range of 4000–400 cm^{-1} and a resolution of 4 cm^{-1}. A total of 32 scans were performed to achieve a high signal-to-noise ratio. To eliminate environmental interference, a background scan correction was performed before each measurement. The instrument was equipped with a DTGS detector, a KBr beam splitter, and operated under a dry air atmosphere to prevent water vapor interference. The vibrational modes of key functional groups were identified by comparison with a standard infrared spectral database.

2.3.2.2 X-ray Photoelectron Spectroscopy (XPS)

The elemental composition and chemical state of the samples were characterized using an X-ray photoelectron spectrometer (ESCALAB 250Xi, Thermo Fisher Scientific, USA). Before testing, 20 mg of the powdered nanocatalyst sample was accurately weighed and evenly dispersed on conductive carbon tape to ensure good electrical contact. Excitation was performed using a monochromatized Al Kα X-ray source (hv = 1486.6 eV, beam spot size 500 μm) under an ultrahigh vacuum environment (base pressure < 5×10^{-9} mbar). A wide scan spectrum (pass energy = 100 eV, step size 1.0 eV) was first acquired over the 0–1350 eV range for elemental composition analysis. Subsequently, high-resolution scans (pass energy = 20 eV, step size 0.05 eV) were performed in the characteristic peak regions of C 1s (282–298 eV), O 1s (528–538 eV), and Fe 2p (700–740 eV) to improve the signal-to-noise ratio. All binding energies were calibrated to surface contaminant carbon (C 1s = 284.8 eV). Data were processed using Avantage 5.992 software. Fine spectra were fitted using Shirley background subtraction and a Gaussian-Lorentzian (GL = 30%) function. The Fe 2p spectrum was subjected to spin-orbit splitting ($2p^{3/2}$ to $2p^{1/2}$ intensity ratio of 2:1, energy gap of 13.6 eV). The fitting results were semi-quantitatively analyzed to calculate the relative content of each chemical state. The chemical states of each element were confirmed by comparison with the NIST XPS database.

2.3.2.3 Thermogravimetric Analysis (TG)

The simultaneous thermal analysis (TG-DTA) test of the sample was carried out using a NETZSCH STA 449 F3/F5 thermal analyzer (NETZSCH, Germany). 50 mg of powder sample was accurately weighed and placed in an Al_2O_3 crucible. An empty Al_2O_3 crucible was used as a reference. The sample was heated from room temperature to 600°C at a heating rate of 10°C/min under a nitrogen atmosphere (flow rate of 50

mL/min). Thermogravimetric (TG) and differential thermal analysis (DTA) signals were collected simultaneously. During the test, a data acquisition frequency of 1 Hz was maintained to ensure measurement accuracy. All tests were baseline corrected and repeated three times to ensure data reliability.

2.3.2.4 Inductively Coupled Plasma Optical Emission Spectroscopy (ICP-OES)

The Fe content of the samples was determined using a Thermo ICAP PRO inductively coupled plasma optical emission spectrometer (ICP-OES, Thermo Fisher Scientific, USA). The instrument operating parameters were set as follows: RF power 1150 W, plasma gas flow rate 15 L/min, auxiliary gas flow rate 0.5 L/min, nebulizer gas flow rate 0.5 L/min, and cooling gas flow rate 12.5 L/min. Sample pretreatment was as follows: approximately 50 mg of nanopowder sample was accurately weighed and placed in a polytetrafluoroethylene digestion vessel. 8 mL of concentrated nitric acid and 2 mL of hydrofluoric acid were added, and complete digestion was performed using a microwave digestion system (200°C, 30 min). The digestion solution was then diluted to 50 mL with ultrapure water. The Fe analytical line was selected at either 238.204 nm or 259.940 nm. Quantitative analysis was performed using a three-point calibration curve (0.1, 1.0, and 10.0 mg/L), with a correlation coefficient $R^2 > 0.999$. Each sample was measured in triplicate, with a method blank and standard reference materials used for quality control. The spiked recovery of Fe was maintained between 90% and 110%. The final Fe content was calculated using the formula: C_{Fe} (mg/kg) = (C × V × f)/m, where C is the measured concentration (mg/L), V is the fixed volume (mL), f is the dilution factor, and m is the sample mass (g).

2.3.2.5 Electron Paramagnetic Resonance Spectroscopy (EPR)

Characterization was performed using an ER200-SRC (Bruker, Germany) electron paramagnetic resonance (EPR) spectrometer. The following test parameters were used: X-band microwave frequencies (~9.85 GHz) were used, with a modulation frequency of 100 kHz, a microwave power of 20 mW to avoid signal saturation, a magnetic field scan range of 0–7000 G, a resolution of 1.0 G, a scan time of 60 s, and three cumulative scans to improve the signal-to-noise ratio. For sample preparation, 10 mg of nanopowder was evenly loaded into a 4 mm quartz sample tube and measured at 77 K.

2.3.3 Optical characterization

2.3.3.1 UV-Vis Diffuse Reflectance Spectroscopy (UV-Vis DRS)

The ultraviolet-visible diffuse reflectance spectroscopy (UV-vis DRS) of the samples was tested using a Lambda 650S UV-visible spectrophotometer (Perkin Elmer, USA). The powdered samples were evenly filled in the sample cell. $BaSO_4$ was used as the 100% reflectance reference standard. The wavelength range of 200-800 nm was scanned at 0.5 nm intervals at a scanning speed of 240 nm/min. The diffuse reflectance signal was collected using an integrating sphere accessory. The sample chamber was kept at a constant temperature of 25°C during the test. All spectral data were converted to the Kubelka-Munk function using the instrument's built-in software to eliminate the influence of particle size and bulk density. The test was repeated three times to ensure data reproducibility.

2.4 Catalytic activity test method

2.4.1 Photocatalytic degradation activity test

Photocatalytic degradation experiments were conducted in a 250 mL quartz beaker equipped with a magnetic stir bar, using a 50W xenon lamp (Beijing Perfect Light PLS-SXE300E) to simulate sunlight (Figure 2.6). The photocatalytic performance of the prepared material was evaluated using the typical neonicotinoid insecticide imidacloprid as the target pollutant. 50 mg of the catalyst and 50 mL of an imidacloprid aqueous solution (initial concentration: 5 mg/L) were added to the reactor simultaneously. The mixed solution was stirred in the dark for 1 hour to achieve adsorption-decomposition equilibrium. The light source was then turned on to initiate and maintain the photocatalytic reaction for 80 minutes. During this time, 1 mL of sample solution was withdrawn regularly every 15 minutes using a syringe. The sample was then filtered through a 0.22 μm pore-size polyester sulfone membrane to separate the catalyst. The filtered solution was transferred to a 2 mL brown vial and stored at 4°C until analysis.

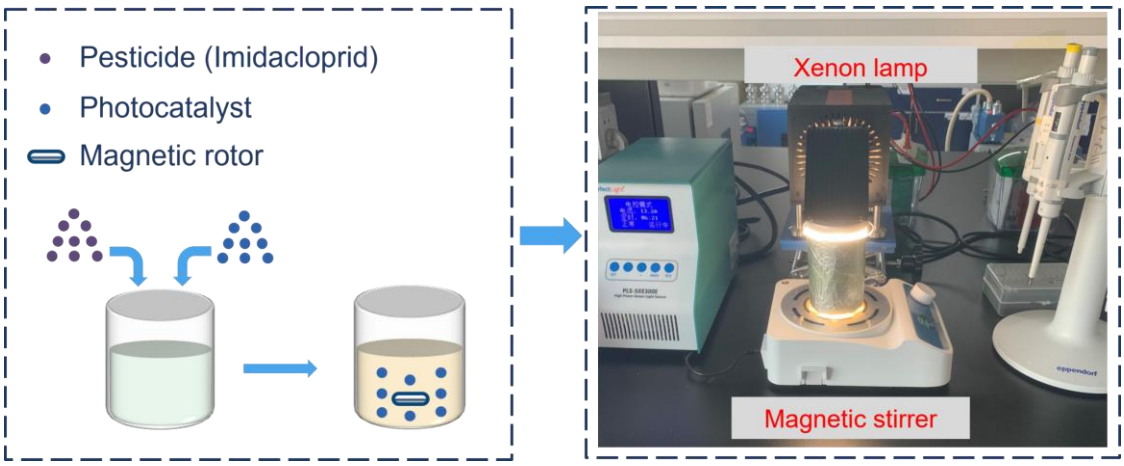

Figure 2.6 Photocatalytic experimental process and experimental equipment.

2.4.2 Heterogeneous Photo-Fenton degradation activity test method

Batch experiments were conducted in a 200 mL beaker equipped with a circulating condenser nest, which maintained a temperature of 20°C during the catalytic reaction. Visible light irradiation was simulated using a 50 W xenon lamp (Beijing Baofeilai Technology Co., Ltd., with a filter with a wavelength of $\lambda > 420$ nm to remove UV light) (Figure 2.7). The photo-Fenton catalytic activity of the materials was tested using the typical herbicide atrazine as the target pollutant. Unless otherwise stated, the atrazine (ATZ) concentration was 10 mg/L. Before degradation, 20 mg of the catalyst was added to 50 mL of the ATZ solution and stirred for 60 minutes to achieve adsorption-desorption equilibrium. Subsequently, the xenon lamp was turned on, and the reaction was initiated by adding 100 μL of H_2O_2 to the solution containing the catalyst and ATZ. During the reaction, 1 mL of the reaction solution was collected every 5 minutes and immediately quenched with an excess of $Na_2S_2O_2$. The sample solution was then filtered using a polyethersulfone filter membrane (0.22 μm) to remove the solid catalyst and transferred to an amber vial and stored at 5 °C until analysis. All experiments were performed three times, and the error bars in the figures represent the standard deviation of the three experiments.

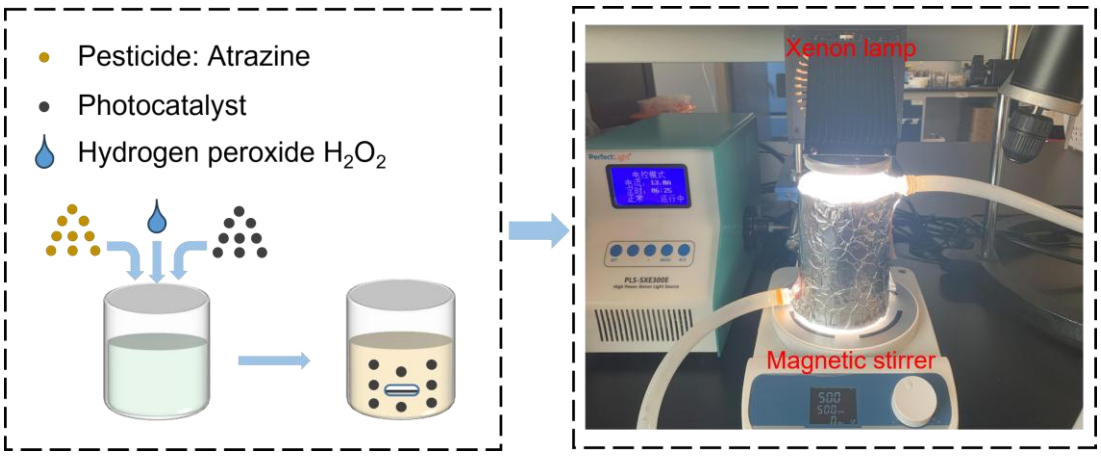

Figure 2.7 Photo-Fenton experimental process and experimental setup.

2.4.3 Reactive oxygen species determination: Scavenger tests and EPR measurements

Reactive oxygen species (ROS) contributing to the Fenton-like degradation activity were identified through scavenger testing and electron paramagnetic resonance spectroscopy (EPR) measurements. Tert-butyl alcohol (TBA), superoxide dismutase (SOD), and L-histidine were used as scavengers for hydroxyl radicals (·OH), superoxide radicals ($\cdot O_2^-$), and singlet oxygen ($^1O_2$), respectively. Prior to the catalytic experiment, the selected scavengers were added to the catalytic reaction system. Excess scavengers were added to ensure complete quenching of ROS generated during the reaction. The scavenger concentrations were 10 mM for TBA, 25 U/mL for SOD, and 10 mM for L-histidine, respectively. Catalytic degradation experiments were then conducted under the same reaction conditions as described in Section 2.4.2. Finally, the pollutant concentrations in the resulting sample solutions were measured. By comparing the effects of the addition of different scavengers on the degradation rate, the role of different ROS species in the reaction process can be determined.

To further identify the ROS generated during the catalyst reaction, EPR testing was conducted. The experiment used an A300-10/12 (Bruker Corporation, Germany) electron paramagnetic resonance spectrometer, employing 5,5-dimethyl-1-pyrroline-N-oxide (DMPO) and 2,2,6,6-tetramethylpiperidine (TEMP) as radical scavengers to detect hydroxyl radicals (·OH), superoxide radicals ($\cdot O_2^-$), and singlet oxygen ($^1O_2$), respectively. The specific testing steps are as follows:

Hydroxyl radical (·OH) detection: Disperse 1 mg/ml of the catalyst sample in deionised water as the solvent and sonicate for 15 minutes. Take 100 μl of the solution and mix it with 100 μl of freshly prepared 3% H_2O_2 solution (diluted with ultra-pure water from a 30% stock solution) and 200 μl of 100 mM DMPO aqueous solution

(prepared fresh and stored away from light) in a 1.5 ml centrifuge tube. Immediately vortex for 30 seconds to ensure thorough mixing. Use a 50 μl quartz capillary tube (inner diameter 0.9 mm) to aspirate the mixture, and seal both ends with sealing film. Conduct dark reactions (wrapped in aluminium foil) and light reactions (300 W xenon lamp + 420 nm filter, light intensity 100 mW/cm²) for 5 minutes each, with the reaction temperature controlled at 25 ± 1°C.

Superoxide radical (O_2^-) detection: Prepare a 1 mg/ml sample methanol solution (HPLC grade) and sonicate for 15 minutes. Take 100 μl of the solution and mix with 100 μl of 3% H_2O_2 methanol solution and 200 μl of 100 mM DMPO methanol solution (protected with argon gas to prevent oxidation). Subsequent processing steps are the same as for ·OH detection. Note that all operations are performed in an inert atmosphere glove box to avoid oxygen interference.

Singlet oxygen ($^1O_2$) detection: Prepare a 1 mg/ml aqueous solution of the sample and sonicate for 15 minutes. Take 100 μl of the solution and mix with 100 μl of 3% H_2O_2 solution and 200 μl of 100 mM TEMP solution (prepared with ethanol and stored in the dark). The mixture must be processed immediately, as the TEMP-$^1O_2$ adduct has a short half-life at room temperature.

Immediately after the reaction is complete, take 100 μl of the reaction solution and inject it into a quartz capillary tube for EPR testing. The test parameters are set as follows: for detecting ·OH, the central magnetic field is 3500 G and the sweep width is 100 G; for detecting $\cdot O_2^-$, the central magnetic field is 3440 G and the sweep width is 120 G. Free radical identification is performed based on characteristic peak shapes: the DMPO-·OH adduct exhibits a typical 1:2:2:1 quadruplet peak; DMPO-$\cdot O_2^-$ shows a sextet peak; and TEMP-$^1O_2$ produces a 1:1:1 triplet peak characteristic signal. All

tests must be completed within 5 minutes after the reaction, and dark reaction control samples must be measured simultaneously.

2.5 Experimental analysis methods

2.5.1 Liquid chromatography to test the concentration of pesticides in water

Imidacloprid (IMD) concentrations in filtered sample solutions were determined using high-performance liquid chromatography (HPLC, Agilent 1100). The chromatographic column was an Agilent ZORBAX Eclipse Plus C18 column (4.6 × 250 mm), with a UV detector at 270 nm. The mobile phase consisted of 50/50 (v/v) methanol and ultrapure water at a flow rate of 1 mL min-1. The column temperature was 25°C.

Atrazine (ATZ) in the sample solution was also determined using an Agilent 1100 using an Agilent ZORBAX SB C18 column (4.6 × 250 mm, 5 μm). The UV detector was set at 225 nm, the mobile phase was 70/30 (v/v) methanol and ultrapure water at a flow rate of 1 mL min-1, and the column temperature was 40°C.

The retention time and integrated area of all samples were recorded and compared with the calibration curve and retention time of standard samples to perform qualitative and quantitative analysis of the solutes. The degradation process follows a pseudo-first-order reaction and can be described by equation (2 - 1):

$$\text{Organic pollutant removal rate (\%)} = \frac{C_t}{C_0} \times 100\% \qquad (2-1)$$

The apparent rate constant can be calculated using formula (2 - 2):

$$\ln\left(\frac{C_0}{C_t}\right) = kt \qquad (2-2)$$

where k is the apparent rate constant, and C_0 and C_t represent the concentrations

of organic pollutants at the initial stage and after the specified irradiation time interval, respectively.

2.5.2 The content of H_2O_2 in the heterogeneous Fenton reaction system was tested by UV-vis spectrophotometry

The concentration changes of H_2O_2 during the Fenton reaction were determined using ultraviolet-visible spectrophotometry. This method utilizes the specific colorimetric reaction between Ti(IV) and H_2O_2, which exhibits high selectivity and sensitivity under strongly acidic conditions, enabling accurate monitoring of H_2O_2 concentration during the Fenton reaction. First, 640 mg of titanium sulfate-sulfuric acid hydrate ($TiOSO_2 \cdot xH_2O+H_2SO_4$) was dissolved in 40 mL of 16 M sulfuric acid solution, and the volume was adjusted to 750 mL with ultra-pure water to prepare the titanium reagent solution. This acidic titanium reagent reacts with H_2O_2 in the sample to form the yellow peroxytitanium complex $[Ti(O_2)OH(H_2O)_3]^+$. The concentration of H_2O_2 is quantitatively analyzed by measuring its characteristic absorbance at 409 nm. During the experiment, a series of H_2O_2 standard solutions ranging from 0 to 1.8 mM were prepared to create a standard curve, as shown in Figure 2.8. The sample to be tested was mixed with the titanium reagent in an appropriate ratio and reacted for 5–10 minutes. The absorbance at 409 nm was then measured under the same conditions, and the accurate concentration of H_2O_2 in the sample was calculated based on the standard curve.

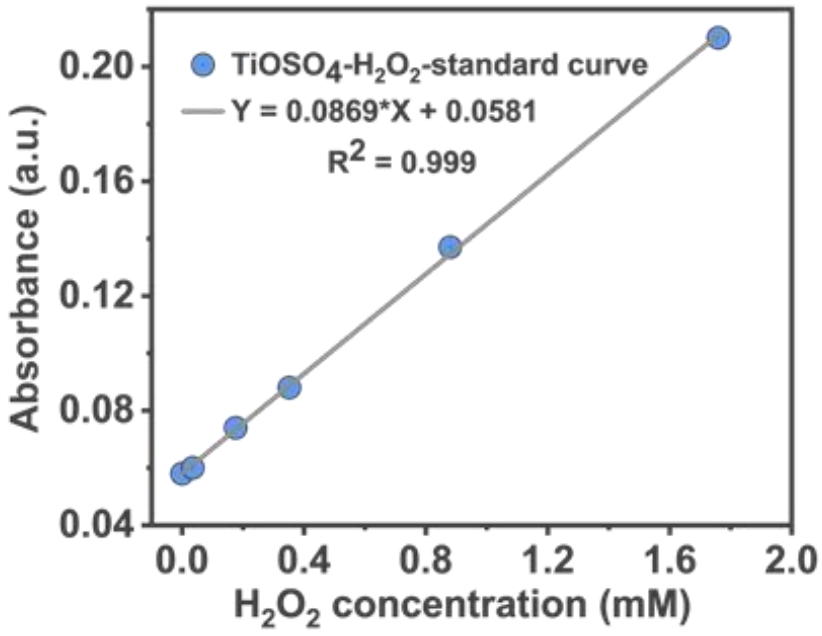

Figure 2.8 Standard curve for measuring hydrogen peroxide concentration using ultraviolet-visible spectrophotometry.

2.5.3 Identification of catalytic degradation products of pesticides by ultra-performance liquid chromatography-quadrupole time-of-flight mass spectrometry (UPLC-QTOF-MS)

The screening of transformation products from pollutant degradation was performed using an ACQUITY UPLC I-Class System (Waters) coupled to a TripleTOF 5600 mass spectrometer (AB SCIEX). Chromatographic separation was achieved on an ACQUITY UPLC BEH C18 column (100 × 2.1 mm, 1.7 μm) under isocratic elution with a mobile phase consisting of 20% ultrapure water and 80% acetonitrile, both containing 0.1% formic acid, at a flow rate of 0.3 mL/min. The injection volume was 5 μL, and the total run time was 20 min. Mass spectrometric analysis was conducted in both positive and negative ESI modes, with subsequent focus on positive mode due

to higher signal responses. High-resolution MS and MS/MS data were acquired in the range of m/z 90–500 (extendable to m/z 1700) at a scan rate of 2 spectra/sec, using optimized source conditions (ion spray voltage: ±5500 V, source temperature: 500°C, gas flow: 8 L/min). Data were processed using SCIEX OS and PeakView® software, where molecular features were extracted, and candidate TPs were identified based on accurate mass (⩽5 ppm error) and MS/MS fragmentation patterns.

Conclusion of Chapter 2

This section provides a detailed description of the synthesis methods for pure titanium-based MOFs (NH_2-MIL-125) and composite materials (NH_2-MIL-125/TiO_2), as well as the synthesis methods for composite materials with different ratios of TiO_2 and MOF precursors. Additionally, it describes the detailed synthesis methods for pure iron-based MOFs (MIL-88A), tannic acid-modified MIL-88A@TA, and MIL-88A@TA-X after calcination at different temperatures.

We also introduce various characterisation methods for the physical and chemical properties of the catalysts, such as morphological and phase structure characterisation (SEM, TEM, XRD), chemical structure characterisation (FTIR, XPS, TGA, ICP-OES, ESR), and optical property characterisation (UV-Vis DRS).

We also provide a detailed description of the experimental methods for the photodegradation of imidacloprid in water using NH_2-MIL-125 and NH_2-MIL-125/TiO_2 composite materials via photocatalytic reactions, as well as the experimental methods for the degradation of atrazine in water using MIL-88A, MIL-88A@TA, and MIL-88A@TA-X via heterogeneous photo-Fenton reactions.

The results of this chapter were published in:

Research articles:

1. **Zhou Zhentao**, Tetiana Dontsova. Modification methods to enhance the performance of TiO_2 in photocatalysis. *Water and Water Purification Technologies. Scientific and Technical News*, 2023, 36(2): 40-57. https://doi.org/10.20535/2218-930022023299542.
2. **Zhou Zhentao**, Anastasiia Sukhoivanenko, Tetiana Dontsova. Prospects of using MOF/TiO_2 nanocomposites for photocatalytic degradation of pesticides. *Functional Materials*, 2024, 31 (4): 630-637. https://doi.org/10.15407/fm31.04.630.

3. Wang, W., Shi, H., Shi, H., **Zhou, Z**., Mao, L., Zhang, L., ... & Liu, X. Application of modified biochar in integrated pollution management for pesticides and antibiotics in water: Recent advances and future prospects. Environmental Research, 2025, 285: 122499. https://doi.org/10.1016/j.envres.2025.122499.

Abstracts of conference presentations:

1. **Zhou Zhentao**, Dontsova T.A. (2023). Degradation performance and mechanism of MOF/TiO_2 nanocomposites for pesticide pollutants in aqueous phase. *Book of abstracts of Міжнародну конференцію з хімії, хімічної технології та екології, що присвячена 125-річчю КПІ ім. Ігоря Сікорського.* Kyiv, p. 263.

2. **Zhou Zhentao**, Dontsova T.A. (2023). Prospects for the use of TiO_2/MOF structures in photocatalysis. *Book of abstracts of the International research and practice conference «Nanotechnology and nanomaterials» (NANO-2023).* Lviv, p. 206.

CHAPTER 3. Characterization and Properties of NH_2-MIL-125/TiO_2 Composite Photocatalyst and its Removal Performance for the Insecticide Imidacloprid in Water

3.1 Sample synthesis

Titanium-based MOF (NH_2-MIL-125) and a series of NH_2-MIL-125/TiO_2 composites were synthesized according to the synthesis method in Section 2.1. The names and characteristics of the synthesized materials are shown in Table 3.1, (TiO_2/TPOT) represents the molar ratio of TiO_2 and TPOT added during sample synthesis. In the following text, unless otherwise specified, NH_2-MIL-125/TiO_2 refers to NH_2-MIL-125/TiO_2-100% with the best performance and cost.

Table 3.1 Names and characteristics of the synthesized materials

Sample name	Synthesis characteristics
NH_2-MIL-125	Precursors: NH_2-BDC, TPOT
NH_2-MIL-125/TiO_2-35%	Precursors: NH_2-BDC, TPOT, TiO_2 (TiO_2 / TPOT = 35%)
NH_2-MIL-125/TiO_2-100%	Precursors: NH_2-BDC, TPOT, TiO_2 (TiO_2 / TPOT = 100%)
NH_2-MIL-125/TiO_2-150%	Precursors: NH_2-BDC, TPOT, TiO_2 (TiO_2 / TPOT = 150%)
NH_2-MIL-125/TiO_2-200%	Precursors: NH_2-BDC, TPOT, TiO_2 (TiO_2 / TPOT = 200%)

3.2 XRD characterization results of samples

Figure 3.1 shows the X-ray diffraction (XRD) patterns of TiO_2 and NH_2-MIL-125/TiO_2 composite materials. The results show that the XRD pattern of TiO_2 is consistent with that of the typical commercial TiO_2 sample P25, confirming the presence of the main rutile phase [81].

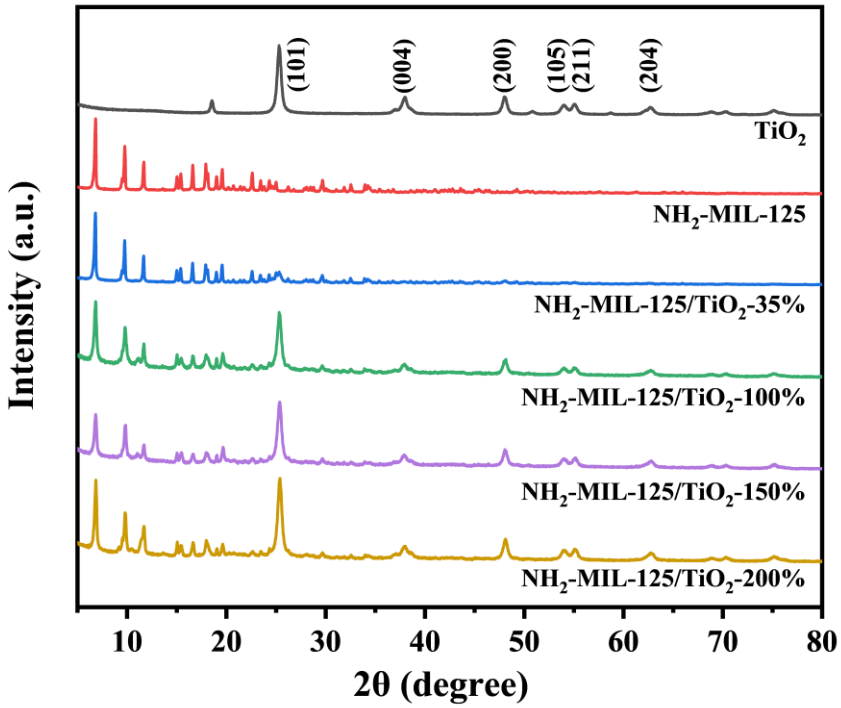

Figure 3.1 XRD patterns of the prepared materials.

The XRD pattern of NH_2-MIL-125 is consistent with the metal organic framework structure of this type reported in the literature [82], confirming the successful synthesis, which can be seen from the XRD characteristic peaks mainly attributed to this structure in the 2θ range of 5° to 25°. The XRD pattern of the NH_2-MIL-125/TiO_2 composite material shows clear characteristic peaks of TiO_2 (101), as well as characteristic peaks of NH_2-MIL-125 from 5° to 25°, confirming the formation of the composite material

and the stability of the TiO_2 structure therein. Figure 2 shows that as the TiO_2/TPOT ratio increases, the intensity of the TiO_2 main peak (101) also increases, while the phase structure of NH_2-MIL-125 is not affected by the TiO_2 doping amount.

3.3 Morphological characterization of samples

SEM images confirmed the formation of MOF structure and NH_2-MIL-125/TiO_2 composite material. As shown in Figure 3.2a, the TiO_2 sample showed a characteristic structure composed of small particles with a size not exceeding 50 nm.

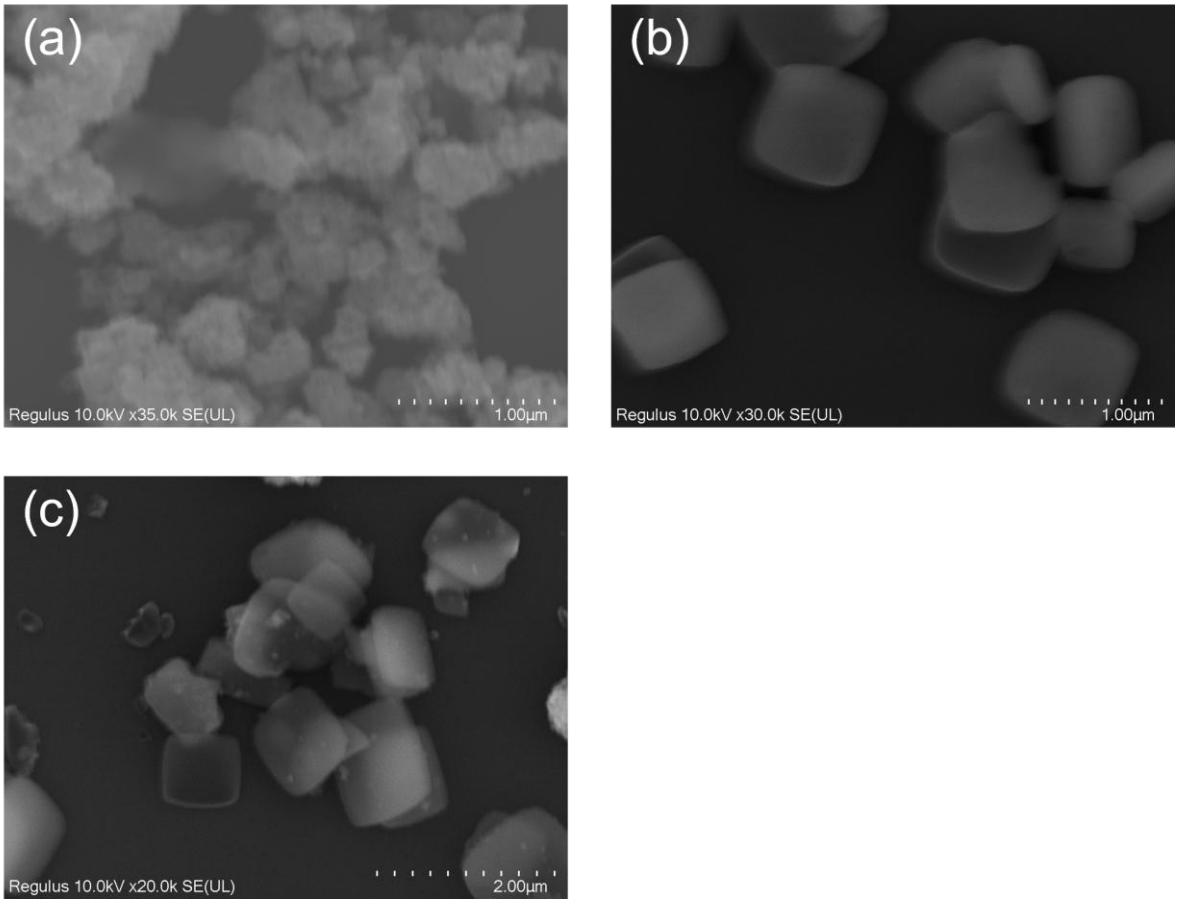

Figure 3.2 SEM images of (a) TiO_2, (b) NH_2-MIL-125, (c) NH_2-MIL-125/TiO_2-100%.

Due to the strong interaction between the particles, these particles formed agglomerates and aggregates [81]. This agglomeration effect is usually not conducive to the contact between TiO_2 nanoparticles and pollutants in the photocatalytic reaction system, thereby affecting the photocatalytic reaction activity. On the other hand, the NH_2-MIL-125 sample has a typical tetragonal crystal structure of this type of MOF, with a particle size mainly not exceeding 500 nm and good particle dispersion (Figure 3.2b). In Figure 3.2c, the NH_2-MIL-125/TiO_2 composite material maintains the main morphological structure of NH_2-MIL-125. A careful observation shows that the TiO_2 nanoparticles are distributed on the surface of the material and are well dispersed. This shows that the NH_2-MIL-125/TiO_2 composite material not only constitutes a heterogeneous structure but also facilitates the dispersion of TiO_2 nanoparticles.

3.4 Light absorption ability and band structure of samples

The light absorption properties and band gap of the catalyst are crucial for photocatalytic applications. Figure 4a shows the reflectance spectra of TiO_2, NH_2-MIL-125, and NH_2-MIL-125/TiO_2 samples.

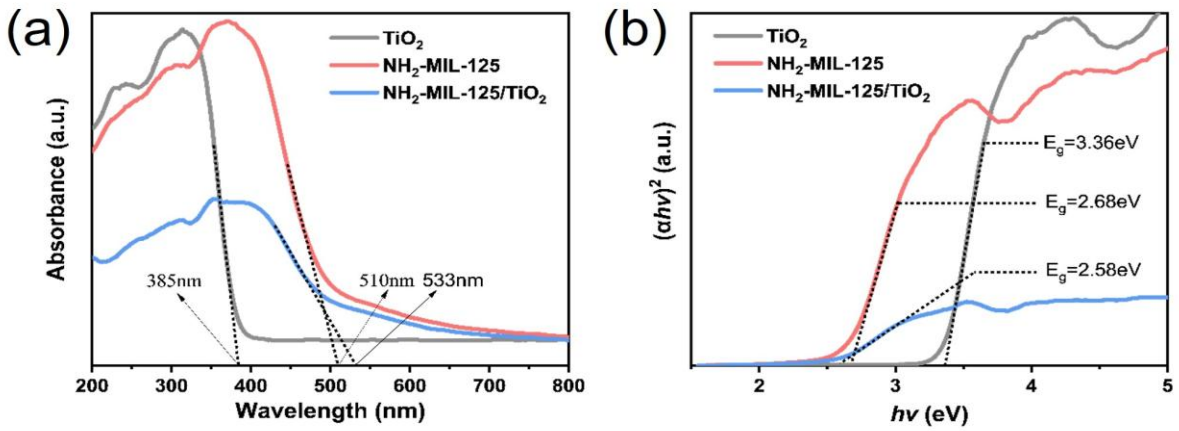

Figure 3.3 UV-visible diffuse reflectance spectroscopy.

Figure 4b also shows the Tauc plot conversion curves of the corresponding spectra. As can be seen from Figure 4a, the diffuse reflectance-absorption spectrum of titanium dioxide has typical characteristics, with the absorption starting at 385 nm, which is almost consistent with the theoretical data [83]. From the perspective of potential application prospects of photocatalytic processes under visible light, the spectrum of the NH_2-MIL-125 sample is interesting because the absorption starting wavelength is 510 nm (which is consistent with the data of other authors [82]) and it has the strongest absorption among all samples. The NH_2-MIL-125/TiO_2 composite material is characterized by a longer absorption wavelength, indicating that the composite material may have photocatalytic activity under visible light, which also indirectly indicates that the material may have formed a heterojunction structure that is conducive to light absorption. However, the absorption intensity of the composite material is low, which may indicate that it produces fewer electron-hole pairs. As shown in Figure 4b, the band gap of TiO_2 is about 3.36 eV, the band gap of NH_2-MIL-125 is about 2.68 eV, and the band gap of NH_2-MIL-125/TiO_2 composite is about 2.58 eV.

3.5 FTIR spectrum characterization results of samples

Figure 3.4 shows the infrared spectra of TiO_2, NH_2-MIL-125, and NH_2-MIL-125/TiO_2 samples.

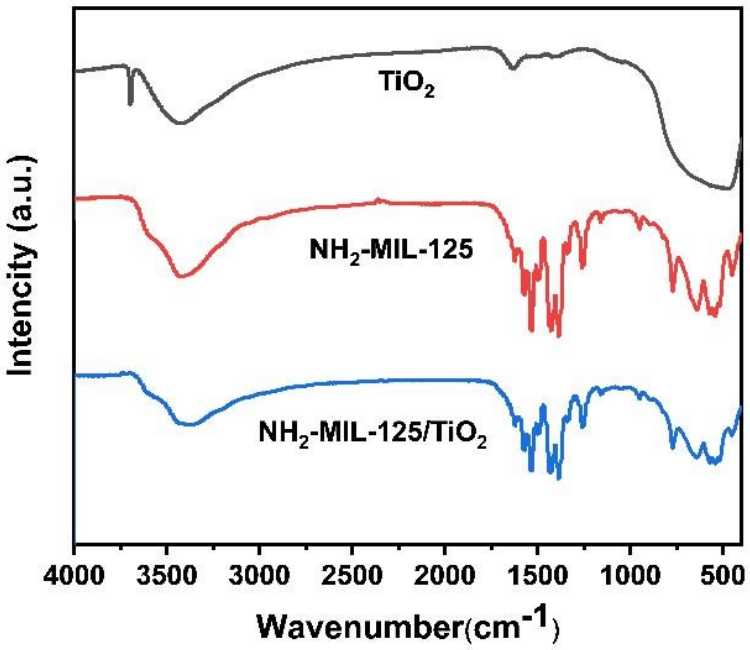

Figure 3.4 FTIR spectra of the prepared materials.

The infrared spectrum of the TiO_2 P25 sample is a typical spectrum of titanium dioxide. The peak width in the range of 480-600 cm^{-1} indicates the presence of anatase and rutile phases, which has been confirmed by the literature. The characteristic signals of NH_2-MIL-125 were observed at 1530 cm^{-1} (N-H stretching vibration), 1420 cm^{-1} (CN vibration), 1570 cm^{-1} and 1500 cm^{-1} (asymmetric -COO vibration), and 1390 cm^{-1} (symmetric -COO vibration) [84]. From the spectrum of the NH_2-MIL-125 sample, it can be seen that the spectral band of the R-COOH functional group of the starting ligand is significantly shifted due to the complexation with Ti(IV). At the same time, we observed the disappearance of the carbonyl (C=O) band (at 1690 cm^{-1}) and the

formation of two new bands at 1600-1500 cm^{-1} and 1450-1350 cm^{-1}, which correspond to the asymmetric and symmetric stretching vibrations of the carboxylate group (COO-), respectively [84]. Therefore, the interaction between Ti(IV) and the -COOH functional group of the ligand induces the resonance structure of the carboxylate group (-COO). This indicates the complexation and formation of titanium MOF. The infrared spectrum of the NH_2-MIL-125/TiO_2 composite material is consistent with the infrared spectrum of the NH_2-MIL-125 sample. This may indicate that the sample contains a small amount of titanium dioxide.

3.6 Thermogravimetric analysis results of samples

Thermogravimetric analysis (TG) can be used to determine the thermal stability of materials and the relative quantitative content of components with different thermal stability in composite materials. Therefore, we separately tested the TG data of TiO_2, NH_2-MIL-125, and NH_2-MIL-125/TiO_2 composite materials with different precursor ratios to infer the actual content of TiO_2 in the composite materials.

As shown in Figure 3.5, the mass loss observed in NH_2-MIL-125 and all NH_2-MIL-125/TiO_2 composite materials between 0–100°C is generally attributed to the desorption of adsorbed water molecules, while the significant mass loss between 350–500°C is attributed to the decomposition of organic ligands in the MOF structure at high temperatures [85].

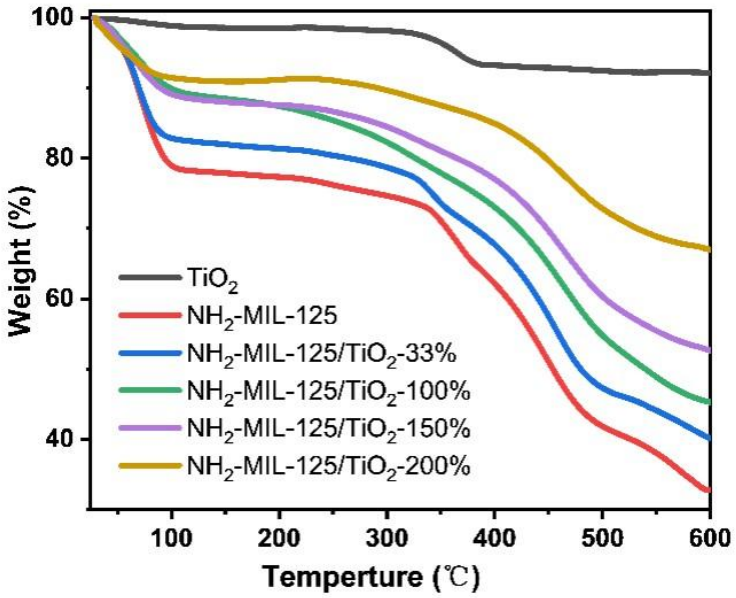

Figure 3.5 TG analysis curves of the prepared materials.

Comparing the TG of pure TiO_2 reveals that TiO_2 only experiences a slight mass loss between 350–400°C, which may be due to the removal of a small amount of lattice oxygen from the TiO_2 structure at high temperatures [86]. Therefore, we can infer the relative content of TiO_2 in the composite material based on the residual mass. When the molar ratio of TiO_2 P25 to TPOT precursor is 0.35:1, the TiO_2 content in the NH_2-MIL-125/TiO_2 composite sample does not exceed 30% wt. Additionally, we analyzed composite samples with higher TiO_2 content, where the molar ratio of P25 to TPOT precursor was 1:1, 1.5:1, and 2:1. It can be seen that the TiO_2 content in the NH_2-MIL-125/TiO_2 samples was ~40%, 50%, and 63% wt., respectively.

3.7 Catalytic activity of NH_2-MIL-125/TiO_2 composite photocatalyst for imidacloprid

We evaluated the kinetics of imidacloprid degradation in water using the various synthesized catalysts. The results, shown in Figures 3.6, show a slight decrease in imidacloprid concentration observed for all materials for up to 60 minutes before xenon lamp irradiation, which is associated with the adsorption process.

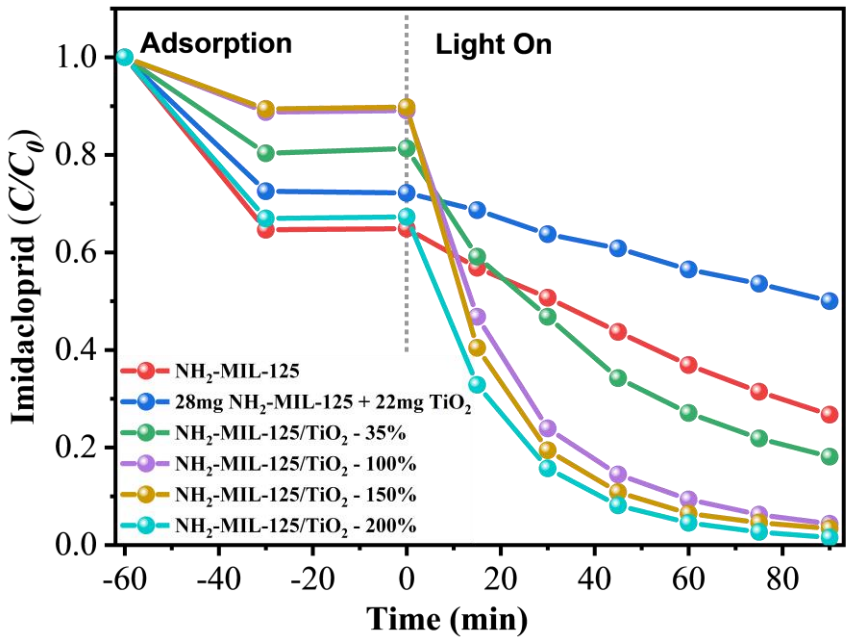

Figure 3.6 Degradation kinetic curve of imidacloprid in water by the prepared material (catalyst 50 mg, imidacloprid aqueous solution 50 mL (10 mg/L), dark reaction 60 min, light reaction 90 min).

The NH_2-MIL-125 sample exhibited a higher adsorption capacity, likely due to the unique porous structure of NH_2-MIL-125 as a MOF. The adsorption capacities of NH_2-MIL-125/TiO_2-35%, NH_2-MIL-125/TiO_2-100%, and NH_2-MIL-125/TiO_2-150% samples were relatively low, likely due to the presence of loaded TiO_2 nanoparticles, which blocked the adsorption active sites on the NH_2-MIL-125 surface. Interestingly,

the adsorption capacity of NH_2-MIL-125/TiO_2-200% sample recovered, likely due to the increased surface area of the large number of TiO_2 nanoparticles deposited on the surface. After xenon lamp irradiation, the rate of decrease in imidacloprid concentration in all the photocatalytic systems we tested was significantly faster than that observed during the dark reaction.

This confirms the activation of the photocatalytic reaction, leading to more vigorous degradation of the studied pesticides. Comparative degradation results show that NH_2-MIL-125/TiO_2-100%, NH_2-MIL-125/TiO_2-150%, and NH_2-MIL-125/TiO_2-200% exhibit the most significant photocatalytic activity, removing nearly 100% of imidacloprid after 90 minutes of photoreaction. While the catalytic performance of NH_2-MIL-125/TiO_2-35% was inferior to that of pure NH_2-MIL-125, combined with previous characterization and analysis, this suggests that composite materials composed of NH_2-MIL-125 and TiO_2 can improve light absorption and band structure, thereby enhancing photocatalytic activity.

To further demonstrate the advantages of the composite material, we conducted photocatalytic experiments using a mixture of 28 mg NH_2-MIL-125 and 22 mg TiO_2 (a 1:1 molar ratio of TiO_2 to NH_2-MIL-125). The results showed that the NH_2-MIL-125 and TiO_2 mixture only removed approximately 50% of imidacloprid within 90 minutes, a performance significantly lower than that achieved by a 100% NH_2-MIL-125/TiO_2 composite with the same molar ratio. This demonstrates that the advantages of the NH_2-MIL-125/TiO_2 composite are not simply the result of additive catalytic activity but rather arise from a synergistic effect between the NH_2-MIL-125 and TiO_2 composites.

Conclusion of Chapter 3

1. Pure NH_2-MIL-125 and NH_2-MIL-125/TiO_2 composites with different TiO_2/TPOT ratios were successfully synthesised. XRD characterisation results confirmed that TiO_2 exhibits a typical anatase structure, while the XRD structure of NH_2-MIL-125 aligns with previously reported literature. The NH_2-MIL-125/TiO_2 composite material simultaneously exhibits XRD characteristic peaks of both TiO_2 and NH_2-MIL-125, indicating the successful synthesis of the composite material.

2. SEM images reveal NH_2-MIL-125 crystals with a regular tetragonal morphology, and the images of the NH_2-MIL-125/TiO_2 composite material also show TiO_2 nanoparticles embedded on the surface of NH_2-MIL-125, further confirming the successful synthesis of the composite material. The FTIR spectra of NH_2-MIL-125 and NH_2-MIL-125/TiO_2 are nearly identical, further confirming that the incorporation of TiO_2 does not disrupt the basic structure of the MOF.

3. The bandgap of TiO_2 calculated from UV-vis DRS results is approximately 3.36 eV, that of NH_2-MIL-125 is approximately 2.68 eV, and that of the NH_2-MIL-125/TiO_2 composite material is approximately 2.58 eV. The bandgap of the composite material is smaller than that of the two individual components, indicating that the composition of the composite material can optimise the band structure, which is beneficial for the material to utilise light energy more effectively.

4. Activity tests show that the catalytic activity of the NH_2-MIL-125/TiO_2 composite material is significantly stronger than that of pure NH_2-MIL-125. NH_2-MIL-125/TiO_2-100%, NH_2-MIL-125/TiO_2-100%, NH_2-MIL-125/TiO_2-150%, and NH_2-MIL-125/TiO_2-200% exhibit nearly identical excellent catalytic performance, all capable of degrading nearly 100% of imidacloprid within 90 minutes, indicating that the

constructing MOF-based composite materials is an effective solution to improve photocatalytic performance.

The results of this chapter were published in:

Research articles:

1. **Zhou Zhentao**, Anastasiia Sukhoivanenko, Tetiana Dontsova. Prospects of using MOF/TiO_2 nanocomposites for photocatalytic degradation of pesticides. *Functional Materials*, 2024, 31 (4): 630-637. https://doi.org/10.15407/fm31.04.630.

Abstracts of conference presentations:

3. Zhou Zhentao, Dontsova T.A. (2023). Degradation performance and mechanism of MOF/TiO_2 nanocomposites for pesticide pollutants in aqueous phase. *Book of abstracts of Міжнародну конференцію з хімії, хімічної технології та екології, що присвячена 125-річчю КПІ ім. Ігоря Сікорського.* Kyiv, p. 263.
4. Zhou Zhentao, Dontsova T.A. (2023). Prospects for the use of TiO_2/MOF structures in photocatalysis. *Book of abstracts of the International research and practice conference «Nanotechnology and nanomaterials» (NANO-2023).* Lviv, p. 206.

CHAPTER 4 Characterization, Properties of the Porous Iron-Based MOF Material Modified by Tannic Acid (M88A@TA-X), and its Performance for the Removal of Atrazine from Water via a Photo-Fenton Catalytic Process

4.1 Sample synthesis

Following the synthetic procedures described in Section 2.2, we synthesized pure iron-based MOFs (MIL-88A, denoted as M88A) and tannic acid-modified MOFs (M88A@TA). MIL-88A@TA was then further calcined to produce the final defective MOFs (M88A@TA-X), where X represents the calcination temperature. Furthermore, to demonstrate the effect of tannic acid modification, we calcined pure, unmodified MIL-88A at different temperatures to produce M88A-X. The names and synthetic characteristics of the resulting samples are shown in Table 4.1.

Table 4.1 Names and characteristics of the synthesized materials

Sample name	Synthesis characteristics
M88A	Hydrothermal synthesis, precursors: Fumaric acid, $FeCl_3 \cdot 6H_2O$. Unmodified. Uncalcined
M88A-2	Hydrothermal synthesis, precursors: Fumaric acid, $FeCl_3 \cdot 6H_2O$. Not modified with TA. Calcination temperature: 200 ℃
M88A-3	Hydrothermal synthesis, precursors: Fumaric acid, $FeCl_3 \cdot 6H_2O$. Not modified with TA. Calcination temperature: 300 ℃
M88A-4	Hydrothermal synthesis, precursors: Fumaric acid, $FeCl_3 \cdot 6H_2O$. Not modified with TA. Calcination temperature: 400 ℃
M88A@TA	Hydrothermal synthesis, precursors: Fumaric acid, $FeCl_3 \cdot 6H_2O$. TA modified. Uncalcined
M88A@TA-2	Hydrothermal synthesis, precursors: Fumaric acid, $FeCl_3 \cdot 6H_2O$. TA modified. Calcination temperature: 200 ℃
M88A@TA-3	Hydrothermal synthesis, precursors: Fumaric acid, $FeCl_3 \cdot 6H_2O$. TA modified. Calcination temperature: 300 ℃
M88A@TA-4	Hydrothermal synthesis, precursors: Fumaric acid, $FeCl_3 \cdot 6H_2O$. TA modified. Calcination temperature: 400 ℃

4.2 Characterization of sample morphology and phase structure

We characterized the physical structure of the prepared materials by X-ray diffraction (XRD). As shown in Figure 4.1, the original M88A showed obvious characteristic peaks at 10.5° and 12.0°, corresponding to the 100 and 101 crystal planes, respectively, which is consistent with the results reported in previous studies [80], [87].

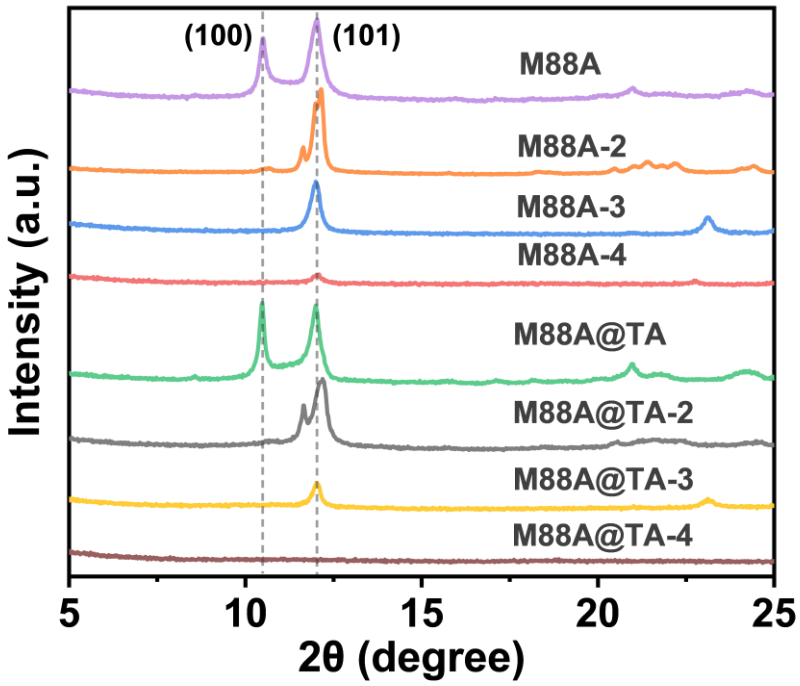

Figure 4.1 XRD patterns of the materials synthesized under different preparation conditions.

The XRD characteristic peaks of M88A@TA modified with tannic acid are almost identical to those of M88A, indicating that the modification with tannic acid does not change the basic crystal structure of M88A. Interestingly, the (100) characteristic peak of M88A@TA-2 and other calcined materials disappeared. This is due to the unique (breathing) characteristics of M88A, which shrinks its crystal plane during high-

temperature calcination, resulting in the disappearance of certain characteristic peaks [88]. A closer look reveals that the 101 characteristic peaks of M88A-2 and M88A@TA-2 are deformed compared to M88A. This phenomenon generally indicates that defects in the lattice structure of the MOF material have occurred, resulting in reduced crystallinity [89]. A detailed comparison reveals that the 101 peak of M88A@TA-2 is more significantly deformed and wider than that of M88A-2, suggesting that M88A@TA-2 may contain more defects than M88A-2. Furthermore, the XRD signal intensities of M88A@TA-3 and M88A-3 become very weak, while those of M88A@TA-4 and M88A-4 almost disappear. This indicates that after calcination at temperatures exceeding 300°C, these materials begin to transform into an amorphous structure, indicating that the framework structure of MOFs begins to collapse at temperatures above 300°C.

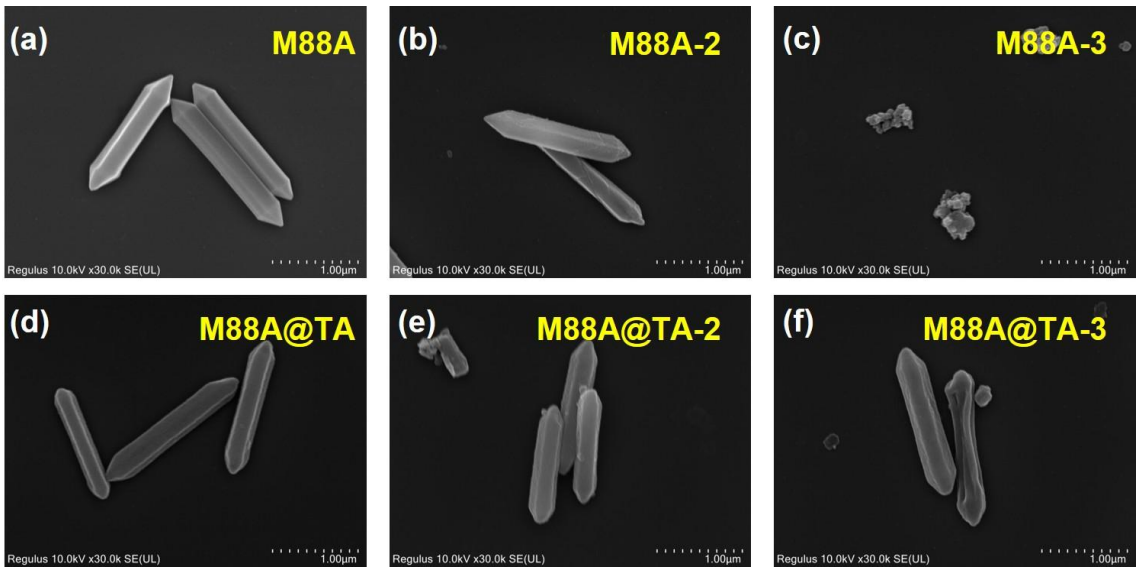

Figure 4.2 SEM images of the prepared materials.

The basic morphology of the materials was characterized using field-emission scanning electron microscopy (SEM). As shown in Figure 4.2a, the original M88A

exhibits a regular bipyramidal hexagonal prism with a smooth surface, approximately 1.5 μm in length, and 300 nm in width. After TA modification, M88A@TA retains a morphology similar to MIL@88A, but with a slightly roughened surface (Figure 4.2d). Further SEM images of the calcined materials reveal a roughened surface for M88A-2 (Figure 4.2b), while the surface of M88A@TA-2 exhibits an even rougher, spongy appearance (Figure 4.2e). Materials M88A-3 and M88A@TA-3, synthesized at higher calcination temperatures, both exhibit structural collapse, consistent with the XRD results. Therefore, we can infer that 200°C is a suitable temperature for constructing MOF defect structures.

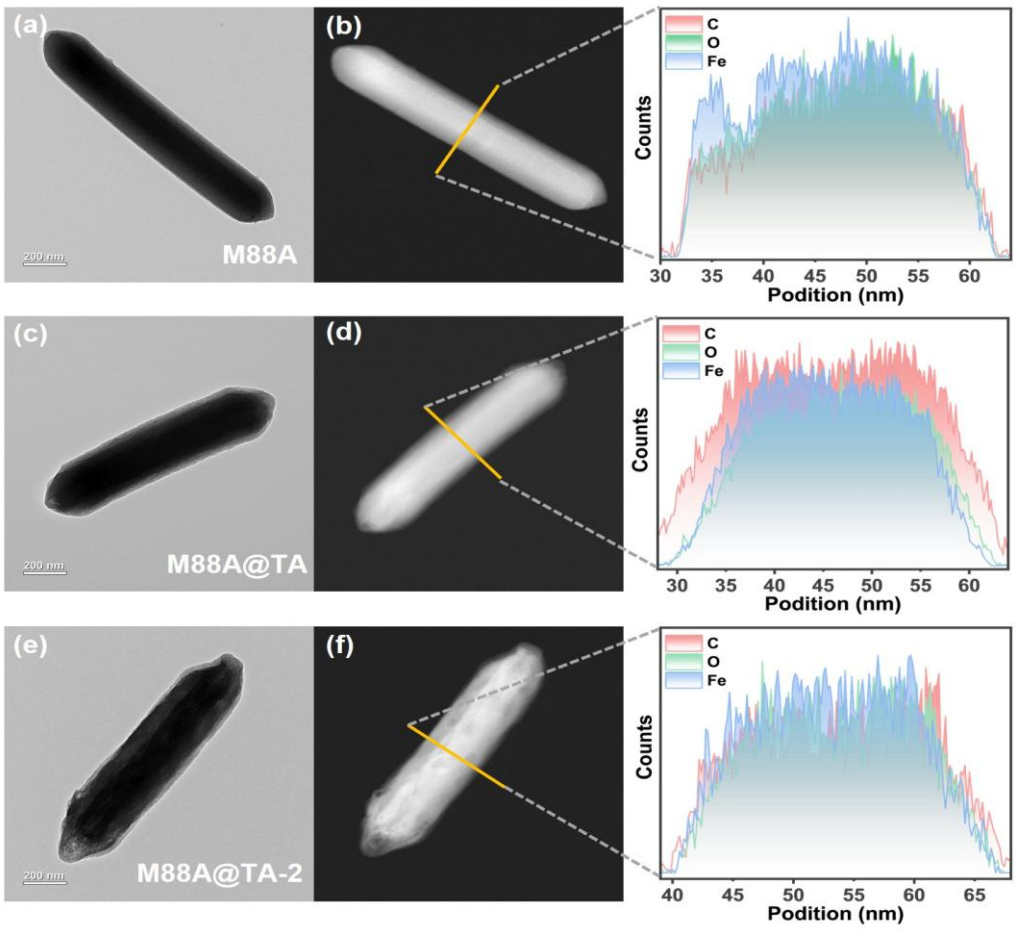

Figure 4.3 TEM and HAADF-STEM images of the prepared materials (the inset is the EDX line scan result under HAADF-STEAM mode).

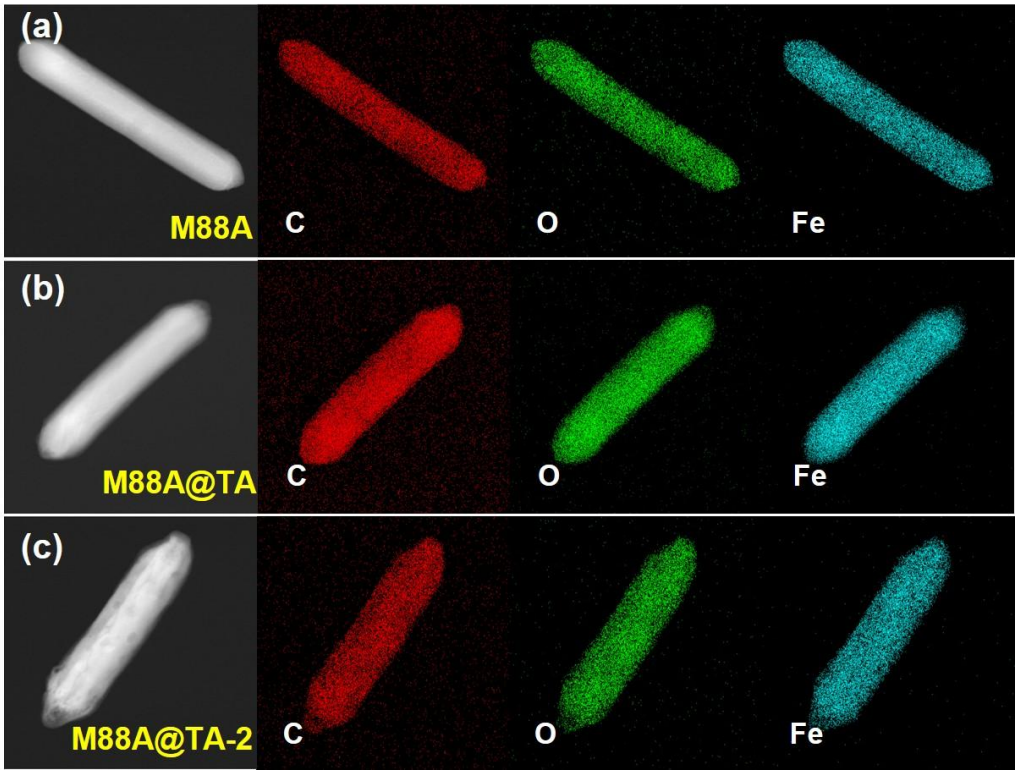

Figure 4.4 EDX element mapping images of C, O, and Fe elements of the prepared material under HAADF-STEM mode.

The internal structure and element distribution characteristics of the prepared materials were further observed using characterization methods such as high-resolution transmission electron microscopy (TEM), high-angle annular dark field scanning transmission electron microscopy (HAADF-STEM), energy dispersive X-ray (EDX) line scanning spectroscopy and EDX element mapping. The TEM and HAADF-STEM images of M88A showed that its morphology was regular and the density was uniform (Figure 4.3a, b). EDX line scanning and EDX element mapping also showed that it was composed of C, O, and Fe elements and the elements were evenly distributed (Figure 4.3b inset, 4.4a). Observing the TEM image of M88A@TA, it was found that a shell with a lower density was generated on its surface (Figure 4.3c). EDX line scanning and

EDX element mapping images proved that its surface was a C shell with a thickness of about 5 nm (Figure 4.3d inset, 4.4b), which can be attributed to the carbon-rich shell formed by TA chelating with the metal sites of M88A to form a complex and wrapping it on the surface [90]. Figures 4.3e and 4.3f show TEM and HAADF-STEM images of M88A@TA. A loose, porous shell approximately 50 nm thick appears on the surface of MIL-88A@TA. In addition, the EDX line scan and EDX mapping of M88A@TA-2 show that its internal elements are evenly distributed and there is no carbon shell structure similar to M88A@TA (Figure 4.3f inset and 4.4c). This suggests that calcination at 200°C can remove some of the TA chelated to the Fe sites and the unstable ligands while maintaining structural stability, thereby forming a rich defect structure.

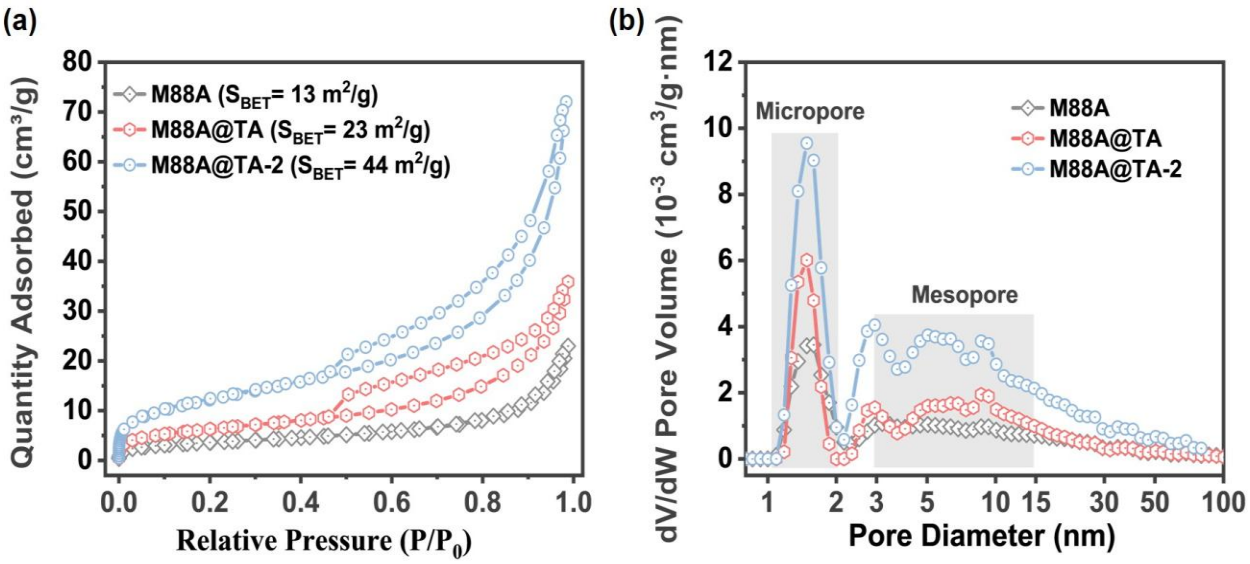

Figure 4.5 N_2 adsorption-desorption isotherm (a) and pore size distribution curve (b) of the prepared material.

To confirm the pore structure and adsorption properties of the material, N_2 adsorption-desorption isotherms were tested for the prepared material. Based on the

results, the Brunauer-Emmett-Teller (BET) specific surface area of the prepared material was calculated (Figure 4.5a), and the pore size distribution curve was calculated using a density functional theory (DFT) model (Figure 4.5b). The N_2 adsorption-desorption isotherm of M88A exhibits the typical microporous characteristics observed in other studies [91], [92], with a specific surface area of 13 m^2/g, consistent with previously reported results [80]. The pore size distribution curve indicates that the pore sizes of M88A are primarily distributed around 1.5 nm. After TA modification, the specific surface area of M88A@TA increased to 23 m^2/g. Additionally, the N_2 adsorption-desorption curve of M88A@TA exhibited an H4-type hysteresis loop [93]. Furthermore, the pore size distribution curve of M88A@TA exhibits characteristic peaks in the 3–15 nm range, indicating the presence of mesopores in the M88A@TA framework structure. This may be attributed to structural defects caused by TA competitively replacing some fumaric acid ligands [92]. The N_2 adsorption-desorption curve of M88A@TA-2 has the same shape as that of M88A@TA, but its specific surface area is significantly increased, reaching 44 m^2/g. Based on previous research analyses, the low-pressure region ($P/P_0 = 0–0.2$) in the N_2 adsorption-desorption curve of M88A@TA-2 corresponds to microporous filling, while the high-pressure region ($P/P_0 = 0.4–1.0$) corresponds to mesopores formed by the thermal calcination-induced instability and breakage of ligand bonds [94]. Additionally, the intensity of the microporous and mesoporous characteristic peaks in the pore size distribution curve is significantly higher than that of M88A@TA, indicating that M88A@TA-2 contains a richer defect structure.

4.3 Chemical composition and structural characterization of samples

The chemical bonds and functional group structures of the materials were confirmed by Fourier transform infrared spectroscopy (FTIR) (Figure 4.6).

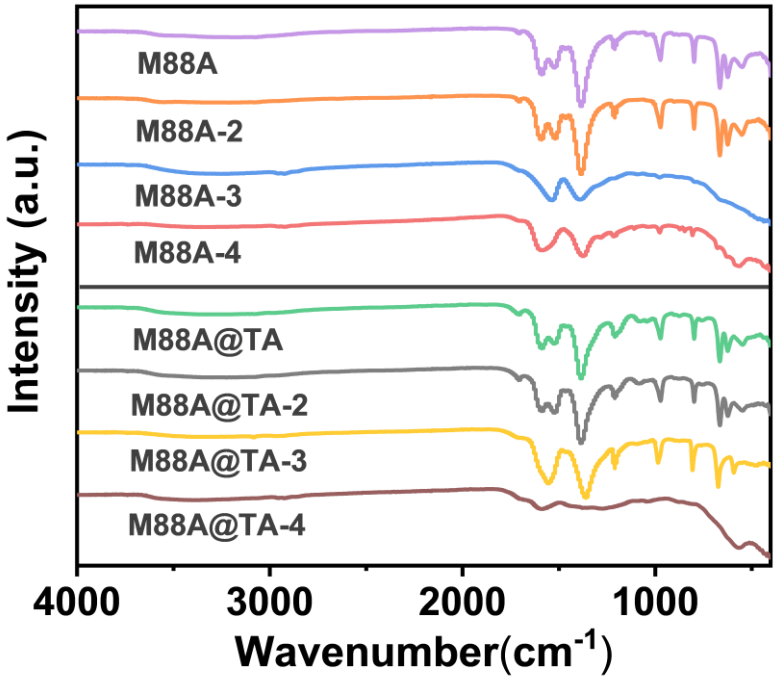

Figure 4.6 FTIR spectra of the prepared materials.

The results showed that the spectra of M88A@TA and M88A@TA-2 contained typical characteristic peaks attributed to TA, including 1710 cm^{-1} (carbonyl CO vibration) and 1202 cm^{-1} (aromatic CH bending vibration), as well as 1070 cm^{-1} (ester group), indicating that TA has been bound to the MIL-88A skeleton structure [90][95]. The characteristic peak intensity of 1510 cm^{-1} (carboxyl stretching vibration) in M88A@TA-2 was higher, which may be attributed to the exposure of carboxyl groups due to defects, further demonstrating the richness of defects in M88A@TA-2 [96], [97]. In addition, the characteristic peaks of the material M88A-3 calcined at 300°C almost

disappeared, indicating that the basic structure of MOF began to be destroyed. In contrast, M88A@TA-3 can retain a certain degree of characteristic peak signals, which indicates that TA modification can improve the thermal stability of M88A to a certain extent. For M88A-4 and M88A@TA-4 modified by calcination at higher temperatures, the FTIR characteristic peaks completely disappeared, indicating that the MOF structure completely collapsed, which is consistent with the XRD results.

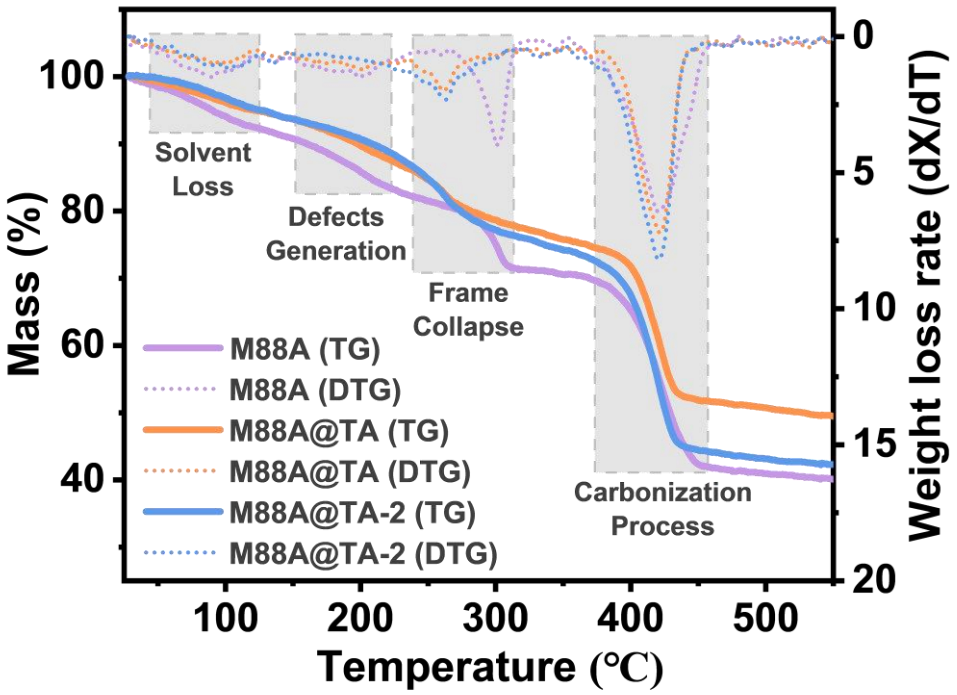

Figure 4.7 TG (left vertical, solid) and DTG (right vertical, dashed) curves of the prepared materials.

Table 4.2 Determination of Fe content in prepared materials by ICP-OES

Catalyst	**Fe (wt.%)**
M88A	23.8
M88A@TA	19.4
M88A@TA-2	21.4

To accurately assess the extent of defects in the material, thermogravimetric (TG) analysis was performed and differential thermogravimetric curves (DTG) were plotted. All samples exhibited four weight loss stages (Figure 4.7): in the first stage, weight loss below 120°C was primarily attributed to the removal of free solvent molecules from the MOF pores; in the second stage, mass loss in the 150–220°C temperature range was attributed to the removal of partially bridged organic ligands and terminal inorganic ligands [98], [99]. The DTG curve for M88A@TA-2 did not show a distinct peak in the second stage, indicating that it approached defect saturation. In the third stage, mass loss in the 240–320°C range can be attributed to the collapse of the MOF coordination structure. The lower mass loss of M88A@TA-2 and M88A@TA in this stage reflects their originally higher defect concentrations [100]. In the fourth stage, the significant mass loss in the 360–470 °C range can be attributed to the high-temperature carbonisation of organic ligands. The increase in residual mass for M88A@TA is due to tannic acid chelation leading to increased carbon content, while

the decrease in residual mass for M88A@TA-2 is attributed to the loss of the surface tannic acid shell layer during calcination in the synthesis process. This trend also aligns with the relative Fe elemental content in the inductively coupled plasma optical emission spectrometer (ICP-OES) results, which first decreases and then increases (M88A: 23.8%, M88A@TA: 19.4%, and M88A@TA-2: 21.4%) (Table 4.2).

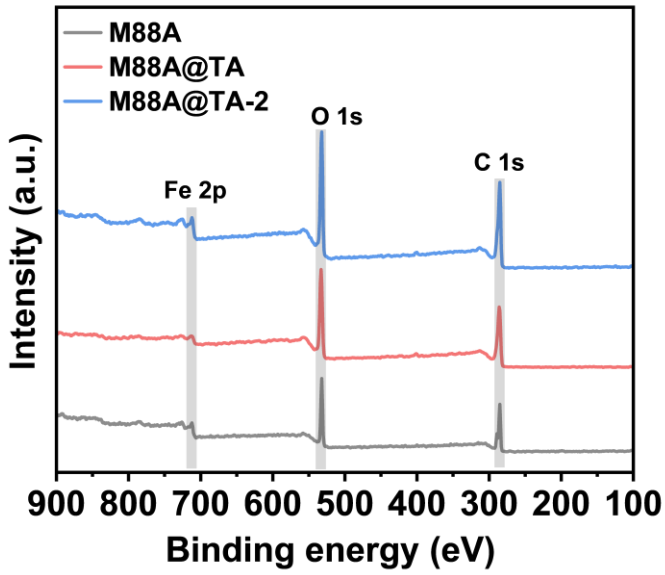

Figure 4.8 XPS total spectrum of the prepared materials.

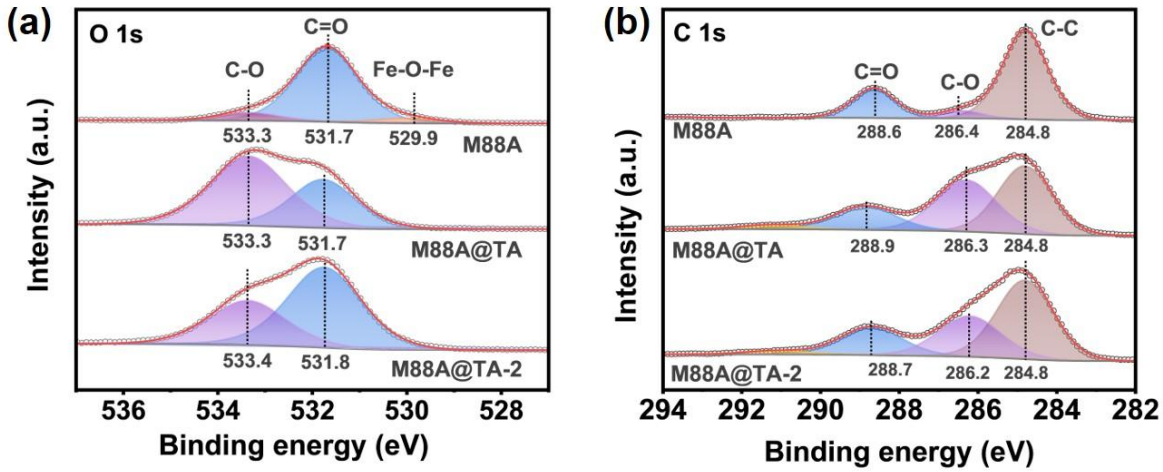

Figure 4.9 O 1s XPS spectra (a) and C 1s XPS spectra (b) of M88A, M88A@TA and M88A@TA-2.

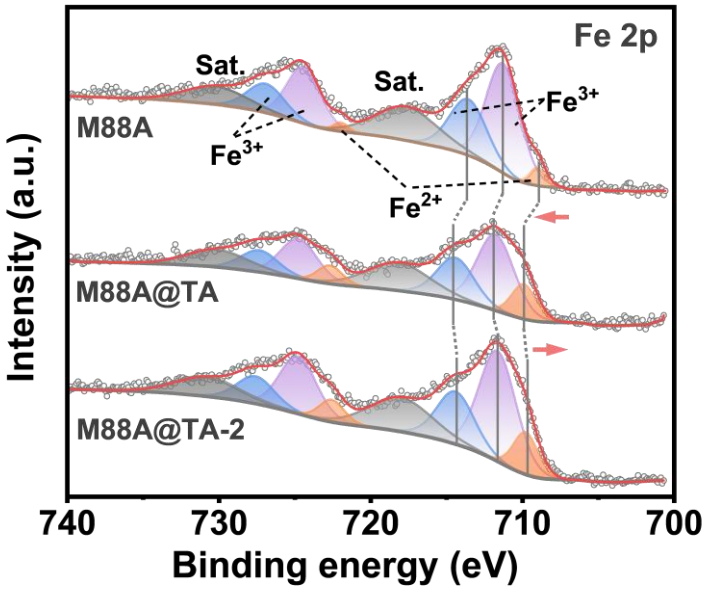

Figure 4.10 High-resolution Fe 2p XPS spectra of the prepared materials.

In order to analyze the elemental composition and chemical state of the materials, the samples were characterized by X-ray photoelectron spectroscopy (XPS). The results of the XPS total spectrum showed that all materials were mainly composed of three elements, namely C, O and Fe (Figure 4.8). For the deconvolution results of the O 1s fine spectrum, the peak intensity attributed to C-O (533.3 eV) in M88A, M88A@TA and M88A@TA-2 showed a clear trend of first increasing and then decreasing (Figure 4.9a) [90][96]. The C-O peak (286.4 eV) in the C 1s fine spectrum also showed the same trend (Figure 4.9b), which reflects the chelation of TA with the Fe site on MIL-88A and the process of TA and organic ligand shedding after heat treatment [101]. The deconvolution results of the Fe 2p fine spectrum are shown in Figure 4.10. The characteristic peak positions of Fe^{2+} and Fe^{3+} in M88A@TA shifted towards the high binding energy direction, which is due to the chelation of TA [90]. At the same time, the binding energy of the Fe 2p peak in M88A@TA-2 decreases again,

which can be attributed to the increase in the electron cloud density of the Fe site due to ligand shedding. In addition, the increase in the peak area attributed to Fe^{2+} in M88A@TA-2 is generally attributed to the unsaturated coordination of the Fe-O cluster, which generates more Fe^{2+} sites [98].

4.4 Optical characterization of samples

Generally, the band structure of a material is not only closely related to its light absorption capacity, but also significantly affects the redox performance of the material [49]. Therefore, we used UV-Vis DRS, Tauc-plot, and XPS valence band potential spectroscopy to measure the band structure of the prepared materials. The UV-Vis DRS results showed that the light absorption edges of M88A, M88A@TA, and M88A@TA-2 were 485 nm, 513 nm, and 582 nm, respectively (Figure 4.11 a).

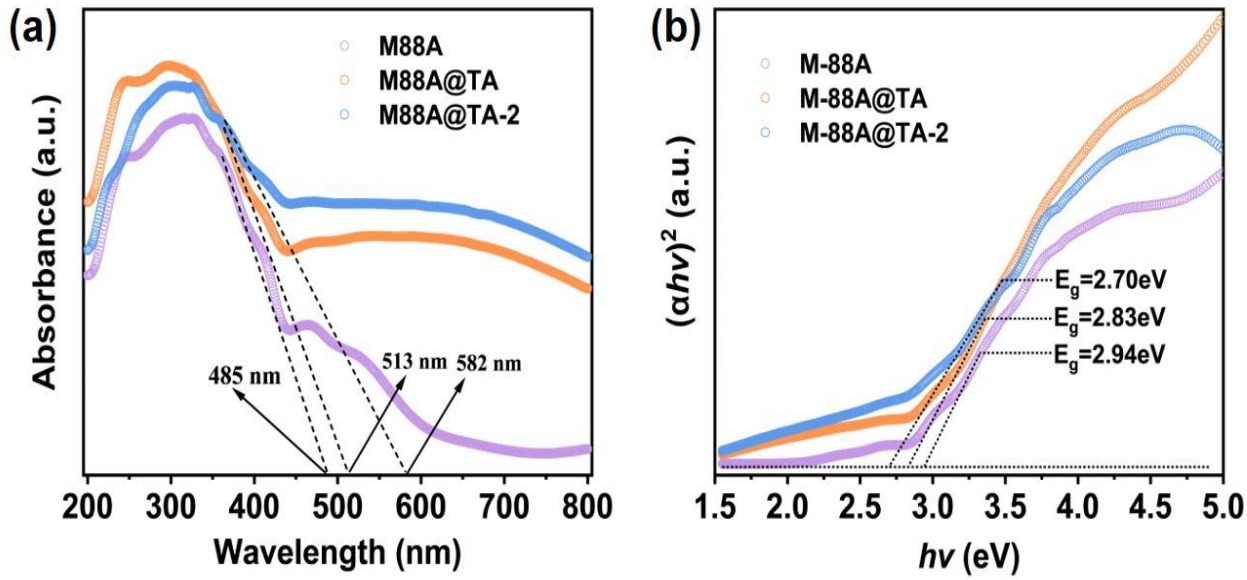

Figure 4.11 UV-Vis DRS spectra (a) and Tauc-plot of M88A, M88A@TA and M88A@TA-2 (b).

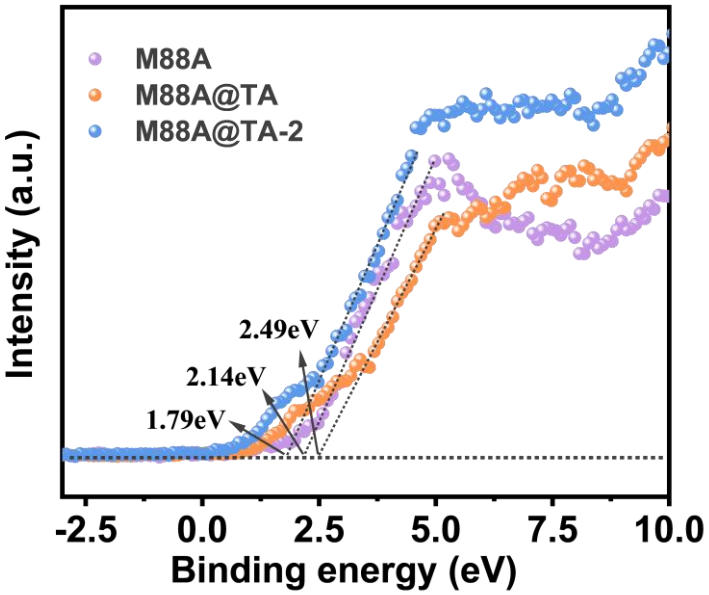

Figure 4.12 XPS valence band potential spectra of M88A, M88A@TA and M88A@TA-2 and corresponding valence band potentials.

This indicates that with the modification process, the spectral range that the material can absorb becomes wider and wider. In addition, the absorption intensity of M88A@TA-2 in the visible light region of 450–800 nm is also significantly better than that of M88A and M88A@TA, which is particularly important for photo-Fenton catalysis. Transforming the UV-Vis DRS yields a Tauc-plot. By fitting the curves, the band gaps of M88A, M88A@TA, and M88A@TA-2 are calculated to be 2.7 eV, 2.83 eV, and 2.94 eV, respectively (Figure 4.11b). Furthermore, XPS valence band potential spectra show that the HOMO potentials are 2.14 eV, 2.49 eV, and 1.79 eV, respectively (Figure 4.12).

4.5 Activity of MIL-88A@TA-X Fenton catalytic degradation of atrazine

4.5.1 Photo-Fenton degradation activity of atrazine by samples synthesized under different conditions

The photo-Fenton catalytic activity of the catalysts was evaluated using the herbicide atrazine (ATZ) as the target pollutant. First, we tested the materials prepared under different synthesis conditions according to the photo-Fenton experimental method described in Section 2.4.2 (Figure 4.13).

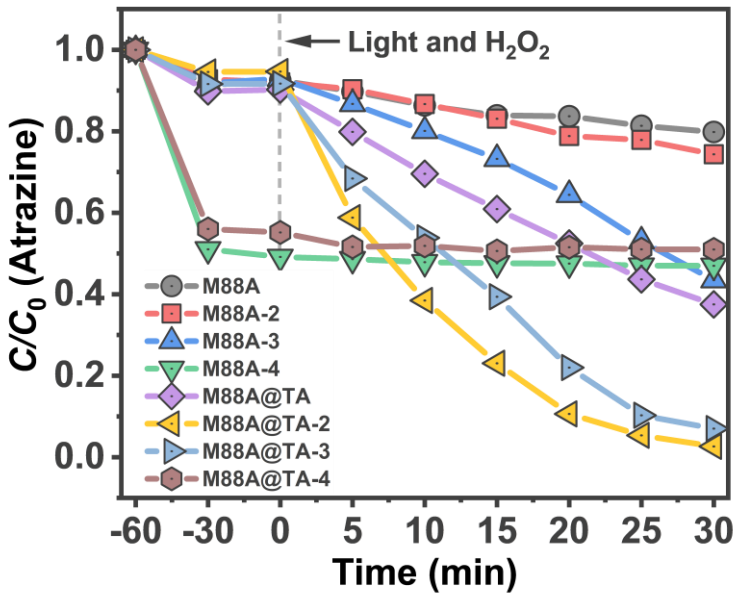

Figure 4.13 Performance of materials prepared under different synthesis conditions for photo-Fenton degradation of ATZ.

The results showed that M88A@TA-2 exhibited the highest photo-Fenton degradation activity among all the prepared materials. In contrast, the catalytic activity of M88A-2, prepared without TA modification and calcined at 200°C, was only slightly improved compared to that of M88A, highlighting the importance of TA modification. Furthermore, the catalytic activities of M88A-3 and M88A@TA-3, prepared after

calcination at 300°C, were also inferior to those of M88A@TA-2. This may be due to the high calcination temperature, which damaged the catalyst structure (as demonstrated in the characterization sections of Sections 4.2 and 4.3), thereby reducing the catalytic activity. M88A-4 and M88A@TA-4 completely lost their photo-Fenton catalytic performance, but they exhibited strong adsorption during the reaction. This is likely due to the carbonization of the MOF framework during high-temperature calcination, forming a porous carbon material with strong adsorption capacity. In summary, we used M88A, M88A@TA, and M88A@TA-2 as representative materials for subsequent catalytic performance studies.

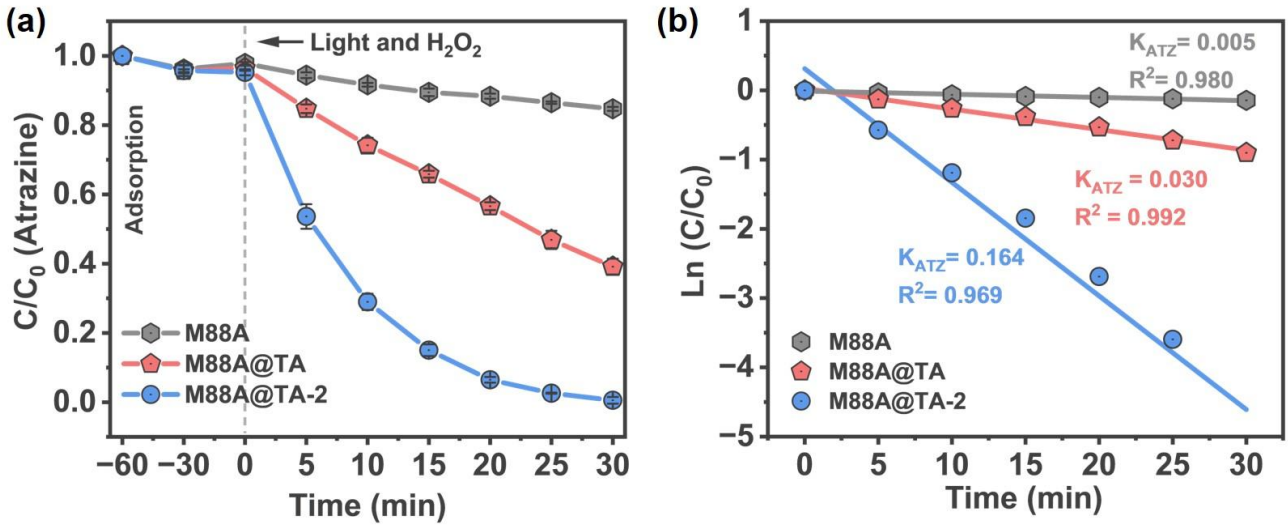

Figure 4.14 Photo-Fenton degradation activity curves (a) and degradation kinetics curves (b) of prepared materials.

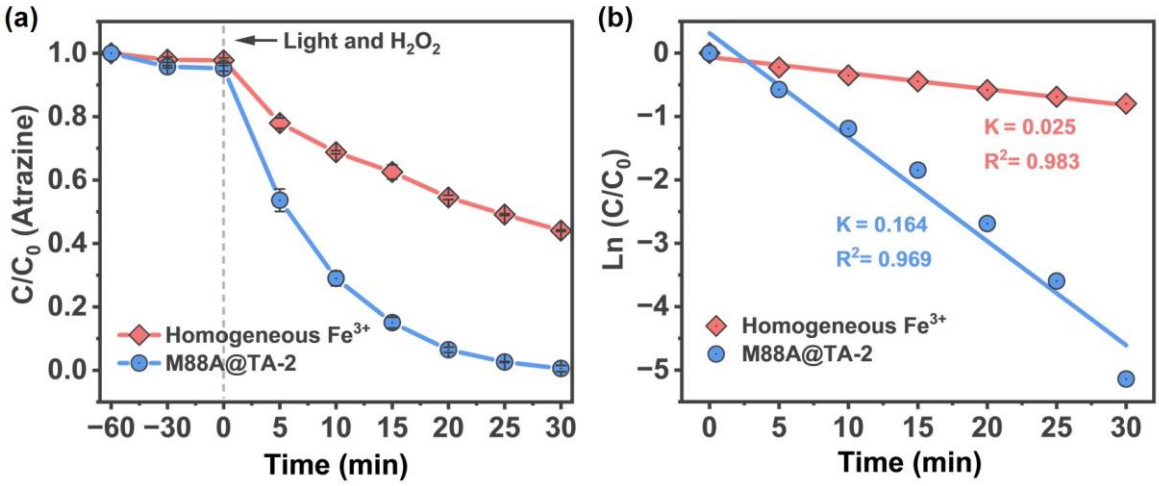

Figure 4.15 Comparison of the degradation kinetics of ATZ by M88A@TA-2 and homogeneous photo-Fenton.

To obtain a more detailed calculation of the catalytic activity of the modified materials, the reaction kinetic constants were calculated according to the method described in Section 2.5.1 (Figure 4.14). The results showed that the photo-Fenton kinetic constant, K(ATZ) for ATZ degradation by M88A@TA-2 was 0.164 min^{-1}, 32.8 times and 5.5 times that of M88A (0.005 min^{-1}) and M88A@TA (0.030 min^{-1}), respectively. We also compared the ATZ degradation kinetics of M88A@TA-2 with that of a homogeneous photo-Fenton reaction (Figure 4.15). The results showed that when using an Fe salt with an equivalent mass to the catalyst for the photo-Fenton reaction, the degradation kinetic constant was 0.025 min^{-1}, significantly lower than the degradation rate of M88A@TA-2. Therefore, M88A@TA-2 not only has advantages over unmodified M88A but also exhibits significant advantages over traditional homogeneous catalysts.

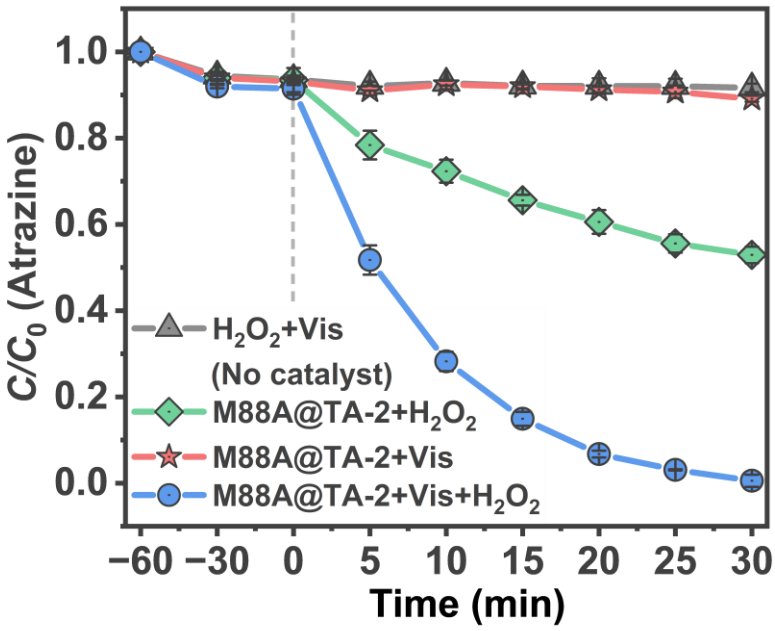

Figure 4.16 Controlled experiments on the degradation of the pollutant ATZ by M88A@TA-2 under different conditions.

In the photo-Fenton reaction, H_2O_2, as an oxidant, is crucial for the catalytic reaction. Furthermore, light, as a source of external energy, is also indispensable. However, for newly developed photo-Fenton catalysts, we need to determine whether their photo-Fenton activity is a simple superposition of pure photocatalysis and heterogeneous Fenton reactions, or whether a 1+1>2 synergistic effect exists. Therefore, it is necessary to verify the performance of pure photocatalysis in the absence of an oxidant, as well as the performance of pure heterogeneous Fenton reactions in the absence of light. We selected the top-performing M88A@TA-2 as the test material and tested its kinetics for the pure photocatalytic degradation of ATZ without the addition of H_2O_2. We also tested its degradation kinetics with the addition of H_2O_2 alone, without light. Furthermore, we conducted a control experiment with

visible light and H_2O_2 alone, without a catalyst. The results, shown in Figure 4.16, show that ATZ does not degrade when the reaction system is exposed to visible light and H_2O_2 only, without a catalyst, indicating that H_2O_2 does not directly degrade ATZ. When the reaction system contains only the catalyst and visible light, ATZ does not degrade, indicating that M88A@TA-2 cannot directly degrade ATZ through photocatalytic reactions. However, when the reaction system contains the catalyst and H_2O_2 but no visible light, ATZ can be degraded, but the reaction rate is far lower than that of the M88A@TA-2/H_2O_2/Vis photo-Fenton system. This suggests that while M88A@TA-2 possesses heterogeneous Fenton catalytic properties, increasing illumination can create a synergistic effect with the Fenton reaction. Therefore, it is crucial to apply M88A@TA-2 to the photo-Fenton reaction to fully exploit the synergistic effect between the Fenton reaction and visible light.

4.5.2 Photo-Fenton degradation activity of samples at different pH values

Typically, the Fenton reaction is highly sensitive to pH, which is related to the activation of H_2O_2 and the Fe^{3+}/Fe^{2+} cycle in the Fenton reaction (detailed discussion in Section 1.4.3). For heterogeneous Fenton reactions, pH also affects the catalytic activity of the catalyst. Considering the practical application of heterogeneous Fenton catalysts, the catalyst needs to have a wide pH operating range to accommodate complex real-world application environments. Therefore, we tested the degradation kinetics of ATZ by the M88A@TA-2 photocatalytic Fenton system at different pH values.

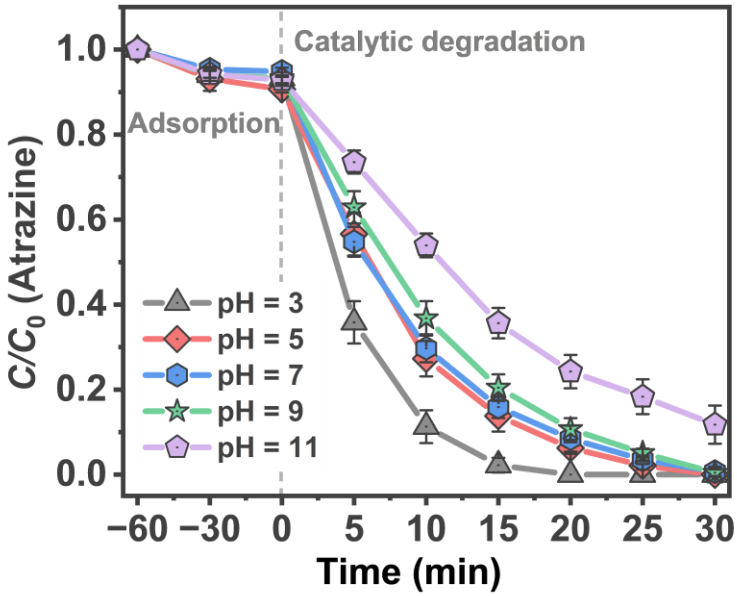

Figure 4.17 Removal performance of ATZ by the M88A@TA-2/H_2O_2 Fenton system at different pH values.

The results are shown in Figure 4.17. At pH 3, the catalyst exhibits the fastest degradation rate, consistent with the characteristic of Fenton reactions having faster reaction rates at lower pH values. When the pH is between 5 and 9, M88A@TA-2 maintains a stable and rapid reaction rate. At pH 11, the reaction rate of M88A@TA-2 decreases to some extent, but it can still degrade approximately 88% of ATZ within 30 minutes. In summary, M88A@TA-2 exhibits good pH adaptability, which is advantageous for its future practical applications.

4.5.3 Photo-Fenton degradation activity of samples atrazine under different H_2O_2 addition amounts

High H_2O_2 consumption and low utilization efficiency have long been a difficult problem for traditional Fenton systems. This issue remains a pressing challenge in

heterogeneous Fenton research. Therefore, we tested the degradation kinetics of ATZ by M88A@TA-2 at varying amounts of added hydrogen peroxide.

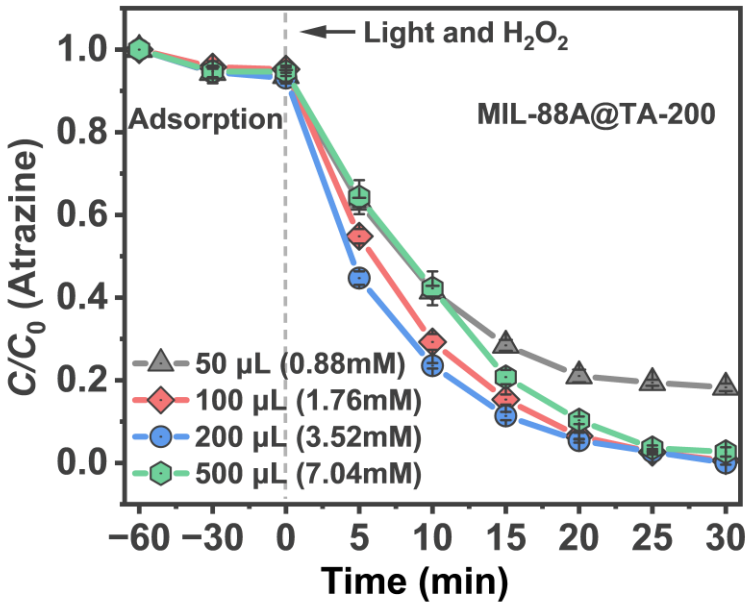

Figure 4.18 Degradation kinetic curves of ATZ by the M88A@TA-2/H_2O_2 photo-Fenton system with different hydrogen peroxide addition amounts.

The results, shown in Figure 4.18, show that M88A@TA-2 can degrade nearly 100% of ATZ within 30 minutes at a H_2O_2 concentration of 1.76 mM. At this H_2O_2 concentration, the molar ratio of pollutant (ATZ) to H_2O_2 is 38:1, significantly lower than the 65:1 to 500:1 reported for other heterogeneous Fenton systems [102][103][104]. This demonstrates the high H_2O_2 utilization efficiency of M88A@TA-2, which facilitates its practical application.

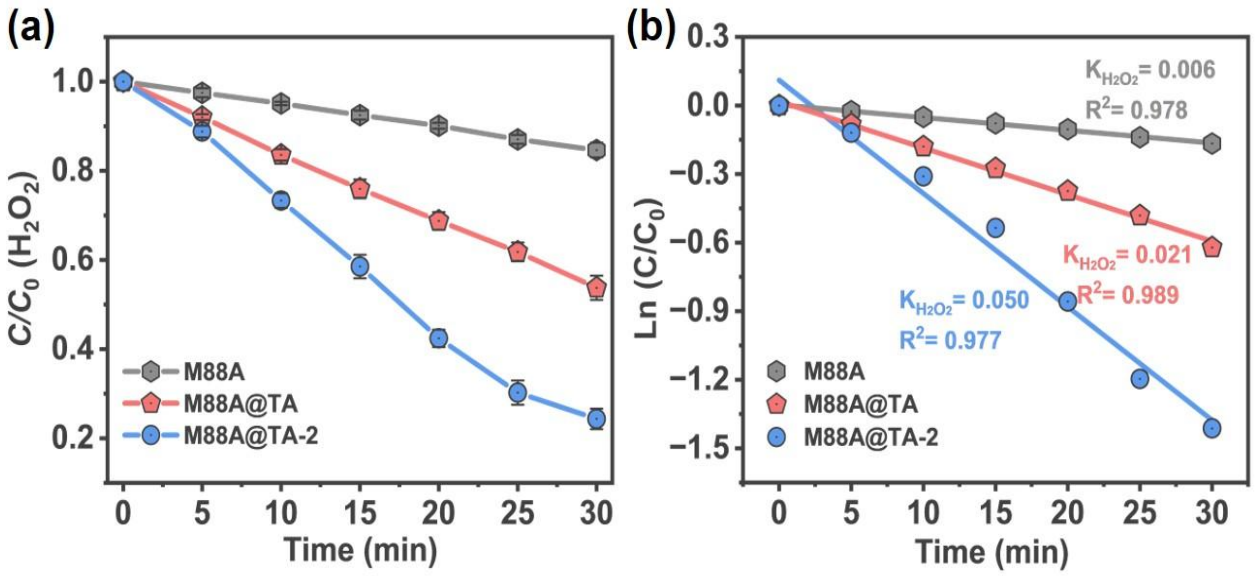

Figure 4.19 H_2O_2 consumption curves (b) and kinetic fitting curves (c).

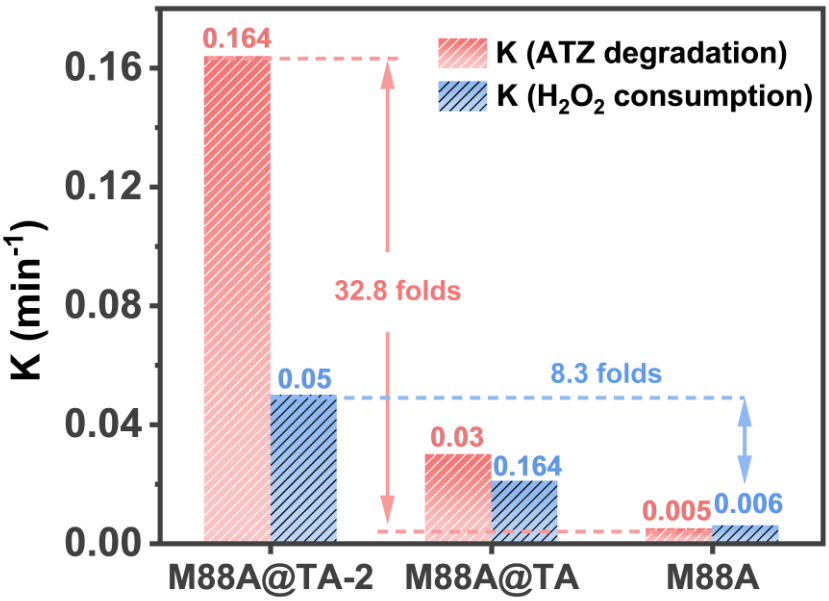

Figure 4.20 The reaction rate constant of ATZ degradation by the prepared material and the rate constant of H_2O_2 consumption during the reaction.

To more accurately calculate the activation efficiency of H_2O_2, we measured the H_2O_2 consumption rate during the photo-Fenton reaction. The results are shown in Figure 4.19. The H_2O_2 consumption rate constant, $K(H_2O_2)$, for M88A@TA-2 is 0.052 min^{-1}, which is 10.4 times and 2.5 times that of M88A (0.005 min^{-1}) and M88A@TA (0.021 min^{-1}), respectively. A faster H_2O_2 consumption rate generally indicates a faster conversion of H_2O_2 to ROS, which is one of the reasons for the higher catalytic activity of M88A@TA-2. Furthermore, we compared the degradation kinetic constant of M88A@TA-2 with the H_2O_2 consumption rate constant of M88A@TA-2. The results are shown in Figure 4.20. The degradation rate constant of ATZ by M88A@TA-2 is 32.8 times higher than that of M88A, while the consumption rate of H_2O_2 is only increased by 8.3 times, indicating that the utilization efficiency of hydrogen peroxide is increased by about 4 times.

4.5.4 Photo-Fenton degradation activity of atrazine in the presence of different reactive oxygen species quenchers

For ROS-dependent advanced oxidation reactions, identifying the primary ROS species during the catalytic reaction is crucial for understanding the catalytic mechanism of the material. Therefore, we conducted a series of experiments using various ROS scavengers. The detailed steps are described in Section 2.4.3. The results are shown in Figure 4.21.

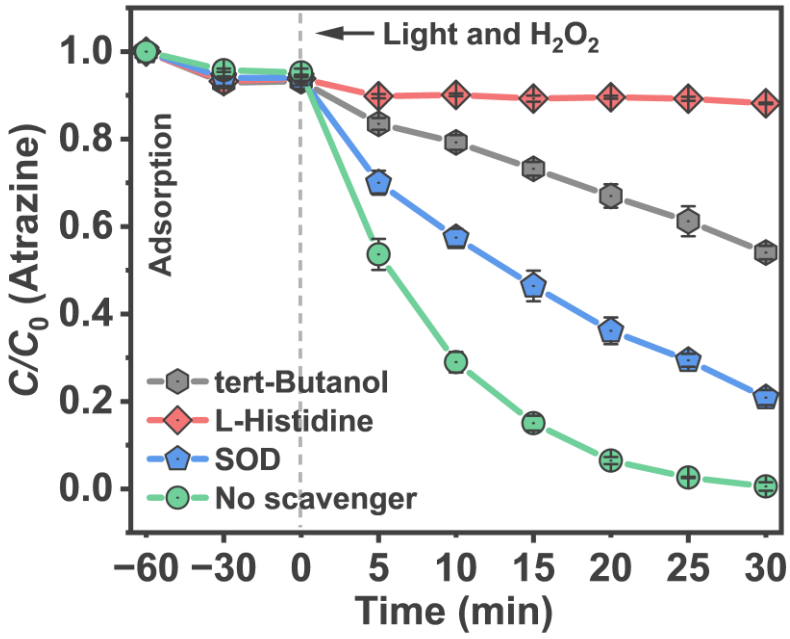

Figure 4.21 Kinetics curves of M88A@TA-2 photocatalytic degradation of ATZ under the condition of adding different ROS scavengers.

Adding superoxide dismutase (SOD, a $\cdot O_2^-$ scavenger) to the M88A@TA-2/H_2O_2/ATZ photo-Fenton system reduced the ATZ removal efficiency from 100% to 80%. Adding tert-butyl alcohol (TBA, a ·OH scavenger) reduced the ATZ removal efficiency to approximately 35%. Adding L-histidine ($^1O_2$ scavenger) almost halted the degradation reaction. This indicates that $^1O_2$ and ·OH are the key ROS species in the catalytic process, with $\cdot O_2^-$ also playing a minor role in the catalytic reaction.

4.5.5 Identification of reactive oxygen species during photo-Fenton degradation by EPR spectroscopy

Electron paramagnetic resonance (EPR) spectroscopy was used to identify and relatively quantify reactive oxygen species (ROS) in the photo-Fenton reaction system,

further exploring the source of the high catalytic activity of M88A@TA-2.

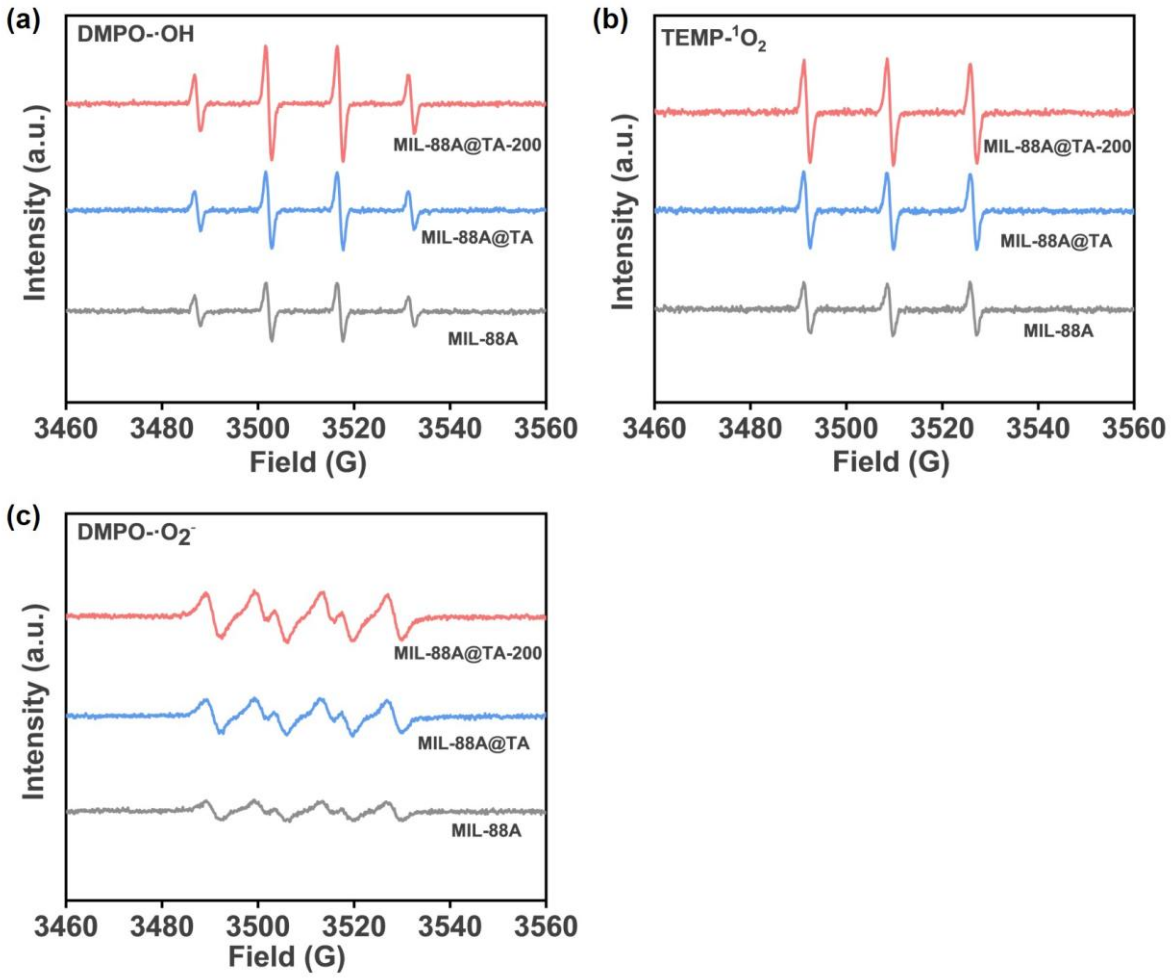

Figure 4.22 Measurement by EPR of DMPO-·OH (a), TEMP-$^1O_2$ (b) and DMPO-·O_2^- (c) on M88A, M88A@TA, M88A@TA-2.

Detailed procedures are described in 2.4.3. As shown in Figure 4.22a, when DMPO was used as a scavenger, the DMPO-·OH adduct appeared as a quartet with a 1:2:2:1 ratio in the EPR spectrum. ·OH signals were detected for M88A@TA-2, M88A@TA, and M88A, but the signal for M88A@TA-2 was stronger, indicating that it could generate more ·OH. Figure 4.22b shows the EPR spectrum using TEMP as a $^1O_2$ scavenger. The EPR signal for TEMP-$^1O_2$ was a triplet with a 1:1:1 ratio. $^1O_2$

signals were detected for M88A@TA-2, M88A@TA, and M88A, with the $^1O_2$ signal for M88A@TA-2 remaining the strongest of the three materials. Figure 4.22 c shows the DMPO-·O_2^- spectrum using DMPO as a scavenger. The ·O_2^- signal is a quartet with a 1:1:1:1 ratio. Weaker ·O_2^- signals were detected for M88A@TA-2, M88A@TA, and M88A, but M88A@TA-2 still possessed the highest intensity. Combining these three EPR results further confirms that the prepared material can generate ·OH, $^1O_2$, and ·O_2^-, demonstrating that M88A@TA-2 possesses a stronger ability to activate H_2O_2 into ROS.

4.6 Analysis of degradation products of atrazine by photo-Fenton degradation

To further validate the key role of each ROS species in the reaction, we identified ATZ degradation products in the M88A@TA-2 photo-Fenton system using UPLC-QTOF-MS, following the method in Section 2.5.3. Furthermore, we identified degradation products in samples from the experiment described in Section 4.5.4 after the addition of different ROS scavengers. Based on the identified transformation products and the effects of different ROS scavengers on the degradation products, we deduced the reaction pathways for ATZ degradation by M88A@TA-2 (Table 4.3, Figure 4.23).

Table 4.3 Results of degradation product measurements in the M88A@TA-2/H_2O_2 system and the scavenger addition system

Product name	Molecular Formula	No scavenger	·OH scavenger	$^1O_2$ scavenger	$\cdot O_2^-$ scavenger
ATZ	$C_8H_{14}ClN_5$				
P232	$C_8H_{14}ClN_5O$	●	●	●	●
P230	$C_8H_{12}ClN_5O$	●	●	●	●
P212	$C_8H_{13}N_5O_2$	●	●	●	●
P188-1	$C_5H_6ClN_5O$	●	●	◎	●
P188-2	$C_6H_{10}N_5Cl$	●	●	◎	●
P174	$C_5H_8N_5Cl$	●	●	◎	●
P146	$C_3H_4ClN_5$	●	◎	◎	●
●Detected ◎Not Detected					

Essentially, seven major transformation products were identified, and the transformation pathways included oxidation reactions (hydroxylation and carbonylation) and dealkylation. Based on the effects of various ROS scavengers on the transformation products, it can be inferred that $^1O_2$ dominates the dealkylation reaction of the ATZ side chain (products $C_5H_6ClN_5O$, $C_6H_{10}N_5Cl$, and $C_5H_8N_5Cl$), while ·OH dominates the oxidation reaction of the ATZ side chain (products $C_8H_{14}ClN_5O$, $C_8H_{12}ClN_5O$, and $C_8H_{13}N_5O_2$), and $^1O_2$ and ·OH jointly dominate the de-acylation reaction (product $C_3H_4ClN_5$). However, O_2^- did not affect the formation of any transformation products, indicating that $\cdot O_2^-$ is not the primary active species, which is consistent with the results of ROS scavenging experiments. In summary, the

degradation of ATZ is attributed to the synergistic action of multiple ROS.

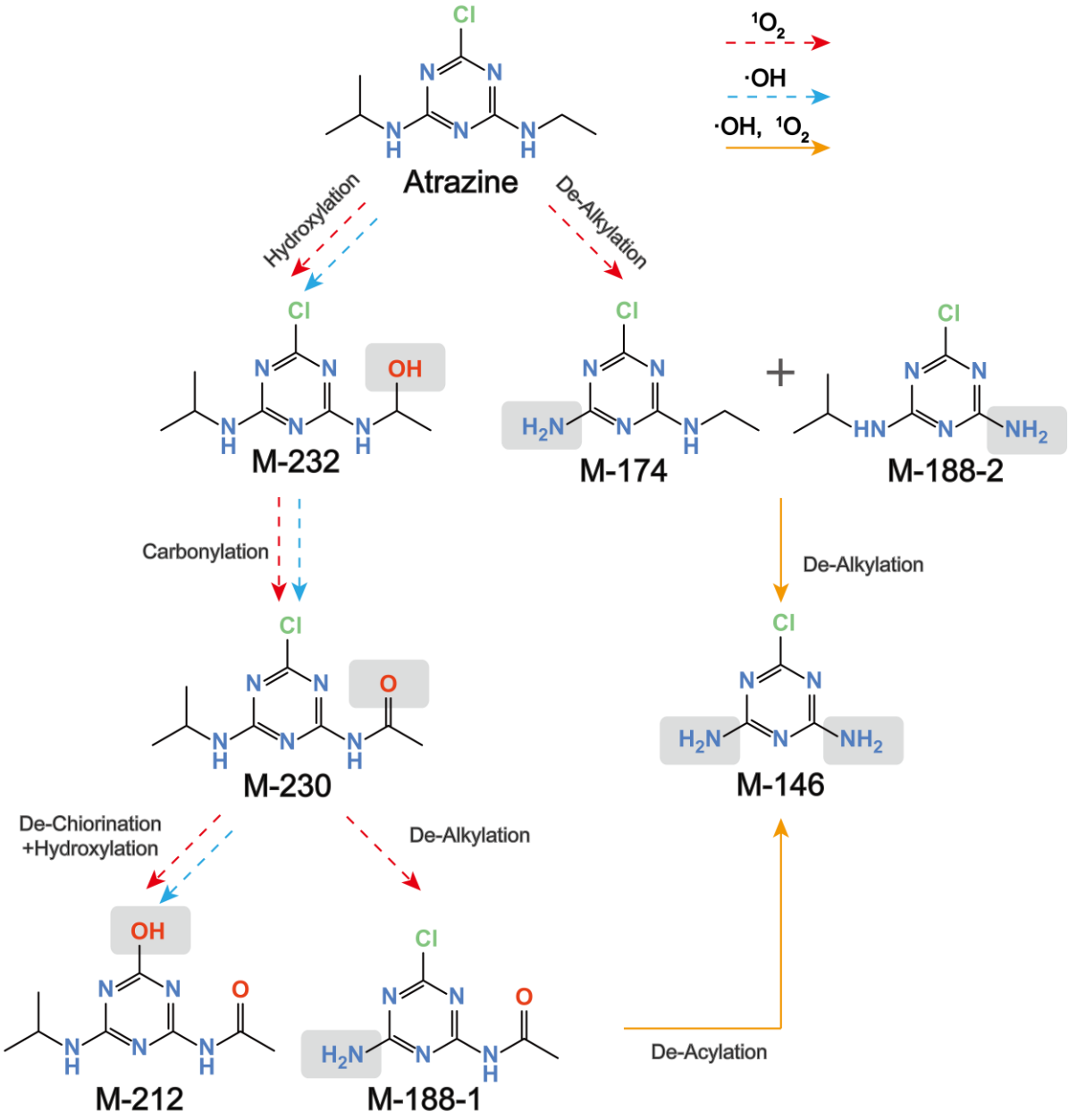

Figure 4.23 Proposed degradation pathways of ATZ inferred from screening of degradation products in the M88A@TA-2/H_2O_2 system and in the system after scavenger addition, and the role of different ROS in the degradation process.

Conclusion of Chapter 4

1. The Fe-based MOF M88A, TA-modified M88A@TA, and M88A@TA-2 synthesized by TA modification followed by calcination were successfully synthesized. The morphology and phase structure of the prepared materials were characterized by XRD, SEM, TEM, EDX, and BET. The results showed that the tannic acid modification and calcination process resulted in a loose and porous structure in M88A@TA-2, and its crystal structure also exhibited abundant defects.

2. The chemical structure of the prepared materials was analyzed by FTIR, TGA, and XPS. FTIR results showed that tannic acid modification and calcination at 200°C did not destroy the basic chemical structure of the MOF, but M88A@TA-2 had abundant defects, exposing more carboxyl groups. TGA and XPS further confirmed that M88A@TA-2 had a higher defect abundance.

3. The band structure and light absorption capacity of the prepared materials were characterized by UV-Vis DRS, Tauc-plots, and XPS valence band potential spectroscopy. Results indicate that the modified material M88A@TA-2 exhibits a narrower energy band and stronger light absorption.

4. Catalytic activity testing showed that, thanks to its high specific surface area, abundant defects, and excellent light absorption capacity, M88A@TA-2 exhibited the best photocatalytic Fenton activity among all the materials prepared. Furthermore, M88A@TA-2 exhibits a wide pH range and higher H_2O_2 utilization efficiency. ROS scavenging experiments and EPR measurements indicate that the primary ROS species involved in the photo-Fenton degradation of ATZ by M88A@TA-2 are ·OH and $^1O_2$.

The results of this chapter were published in:

Research articles:

4. Wang, W., Shi, H., Shi, H., **Zhou, Z.**, Mao, L., Zhang, L., ... & Liu, X. Application of modified biochar in integrated pollution management for pesticides and antibiotics in water: Recent advances and future prospects. *Environmental Research*, 2025, 285: 122499. https://doi.org/10.1016/j.envres.2025.122499.

CONCLUSIONS

1. A review of the literature on pesticide contamination of water and methods for removing organic pesticide contaminants from water was conducted. The results of this literature review indicate that photocatalytic technologies using MOF-based nanomaterials as catalysts and heterogeneous photo-Fenton techniques show great potential for degrading organic pesticide contaminants.

2. A series of Ti-MOF-based composite photocatalysts (NH_2-MIL-125/TiO_2) were synthesised. XRD analysis demonstrated that the NH_2-MIL-125/TiO_2 composites possessed the lattice characteristics of both NH_2-MIL-125 and TiO_2. FTIR characterization revealed that the composites of NH_2-MIL-125 and TiO_2 exhibited little change in their infrared structure. Furthermore, SEM analysis visually observed dispersed TiO_2 nanoparticles on the surface of the NH_2-MIL-125/TiO_2 composites. These results demonstrate the successful construction of the composites. We also measured UV-Vis DRS spectra of NH_2-MIL-125/TiO_2, NH_2-MIL-125, and TiO_2. Results showed that the absorption edge of NH_2-MIL-125/TiO_2 is at 533 nm, which is stronger than that of NH_2-MIL-125 (510 nm) and TiO_2 (385 nm).

3. Photocatalytic performance tests were conducted using imidacloprid as the target pollutant. Results demonstrated that the photocatalytic activity of the NH_2-MIL-125/TiO_2 composite material was significantly improved compared to that of NH_2-MIL-125. We found that materials synthesized with a TiO_2/TPOT ratio of 100% or higher exhibited high catalytic activity, achieving near 100% degradation of imidacloprid within 90 minutes.

4. For photo-Fenton catalyst research, we used the Fe-based MOF MIL-88A as the base material, first modifying it with tannic acid to synthesize M88A@TA, and

then calcining it at different temperatures to synthesize M88A@TA-X. XRD, SEM, TEM, and BET characterizations demonstrated that M88A@TA-2, synthesized after tannic acid modification and calcination at 200°C, possesses a porous structure and abundant lattice defects, increasing its specific surface area from 13 m^2/g for M88A to 44 m^2/g.

5. FTIR, TGA, and XPS characterization of M88A@TA-2 further confirmed its abundant defects while maintaining a stable structure. UV-vis DRS results showed that M88A@TA-2 has an absorption edge at 582 nm and a band gap of 2.70 eV, while MIL-88A has an absorption edge at 485 nm and a band gap of 2.94 eV. This is attributed to the optimized band structure of M88A@TA-2 due to its abundant defects.

6. The photo-Fenton activity of M88A, M88A@TA, and M88A@TA-2 was tested against atrazine as the target pollutant. M88A@TA-2 exhibited the best activity, with reaction rate constants 32.8 and 5.5 times those of M88A and M88A@TA, respectively. Furthermore, ROS scavenging experiments and EPR spectroscopy confirmed that the main ROS in the M88A@TA-2 photo-Fenton system were ·OH and $^1O_2$. Furthermore, we tested the photo-Fenton activity of M88A@TA-2 at different H_2O_2 addition levels. The results showed that M88A@TA-2 could degrade 100% of atrazine within 30 minutes at a low H_2O_2 concentration of 1.76 mM, and its catalytic activity remained stable in the pH range of 3-9. This demonstrates that M88A@TA-2 has high H_2O_2 utilization efficiency and pH adaptability, which gives it great potential for practical applications.

REFERENCES

[1] T. Oki and S. Kanae, “Global Hydrological Cycles and World Water Resources,” *Science*, vol. 313, no. 5790, pp. 1068–1072, Aug. 2006, doi: 10.1126/science.1128845.

[2] C. J. Vörösmarty *et al.*, “Global threats to human water security and river biodiversity,” *Nature*, vol. 467, no. 7315, pp. 555–561, 2010, doi: 10.1038/nature09440.

[3] T. Tao and K. Xin, “Public health: A sustainable plan for China’s drinking water,” *Nature*, vol. 511, no. 7511, pp. 527–528, 2014, doi: 10.1038/511527a.

[4] D. Cutler and G. Miller, “The role of public health improvements in health advances: The twentieth-century United States,” *Demography*, vol. 42, no. 1, pp. 1–22, 2005, doi: 10.1353/dem.2005.0002.

[5] J. Jalan and M. Ravallion, “Does piped water reduce diarrhea for children in rural India?,” *J. Econom.*, vol. 112, no. 1, pp. 153–173, 2003, doi: https://doi.org/10.1016/S0304-4076(02)00158-6.

[6] A. Ebenstein, “The Consequences of Industrialization: Evidence from Water Pollution and Digestive Cancers in China,” *Rev. Econ. Stat.*, vol. 94, no. 1, pp. 186–201, Feb. 2012, doi: 10.1162/REST_a_00150.

[7] Y. Lu *et al.*, “Impacts of soil and water pollution on food safety and health risks in China,” *Environ. Int.*, vol. 77, pp. 5–15, 2015, doi: https://doi.org/10.1016/j.envint.2014.12.010.

[8] N. M. Norida Mazlan, M. A. Mohammed Ahmed, F. M. M. Farrah Melissa Muharam, and M. A. A. Md. Amirul Alam, “Status of persistent organic pesticide residues in water and food and their effects on environment and farmers: a

comprehensive review in Nigeria.," *Semin. Ciências Agrárias*, vol. 38, no. 4 PP-Londrina, pp. 2221–2236, 2017, doi: 10.5433/1679-0359.2017v38n4p2221.

[9] C. E. Rose, R. H. Coupe, P. D. Capel, and R. M. T. Webb, "Holistic assessment of occurrence and fate of metolachlor within environmental compartments of agricultural watersheds," *Sci. Total Environ.*, vol. 612, pp. 708–719, 2018, doi: https://doi.org/10.1016/j.scitotenv.2017.08.154.

[10] Y. Wang, S. Zhang, W. Cui, X. Meng, and X. Tang, "Polycyclic aromatic hydrocarbons and organochlorine pesticides in surface water from the Yongding River basin, China: Seasonal distribution, source apportionment, and potential risk assessment," *Sci. Total Environ.*, vol. 618, pp. 419–429, 2018, doi: https://doi.org/10.1016/j.scitotenv.2017.11.066.

[11] D. Luo, T. Zhou, Y. Tao, Y. Feng, X. Shen, and S. Mei, "Exposure to organochlorine pesticides and non-Hodgkin lymphoma: a meta-analysis of observational studies," *Sci. Rep.*, vol. 6, no. 1, p. 25768, 2016, doi: 10.1038/srep25768.

[12] M. Brouwer *et al.*, "Environmental exposure to pesticides and the risk of Parkinson's disease in the Netherlands," *Environ. Int.*, vol. 107, pp. 100–110, 2017, doi: https://doi.org/10.1016/j.envint.2017.07.001.

[13] C. S. Mazur, S. A. Marchitti, and J. Zastre, "P-glycoprotein inhibition by the agricultural pesticide propiconazole and its hydroxylated metabolites: Implications for pesticide–drug interactions," *Toxicol. Lett.*, vol. 232, no. 1, pp. 37–45, 2015, doi: https://doi.org/10.1016/j.toxlet.2014.09.020.

[14] S. Thongprakaisang, A. Thiantanawat, N. Rangkadilok, T. Suriyo, and J. Satayavivad, "Glyphosate induces human breast cancer cells growth via estrogen

receptors," *Food Chem. Toxicol.*, vol. 59, pp. 129–136, 2013, doi: https://doi.org/10.1016/j.fct.2013.05.057.

[15] W. Huang, X. Zhang, and W. Chen, "Role of oxidative stress in Alzheimer's disease (Review)," *Biomed Rep*, vol. 4, no. 5, pp. 519–522, 2016, doi: 10.3892/br.2016.630.

[16] D. Yan, Y. Zhang, L. Liu, and H. Yan, "Pesticide exposure and risk of Alzheimer's disease: a systematic review and meta-analysis," *Sci. Rep.*, vol. 6, no. 1, p. 32222, 2016, doi: 10.1038/srep32222.

[17] Q. Zhou, H. Sun, L. Jia, W. Wu, and J. Wang, "Simultaneous biological removal of nitrogen and phosphorus from secondary effluent of wastewater treatment plants by advanced treatment: A review," *Chemosphere*, vol. 296, p. 134054, 2022, doi: https://doi.org/10.1016/j.chemosphere.2022.134054.

[18] L. Chen, H. Ji, J. Qi, T. Huang, C.-C. Wang, and W. Liu, "Degradation of acetaminophen by activated peroxymonosulfate using $Co(OH)_2$ hollow microsphere supported titanate nanotubes: Insights into sulfate radical production pathway through $CoOH^+$ activation," *Chem. Eng. J.*, vol. 406, p. 126877, 2021, doi: https://doi.org/10.1016/j.cej.2020.126877.

[19] P. Xie, C. Chen, C. Zhang, G. Su, N. Ren, and S.-H. Ho, "Revealing the role of adsorption in ciprofloxacin and sulfadiazine elimination routes in microalgae," *Water Res.*, vol. 172, p. 115475, 2020, doi: https://doi.org/10.1016/j.watres.2020.115475.

[20] X. Kang, Q. Zhang, X. Liu, J. Song, H. Guo, and L. Wang, "The interface mechanism of sludge biochar activating persulfate to remove tetracycline: The role of the C-O-Fe bridge at the carbon surface," *J. Clean. Prod.*, vol. 384, p.

135514, 2023, doi: https://doi.org/10.1016/j.jclepro.2022.135514.

[21] M. Zou, W. Tian, J. Zhao, M. Chu, and T. Song, “Quinolone antibiotics in sewage treatment plants with activated sludge treatment processes: A review on source, concentration and removal,” *Process Saf. Environ. Prot.*, vol. 160, pp. 116–129, 2022, doi: https://doi.org/10.1016/j.psep.2022.02.013.

[22] S. J. Seema Jilani and M. A. Khan, “Treatment of toxic organics in industrial waste water using activated sludge process.,” *Am. J. Agric. & Environ. Sci.*, vol. 14, no. 3, pp. 231–239, 2014, [Online]. Available: http://www.idosi.org/aejaes/jaes14(3)14/9.pdf

[23] M. Sun, L. Yan, L. Zhang, L. Song, J. Guo, and H. Zhang, “New insights into the rapid formation of initial membrane fouling after in-situ cleaning in a membrane bioreactor,” *Process Biochem.*, vol. 78, pp. 108–113, 2019, doi: https://doi.org/10.1016/j.procbio.2019.01.004.

[24] D. S. Srinivasa Raghavan, G. Qiu, and Y.-P. Ting, “Fate and removal of selected antibiotics in an osmotic membrane bioreactor,” *Chem. Eng. J.*, vol. 334, pp. 198–205, 2018, doi: https://doi.org/10.1016/j.cej.2017.10.026.

[25] Y. Xiao, H. Yaohari, C. De Araujo, C. C. Sze, and D. C. Stuckey, “Removal of selected pharmaceuticals in an anaerobic membrane bioreactor (AnMBR) with/without powdered activated carbon (PAC),” *Chem. Eng. J.*, vol. 321, pp. 335–345, 2017, doi: https://doi.org/10.1016/j.cej.2017.03.118.

[26] C. Vural *et al.*, “Assessment of Microbial and Ecotoxicological Qualities of Industrial Wastewater Treated with Membrane Bioreactor (MBR) Process for Agricultural Irrigation,” *Water, Air, Soil Pollut.*, vol. 232, no. 11, p. 442, 2021, doi: 10.1007/s11270-021-05372-0.

[27] A. Priyadarshini, L. Hong, and R. Bera, “Phosphonium-defoliated GO nanosheets as micropore booster of carbon membrane to improve separation of tetracycline from isopropanol,” *J. Environ. Chem. Eng.*, vol. 10, no. 3, p. 107496, 2022, doi: https://doi.org/10.1016/j.jece.2022.107496.

[28] J. J. S. Alonso, N. El Kori, N. Melián-Martel, and B. Del Río-Gamero, “Removal of ciprofloxacin from seawater by reverse osmosis,” *J. Environ. Manage.*, vol. 217, pp. 337–345, 2018, doi: https://doi.org/10.1016/j.jenvman.2018.03.108.

[29] X. Q. Cheng, Y. Liu, Z. Guo, and L. Shao, “Nanofiltration membrane achieving dual resistance to fouling and chlorine for ‘green’ separation of antibiotics,” *J. Memb. Sci.*, vol. 493, pp. 156–166, 2015, doi: https://doi.org/10.1016/j.memsci.2015.06.048.

[30] A. Gupta, R. K. Vyas, and S. Vyas, “A review on antibiotics pervasiveness in the environment and their removal from wastewater,” *Sep. Sci. Technol.*, vol. 58, no. 2, pp. 326–344, Jan. 2023, doi: 10.1080/01496395.2022.2110120.

[31] X.-X. Wang, Z.-F. Meng, X. Liu, T. Wang, X.-L. Hu, and X.-X. Sun, “[Adsorption of BS-18 Amphoterically Modified Bentonite to Tetracycline and Norfloxacin Combined Pollutants],” *Huan jing ke xue= Huanjing kexue*, vol. 42, no. 5, pp. 2334–2342, 2021, doi: 10.13227/j.hjkx.202009048.

[32] J. Lin *et al.*, “Ultra-fast adsorption of four typical pollutants using magnetically separable ethanolamine-functionalized graphene,” *Sep. Purif. Technol.*, vol. 271, p. 118862, 2021, doi: https://doi.org/10.1016/j.seppur.2021.118862.

[33] Y. Liu *et al.*, “Fabrication of attapulgite/C_3N_4 hybridized metal organic framework nanocomposites by different strategies and study on adsorption properties for alizarin yellow GG,” *Powder Technol.*, vol. 397, p. 117113, 2022,

doi: https://doi.org/10.1016/j.powtec.2022.117113.

[34] S. Feijoo, X. Yu, M. Kamali, L. Appels, and R. Dewil, “Generation of oxidative radicals by advanced oxidation processes (AOPs) in wastewater treatment: a mechanistic, environmental and economic review,” *Rev. Environ. Sci. Bio/Technology*, vol. 22, no. 1, pp. 205–248, 2023, doi: 10.1007/s11157-023-09645-4.

[35] S. Tang *et al.*, “$MnFe_2O_4$ nanoparticles promoted electrochemical oxidation coupling with persulfate activation for tetracycline degradation,” *Sep. Purif. Technol.*, vol. 255, p. 117690, 2021, doi: https://doi.org/10.1016/j.seppur.2020.117690.

[36] X. Runjing, L. Liang, F. Xiaojie, Y. Liu, J. Yunjing, and L. Liuqiang, “Catalytic Ozonation of Ciprofloxacin with Cu–Al Layered Double Hydroxides Based on Response Surface Analysis,” *J. Environ. Eng.*, vol. 148, no. 4, p. 4022010, Apr. 2022, doi: 10.1061/(ASCE)EE.1943-7870.0001988.

[37] R. Li, J. Xiong, Y. Zhang, S. Wang, H. Zhu, and L. Lu, “Catalytic Ozonation of Norfloxacin Using Co-Mn/CeO_2 as a Multi-Component Composite Catalyst,” 2022. doi: 10.3390/catal12121606.

[38] N. H. Mohamad Idris, K. Y. Cheong, B. J. Kennedy, T. Ohno, and H. L. Lee, “Buoyant titanium dioxide (TiO_2) as high performance photocatalyst and peroxide activator: A critical review on fabrication, mechanism and application,” *J. Environ. Chem. Eng.*, vol. 10, no. 3, p. 107549, 2022, doi: https://doi.org/10.1016/j.jece.2022.107549.

[39] T. L. Nguyen *et al.*, “Improved photodegradation of antibiotics pollutants in wastewaters by advanced oxidation process based on Ni-doped TiO_2,”

Chemosphere, vol. 302, p. 134837, 2022, doi: https://doi.org/10.1016/j.chemosphere.2022.134837.

[40] Y. Lin, Y. Zhang, and G. Li, "Promotion of sulfameter degradation by coupling persulfate and photocatalytic advanced oxidation processes with Fe-doped MOFs," *Sep. Purif. Technol.*, vol. 282, p. 119632, 2022, doi: https://doi.org/10.1016/j.seppur.2021.119632.

[41] N. Wang, T. Zheng, G. Zhang, and P. Wang, "A review on Fenton-like processes for organic wastewater treatment," *J. Environ. Chem. Eng.*, vol. 4, no. 1, pp. 762–787, 2016, doi: https://doi.org/10.1016/j.jece.2015.12.016.

[42] Y. Liu *et al.*, "FeOx nanoclusters decorated TiO_2 for boosting white LED driven photocatalytic Fenton-like norfloxacin degradation," *Sep. Purif. Technol.*, vol. 303, p. 122194, 2022, doi: https://doi.org/10.1016/j.seppur.2022.122194.

[43] X. Lv, Y. Ma, Y. Li, and Q. Yang, "Heterogeneous Fenton-Like Catalytic Degradation of 2,4-Dichlorophenoxyacetic Acid by Nano-Scale Zero-Valent Iron Assembled on Magnetite Nanoparticles," 2020. doi: 10.3390/w12102909.

[44] F. Wang, X. Yu, M. Ge, and S. Wu, "One-step synthesis of TiO_2/γ-Fe_2O_3/GO nanocomposites for visible light-driven degradation of ciprofloxacin," *Chem. Eng. J.*, vol. 384, p. 123381, 2020, doi: https://doi.org/10.1016/j.cej.2019.123381.

[45] S. Rajendran, M. M. Khan, F. Gracia, J. Qin, V. K. Gupta, and S. Arumainathan, "Ce^{3+}-ion-induced visible-light photocatalytic degradation and electrochemical activity of ZnO/CeO_2 nanocomposite," *Sci. Rep.*, vol. 6, no. 1, p. 31641, 2016, doi: 10.1038/srep31641.

[46] Z. Yan, Z. Xu, B. Cheng, and C. Jiang, "Co_3O_4 nanorod-supported Pt with enhanced performance for catalytic HCHO oxidation at room temperature," *Appl.*

Surf. Sci., vol. 404, pp. 426–434, 2017, doi: https://doi.org/10.1016/j.apsusc.2017.02.010.

[47] R. Liao *et al.*, "Facile solvothermal synthesis of nitrogen-doped SnO_2 nanorods towards enhanced photocatalysis," *RSC Adv.*, vol. 12, no. 44, pp. 28629–28636, 2022, doi: 10.1039/D2RA04900G.

[48] Y. Wang *et al.*, "Ti_3C_2 MXene coupled with CdS nanoflowers as 2D/3D heterostructures for enhanced photocatalytic hydrogen production activity," *Int. J. Hydrogen Energy*, vol. 47, no. 52, pp. 22045–22053, 2022, doi: https://doi.org/10.1016/j.ijhydene.2022.05.014.

[49] Z. Zhou *et al.*, "Nitrogen vacancy mediated exciton dissociation in carbon nitride nanosheets: Enhanced hydroxyl radicals generation for efficient photocatalytic degradation of organic pollutants," *J. Hazard. Mater.*, vol. 387, 2020, doi: 10.1016/j.jhazmat.2020.122023.

[50] Q. Huang, Y. Hu, G. He, C. Lin, and C. Wei, "Photocatalytic oxidation of nitrogen oxides over {001}TiO_2: the influence of F− ions," *Environ. Sci. Pollut. Res.*, vol. 25, no. 35, pp. 35342–35351, 2018, doi: 10.1007/s11356-018-3435-7.

[51] Y. Hu, X. Song, S. Jiang, and C. Wei, "Enhanced photocatalytic activity of Pt-doped TiO_2 for NO_x oxidation both under UV and visible light irradiation: A synergistic effect of lattice Pt^{4+} and surface PtO," *Chem. Eng. J.*, vol. 274, pp. 102–112, 2015, doi: https://doi.org/10.1016/j.cej.2015.03.135.

[52] Z. Sheng, Z. Wu, Y. Liu, and H. Wang, "Gas-phase photocatalytic oxidation of NO over palladium modified TiO_2 catalysts," *Catal. Commun.*, vol. 9, no. 9, pp. 1941–1944, 2008, doi: https://doi.org/10.1016/j.catcom.2008.03.022.

[53] B. Naik, K. M. Parida, and C. S. Gopinath, "Facile Synthesis of N- and S-

Incorporated Nanocrystalline TiO_2 and Direct Solar-Light-Driven Photocatalytic Activity," *J. Phys. Chem. C*, vol. 114, no. 45, pp. 19473–19482, Nov. 2010, doi: 10.1021/jp1083345.

[54] S. Prabakaran, K. D. Nisha, S. Harish, J. Archana, and M. Navaneethan, "Yttrium incorporated TiO_2/rGO nanocomposites as an efficient charge transfer layer with enhanced mobility and electrical conductivity," *J. Alloys Compd.*, vol. 885, p. 160936, 2021, doi: https://doi.org/10.1016/j.jallcom.2021.160936.

[55] R. Röder *et al.*, "Multifunctional Nanoparticles by Coordinative Self-Assembly of His-Tagged Units with Metal–Organic Frameworks," *J. Am. Chem. Soc.*, vol. 139, no. 6, pp. 2359–2368, Feb. 2017, doi: 10.1021/jacs.6b11934.

[56] Y. Liu *et al.*, "Metal or metal-containing nanoparticle@MOF nanocomposites as a promising type of photocatalyst," *Coord. Chem. Rev.*, vol. 388, pp. 63–78, 2019, doi: https://doi.org/10.1016/j.ccr.2019.02.031.

[57] R.-B. Lin, S. Xiang, H. Xing, W. Zhou, and B. Chen, "Exploration of porous metal–organic frameworks for gas separation and purification," *Coord. Chem. Rev.*, vol. 378, pp. 87–103, 2019, doi: https://doi.org/10.1016/j.ccr.2017.09.027.

[58] L. E. Kreno, K. Leong, O. K. Farha, M. Allendorf, R. P. Van Duyne, and J. T. Hupp, "Metal–Organic Framework Materials as Chemical Sensors," *Chem. Rev.*, vol. 112, no. 2, pp. 1105–1125, Feb. 2012, doi: 10.1021/cr200324t.

[59] M. Filippousi *et al.*, "Biocompatible Zr-based nanoscale MOFs coated with modified poly(ε-caprolactone) as anticancer drug carriers," *Int. J. Pharm.*, vol. 509, no. 1, pp. 208–218, 2016, doi: https://doi.org/10.1016/j.ijpharm.2016.05.048.

[60] M. Alvaro, E. Carbonell, B. Ferrer, F. X. Llabrés i Xamena, and H. Garcia, "Semiconductor Behavior of a Metal-Organic Framework (MOF)," *Chem. – A*

Eur. J., vol. 13, no. 18, pp. 5106–5112, Jun. 2007, doi: https://doi.org/10.1002/chem.200601003.

[61] Y. Ma *et al.*, "In-situ prepared MIL-53(Fe)/BiOI photocatalyst for efficient degradation of tetracycline under visible-light driven photo-Fenton system: Investigation of performance and mechanism," *J. Alloys Compd.*, vol. 870, p. 159524, 2021, doi: https://doi.org/10.1016/j.jallcom.2021.159524.

[62] M. Dan-Hardi *et al.*, "A New Photoactive Crystalline Highly Porous Titanium(IV) Dicarboxylate," *J. Am. Chem. Soc.*, vol. 131, no. 31, pp. 10857–10859, Aug. 2009, doi: 10.1021/ja903726m.

[63] Y. Fu *et al.*, "An amine-functionalized titanium metal-organic framework photocatalyst with visible-light-induced activity for CO_2 reduction," *Angew. Chem. Int. Ed. Engl.*, vol. 51, no. 14, pp. 3364–3367, 2012, doi: 10.1002/anie.201108357.

[64] S. Yin *et al.*, "Construction of NH_2-MIL-125(Ti)/Bi_2WO_6 composites with accelerated charge separation for degradation of organic contaminants under visible light irradiation," *Green Energy Environ.*, vol. 5, no. 2, pp. 203–213, 2020, doi: https://doi.org/10.1016/j.gee.2020.03.008.

[65] H. Fu, L. Wu, J. Hang, P. Wang, C. Zhao, and C.-C. Wang, "Room-temperature preparation of MIL-68 and its derivative In2S3 for enhanced photocatalytic Cr(VI) reduction and organic pollutant degradation under visible light," *J. Alloys Compd.*, vol. 837, p. 155567, 2020, doi: https://doi.org/10.1016/j.jallcom.2020.155567.

[66] K. G. M. Laurier, F. Vermoortele, R. Ameloot, D. E. De Vos, J. Hofkens, and M. B. J. Roeffaers, "Iron(III)-Based Metal–Organic Frameworks As Visible Light Photocatalysts," *J. Am. Chem. Soc.*, vol. 135, no. 39, pp. 14488–14491, Oct. 2013,

doi: 10.1021/ja405086e.

[67] D. Yan, H. Hu, N. Gao, J. Ye, and H. Ou, “Fabrication of carbon nanotube functionalized MIL-101(Fe) for enhanced visible-light photocatalysis of ciprofloxacin in aqueous solution,” *Appl. Surf. Sci.*, vol. 498, p. 143836, 2019, doi: https://doi.org/10.1016/j.apsusc.2019.143836.

[68] Y. Li *et al.*, “TiO_2 Nanoparticles Anchored onto the Metal–Organic Framework NH_2-MIL-88B(Fe) as an Adsorptive Photocatalyst with Enhanced Fenton-like Degradation of Organic Pollutants under Visible Light Irradiation,” *ACS Sustain. Chem. Eng.*, vol. 6, no. 12, pp. 16186–16197, Dec. 2018, doi: 10.1021/acssuschemeng.8b02968.

[69] S.-W. Lv, Y. Cong, X. Chen, W. Wang, and L. Che, “Developing fine-tuned metal–organic frameworks for photocatalytic treatment of wastewater: A review,” *Chem. Eng. J.*, vol. 433, p. 133605, 2022, doi: https://doi.org/10.1016/j.cej.2021.133605.

[70] D. Han *et al.*, “Enhanced photocatalytic activity and photothermal effects of cu-doped metal-organic frameworks for rapid treatment of bacteria-infected wounds,” *Appl. Catal. B Environ.*, vol. 261, p. 118248, 2020, doi: https://doi.org/10.1016/j.apcatb.2019.118248.

[71] S. Li *et al.*, “Electron Redistributed S-Doped Nickel Iron Phosphides Derived from One-Step Phosphatization of MOFs for Significantly Boosting Electrochemical Water Splitting,” *Adv. Funct. Mater.*, vol. 32, no. 23, p. 2200733, Jun. 2022, doi: https://doi.org/10.1002/adfm.202200733.

[72] X. Wang *et al.*, “Photocatalytic Cr(VI) elimination over BUC-21/N-$K_2Ti_4O_9$ composites: Big differences in performance resulting from small differences in

composition," *Chinese J. Catal.*, vol. 42, no. 2, pp. 259–270, 2021, doi: https://doi.org/10.1016/S1872-2067(20)63629-4.

[73] P. Hu, C. Yao, L. Yang, Y. Xin, and Y. Miao, "Boosted photodegradation of tetracycline hydrochloride over Z-scheme MIL-88B(Fe)/Bi_2WO_6 composites under visible light," *Colloids Surfaces A Physicochem. Eng. Asp.*, vol. 627, p. 127248, 2021, doi: https://doi.org/10.1016/j.colsurfa.2021.127248.

[74] X. Wei, C.-C. Wang, Y. Li, P. Wang, and Q. Wei, "The Z-scheme NH_2-UiO-66/PTCDA composite for enhanced photocatalytic Cr(VI) reduction under low-power LED visible light," *Chemosphere*, vol. 280, p. 130734, 2021, doi: https://doi.org/10.1016/j.chemosphere.2021.130734.

[75] Y. Wang *et al.*, "Defect engineering of NH_2-MIL-88B(Fe) using different monodentate ligands for enhancement of photo-Fenton catalytic performance of acetamiprid degradation," *Chem. Eng. J.*, vol. 398, p. 125684, 2020, doi: https://doi.org/10.1016/j.cej.2020.125684.

[76] L. Duan, H. Jiang, B. Cai, W. Wu, D. Lin, and K. Yang, "Regulating defect density of iron based metal–organic frameworks by defective ligands functionalization to enhance fenton-like activity and stability," *Chem. Eng. J.*, vol. 479, p. 147768, 2024, doi: https://doi.org/10.1016/j.cej.2023.147768.

[77] G. Cheng *et al.*, "Visible light enhanced persulfate activation for degradation of tetracycline via boosting adsorption of persulfate by ligand-deficient MIL-101(Fe) icosahedron," *Chemosphere*, vol. 317, p. 137857, 2023, doi: https://doi.org/10.1016/j.chemosphere.2023.137857.

[78] H. Chen *et al.*, "Construction of ultra-high defective iron-based metal organic frameworks with small molecule acid regulator for enhanced degradation of

sulfamethoxazole," *J. Clean. Prod.*, vol. 348, p. 131367, 2022, doi: https://doi.org/10.1016/j.jclepro.2022.131367.

[79] S. Hu *et al.*, "Solvothermal synthesis of NH_2-MIL-125(Ti) from circular plate to octahedron," *CrystEngComm*, vol. 16, no. 41, pp. 9645–9650, 2014, doi: 10.1039/C4CE01545B.

[80] N. Liu *et al.*, "Ultrathin graphene oxide encapsulated in uniform MIL-88A(Fe) for enhanced visible light-driven photodegradation of RhB," *Appl. Catal. B-ENVIRONMENTAL*, vol. 221, pp. 119–128, 2018, doi: 10.1016/j.apcatb.2017.09.020.

[81] L. A. González-Burciaga, C. M. Núñez-Núñez, M. M. Morones-Esquivel, M. Avila-Santos, A. Lemus-Santana, and J. B. Proal-Nájera, "Characterization and Comparative Performance of TiO_2 Photocatalysts on 6-Mercaptopurine Degradation by Solar Heterogeneous Photocatalysis," 2020. doi: 10.3390/catal10010118.

[82] J. W. Yoon, D. H. Kim, J.-H. Kim, H. W. Jang, and J.-H. Lee, "NH_2-MIL-125(Ti)/TiO_2 nanorod heterojunction photoanodes for efficient photoelectrochemical water splitting," *Appl. Catal. B Environ.*, vol. 244, pp. 511–518, 2019, doi: https://doi.org/10.1016/j.apcatb.2018.11.057.

[83] A. Fidalgo, S. Letichevsky, and B. F. Santos, "Assessment of TiO_2 band gap from structural parameters using artificial neural networks," *J. Photochem. Photobiol. A Chem.*, vol. 405, p. 112870, 2021, doi: https://doi.org/10.1016/j.jphotochem.2020.112870.

[84] N. J. Castellanos, Z. Martinez Rojas, H. A. Camargo, S. Biswas, and G. Granados-Oliveros, "Congo red decomposition by photocatalytic formation of hydroxyl

radicals (·OH) using titanium metal–organic frameworks," *Transit. Met. Chem.*, vol. 44, no. 1, pp. 77–87, 2019, doi: 10.1007/s11243-018-0271-z.

[85] M. Alfè, V. Gargiulo, M. Amati, V.-A. Maraloiu, P. Maddalena, and S. Lettieri, "Mesoporous TiO_2 from Metal-Organic Frameworks for Photoluminescence-Based Optical Sensing of Oxygen," 2021. doi: 10.3390/catal11070795.

[86] G. Jia *et al.*, "Wet-chemistry hydrogen doped TiO_2 with switchable defects control for photocatalytic hydrogen evolution," *Matter*, vol. 5, no. 1, pp. 206–218, Jan. 2022, doi: 10.1016/j.matt.2021.10.027.

[87] X. Liao *et al.*, "Synthesis of (100) surface oriented MIL-88A-Fe with rod-like structure and its enhanced fenton-like performance for phenol removal," *Appl. Catal. B-ENVIRONMENTAL*, vol. 259, 2019, doi: 10.1016/j.apcatb.2019.118064.

[88] C. Serre, C. Mellot-Draznieks, S. Surblé, N. Audebrand, Y. Filinchuk, and G. Férey, "Role of solvent-host interactions that lead to very large swelling of hybrid frameworks," *Science*, vol. 315, no. 5820, pp. 1828–1831, 2007, doi: 10.1126/science.1137975.

[89] X. Kang *et al.*, "Integration of mesopores and crystal defects in metal-organic frameworks via templated electrosynthesis," *Nat. Commun.*, vol. 10, 2019, doi: 10.1038/s41467-019-12268-5.

[90] Y. Lu *et al.*, "Enhanced Active Sites and Stability in Nano-MOFs for Electrochemical Energy Storage through Dual Regulation by Tannic Acid," *Angew. CHEMIE-INTERNATIONAL Ed.*, vol. 62, no. 41, 2023, doi: 10.1002/anie.202311075.

[91] L. Luo *et al.*, "Directional Engraving within Single Crystalline Metal-Organic Framework Particles via Oxidative Linker Cleaving," *J. Am. Chem. Soc.*, vol. 141,

no. 51, pp. 20365–20370, 2019, doi: 10.1021/jacs.9b10499.

[92] C.-Z. Wang *et al.*, "Pore Size Modulation in Flexible Metal-Organic Framework Enabling High Performance Gas Sensing," *Angew. CHEMIE-INTERNATIONAL Ed.*, vol. 62, no. 26, 2023, doi: 10.1002/anie.202302996.

[93] M. Liu, L. Zu, and Z. M. Hudson, "Mechanistic Principles for Engineering Hierarchical Porous Metal-Organic Frameworks," *ACS Nano*, 2022, doi: 10.1021/acsnano.2c06587.

[94] Y. Sun *et al.*, "Synergistic Effect of Oxygen Vacancy and High Porosity of Nano MIL-125(Ti) for Enhanced Photocatalytic Nitrogen Fixation," *Angew. CHEMIE-INTERNATIONAL Ed.*, vol. 63, no. 3, 2024, doi: 10.1002/anie.202316973.

[95] H. Wang *et al.*, "A Universal Single-Atom Coating Strategy Based on Tannic Acid Chemistry for Multifunctional Heterogeneous Catalysis," *Angew. CHEMIE-INTERNATIONAL Ed.*, vol. 61, no. 14, 2022, doi: 10.1002/anie.202200465.

[96] C. Liu *et al.*, "Amorphous Metal-Organic Framework-Dominated Nanocomposites with Both Compositional and Structural Heterogeneity for Oxygen Evolution," *Angew. CHEMIE-INTERNATIONAL Ed.*, vol. 59, no. 9, pp. 3630–3637, 2020, doi: 10.1002/anie.201914587.

[97] Z. Fang, Y. Liu, J. Qi, Z.-F. Xu, T. Qi, and L. Wang, "Establishing a high-speed electron transfer channel *via* CuS/MIL-Fe heterojunction catalyst for photo-Fenton degradation of acetaminophen," *Appl. Catal. B-ENVIRONMENTAL*, vol. 320, 2023, doi: 10.1016/j.apcatb.2022.121979.

[98] X. Wang *et al.*, "Regulated Dual Defects of Bridging Organic and Terminal Inorganic Ligands in Iron-based Metal-Organic Framework Nodes for Efficient Photocatalytic Ammonia Synthesis," *Angew. CHEMIE-INTERNATIONAL Ed.*,

vol. 63, no. 22, 2024, doi: 10.1002/anie.202404258.

[99] F. Guo *et al.*, "Designing Heteroatom-Codoped Iron Metal-Organic Framework for Promotional Photoreduction of Carbon Dioxide to Ethylene," *Angew. CHEMIE-INTERNATIONAL Ed.*, vol. 62, no. 14, 2023, doi: 10.1002/anie.202216232.

[100] S. Dissegna, K. Epp, W. R. Heinz, G. Kieslich, and R. A. Fischer, "Defective Metal-Organic Frameworks," *Adv. Mater.*, vol. 30, no. 37, 2018, doi: 10.1002/adma.201704501.

[101] X.-H. Li *et al.*, "Constructing Mimic-Enzyme Catalyst: Polyoxometalates Regulating Carrier Dynamics of Metal-Organic Frameworks to Promote Photocatalytic Nitrogen Fixation," *ACS Catal.*, vol. 13, no. 11, pp. 7189–7198, 2023, doi: 10.1021/acscatal.3c00944.

[102] Y. Jiang *et al.*, "In situ turning defects of exfoliated Ti_3C_2 MXene into Fenton-like catalytic active sites," *Proc. Natl. Acad. Sci. U. S. A.*, vol. 120, no. 1, 2022, doi: 10.1073/pnas.2210211120.

[103] Y. Shi, X. Wang, X. Liu, C. Ling, W. Shen, and L. Zhang, "Visible light promoted Fe_3S_4 Fenton oxidation of atrazine," *Appl. Catal. B-ENVIRONMENTAL*, vol. 277, 2020, doi: 10.1016/j.apcatb.2020.119229.

[104] Z. Yang, A. Yu, C. Shan, G. Gao, and B. Pan, "Enhanced Fe(III)-mediated Fenton oxidation of atrazine in the presence of functionalized multi-walled carbon nanotubes," *WATER Res.*, vol. 137, pp. 37–46, 2018, doi: 10.1016/j.watres.2018.03.006.